8-2015

Improving Attenuation Correction in Hybrid Positron Emission Tomography

Hua Asher Ai

IMPROVING ATTENUATION CORRECTION IN

HYBRID POSITRON EMISSION TOMOGRAPHY

A

DISSERTATION

Presented to the Faculty of

The University of Texas

Health Science Center at Houston

and

The University of Texas

M. D. Anderson Cancer Center

Graduate School of Biomedical Sciences

In Partial Fulfillment

Of the Requirements

For the Degree of

DOCTOR OF PHILOSOPHY

by

Hua Asher Ai, B.Sc.

Houston, TX

August, 2015

A journey of one thousand miles begins with a single step.

- Laozi

Table of Contents

This work is dedicated to my mother, my father and my grandma, for their unwavering and unrelenting support to me all through my life; also to everyone else I love in this world, for inspiring me to become a better human being each and every day.

Acknowledgements

I take this opportunity to express my gratitude for all the help and support I have received from the wonderful mentors and colleagues at the University of Texas MD Anderson Cancer Center.

First and foremost, my deepest gratitude goes to my advisor and the chair of my supervisory committee, Dr. Richard Wendt III, without whom the completion of this dissertation would not have been possible. I have benefitted much from his vast knowledge in medical physics and perpetual kindness towards the younger generation since the early stage of my graduate school journey. His patience, wisdom and constant encouragement have helped me get through the most challenging times.

I am immensely grateful to Dr. Tinsu Pan, who led me into the fascinating field of hybrid PET imaging. It is his pioneering work in PET/CT that inspired this research, and his insightful advice was instrumental to its progression. I appreciate the tremendous amount of effort he spent in helping me grow as a scientist and a professional. His hardworking attitude and uncompromising pursuit of scientific rigor are the things I will always look up to.

I would also like to extend my special thanks to the members of my supervisory committee: Dr. Jim Bankson and Dr. Jason Stafford, for the valuable advice they have provided me with their enormous knowledge and expertise in MR; Dr. Yiping Shao, for his incisive comments on research and academia, his constructive criticism and his refreshing perspectives as a PET expert; and Dr. Michele Guindani, for guiding me through the statistical concepts and his help with my writing. In addition to their dedication and commitment to my dissertation, I also owe a debt of gratitude for the compassion and support they had shown me in my time of need.

There are many other people to whom I feel grateful. Dr. Jingfei Ma opened the door to the realm of MR for me, and provided crucial guidance during my initial struggle with all those sophisticated concepts. Dr. Osama Mawlawi provided much help to me in

IMPROVING ATTENUATION CORRECTION IN HYBRID POSITRON EMISSION TOMOGRAPHY

Hua Asher Ai, B.Sc.

Advisory Professor: Richard Wendt III, Ph.D.

Hybrid positron emission tomography imaging techniques such as PET/CT and PET/MR have undergone significant developments over the last two decades and have played increasingly more important roles both in research and in the clinic. A unique advantage PET has over other clinical imaging modalities is its capability of accurate quantification. However, as the most critical component of PET quantification, attenuation correction in hybrid PET systems is challenged in several different aspects, including the spatial-temporal mismatch between the PET emission images and the associated attenuation images provided by the complementary modality, and the difficulty in bone identification in the MR-based attenuation correction approaches. These problems, if left unaddressed, can limit the potential of the hybrid PET systems.

This research developed solutions to overcome the spatial-temporal mismatch in PET/CT and PET/MR, and established the requirements for bone identification in PET/MR. An automatic registration algorithm based on a modified fuzzy c-means clustering method and gradient correlation was developed and validated to perform automatic registration in cardiac PET/CT data of different breathing protocols. A free-breathing MR protocol and post-process algorithm were developed to provide MR-based attenuation images that also match the temporal resolution of PET and were evaluated in a feasibility study. The relationship between the sensitivity of bone identification in attenuation images and PET quantification of bone lesions uptake was evaluated in a simulated study using data from ^{18}F-sodium fluoride PET/CT exams.

List of Figures

List of Tables

List of Abbreviations

AC - attenuation correction

ACT - respiration-average CT

BVF - bone volume fraction

CT - computed tomography

FCM - fuzzy c-means

FMMV - fraction of mis-projected myocardium volume

FWHM - full width half maximum

HCT - helical CT (also known as spiral CT)

HU - Hounsfield unit

MRI - magnetic resonance imaging

PET - positron emission tomography

RF - radiofrequency

ROI - region of interest

RSS - root-of-sum-of-square

SNR - signal-to-noise ratio

SPGR - spoiled gradient recalled echo

TE - echo time

TISA - total in-slice attenuation, defined as the summation of all voxel values within a CT slice

TR - repetition time

UTE - ultrashort echo time

Chapter 1: Introduction and Background

1.1 Introduction

This work aims to improve the accuracy of hybrid positron emission tomography by reducing the spatial-temporal mismatch between emission and attenuation images and by defining the requirements for the correction of bone attenuation in PET/MR scanners.

Positron emission tomography (PET) is a functional imaging technique that can provide *in vivo*, metabolic information of various molecular, biological processes of the subject in a non-invasive manner. It obtains functional information of a specific metabolic activity (for example, myocardial blood flow, receptor density, cellular mitosis and glucose metabolism) by first injecting the positron-emitting radioactive tracer that exclusively targets such metabolic process into the subject, and then detecting the pair of 511 keV gamma photons created from positron-electron annihilation events and thereby tracking the distribution of injected tracer. Because the concentration of the tracer reflects the local level of activity of the target metabolic process, the distribution and accumulation of the tracer, captured by the reconstructed PET images, can reveal information about the underlying metabolism.

Since its clinical introduction in the early 1990s by Siemens and GE [1], PET has gained widespread popularity in clinical practices, including neurology [2], cardiology [3], pharmacology [4] and, probably most importantly, oncology [5-7]. As more applications have been developed, the imaging modality itself has also evolved over the last few decades, with two of the greatest milestones being the introductions of the two

hybrid PET imaging modalities: combined PET/CT systems and combined PET/MR systems.

Previous studies have consistently demonstrated that PET provides better diagnostic performance than Single Photon Emission Computed Tomography (SPECT), which is another widely used functional imaging modality in nuclear medicine. Among the many advantages PET has, one of the most important is its potential for absolute quantification via accurate correction of the loss of photon counts to the media that photons have to travel through before reaching the PET detectors. This is largely attributable to the unique mechanism utilized by PET imaging: instead of detecting individual photons, PET detects pairs of photons that reach the gantry simultaneously, and localizes their origin to lie along the line connecting the two points of detection. As a result, the number of photon pairs lost to the medium depends only on the total amount of attenuation along the path connecting the detector pairs and not upon the precise location where the annihilation event occurs [8]. Accurate correction of the photon attenuation during the PET scan is thus possible, at least in theory.

Attenuation correction of the PET data requires an accurate knowledge of the distribution of attenuation coefficients of the various media that attenuate the photons. In the design that is used in the early generation of stand-alone PET systems, this is achieved with separate transmission scans performed independently of the emission scan. A positron-emitting source to produce 511 keV photons, usually ^{68}Ge in the physical form of a rod, is rotated around the empty bore of the scanner, and the number of

coincidence events is recorded to produce the so-called blank scan. This process is usually done once a day and its data are used for all of the PET scans performed during the day. The same process is repeated when each subject of the PET exam is placed inside the scanner. From the difference of the recorded numbers of coincidence events with and without the patient, a map of photon attenuation coefficients is calculated and used to perform attenuation correction.

However, the maximal count rate that can be recorded by PET detectors is restricted by the hardware, which limits the number of coincidence events that can be detected by the PET scanner per unit time. At the same time, a certain number of photon counts is required in order to obtain an acceptable signal-to-noise ratio (SNR) in the attenuation coefficient map and thus adequate quality in the attenuation-corrected image. As a result, a relatively long acquisition time is usually required for the transmission scan, which alone can be as long as 40 minutes. This greatly limits the clinical throughput of PET scans made with such devices, and despite the long scan duration, attenuation maps calculated from transmission scans often remain noisy.

1.2　Background and Significance

1.2.1　Hybrid PET/CT Imaging

The invention of the combined PET/CT system in 1998 and its subsequent introduction to the clinic in 2001 is a revolutionary development of the PET technology. The integration

of a computed tomography module into the PET system provides several important advantages.

First, it produces complementary, anatomical images that are well-registered with the functional images provided by PET. This enables accurate localization of functional abnormality including tumor infiltration of adjacent structures which could not be assessed conclusively using separate CT and PET data [9]. The combination of PET and CT has been shown to consistently result in improved diagnostic performance over either modality when used alone [10-12].

Secondly, attenuation coefficient maps of 511 keV photons can be derived from CT images, which represent the attenuation coefficients at lower energy levels of 80-140 kVp [13, 14]. This capability essentially eliminated the necessity for PET transmission scans. In these methods, the photon attenuation coefficients between the lower energy levels of 80-140 kVp CT X-rays and the higher energy 511 keV PET photons are measured for homogenous tissue types, mainly soft tissue and cortical bone. The scaling factors between different energy levels, which differ for different materials and tissue types, are determined and then used to convert CT images into PET attenuation maps. Voxels with CT coefficients that fall between the measured values of the homogeneous tissue types are simply assumed to be a mixture of the materials that have been characterized. Any voxel below 0 HU is assumed to be a mixture of air and soft tissue, while any voxel above 0 HU is assumed to be a mixture of soft tissue and bone. Under this assumption, the conversion of the CT measured attenuation coefficients into 511 keV

attenuation coefficients can be achieved with a bilinear scaling procedure. This attenuation correction strategy has been verified and proven to be sufficiently accurate when compared to the PET transmission scan approach, and thus has become the de facto gold standard for PET attenuation correction.

Since a whole-body CT scan acquired in helical CT mode takes less than 20 seconds, the replacement of PET transmission scans with a CT scan for attenuation correction purposes shortens the duration of a PET imaging session from about one hour to 30 minutes or less. The briefer exam duration improves patient comfort and also increases the clinical throughput of the imaging procedure. CT-derived attenuation maps have vastly better noise properties compared to the ones from PET transmission scans, although the better signal-to-noise ratio and higher spatial resolution do come at the price of increased radiation dose to the patient. It has been reported that the effective dose contributed by CT can account for 50%-80% of the total effective dose of a whole-body PET/CT exam [15].

Because of the advantages provided by the integration of CT, combined PET/CT imaging technology was rapidly embraced by the healthcare professions. By 2006, all major vendors had stopped offering standalone whole-body PET systems, and hybrid PET/CT became the standard form of PET imaging. By the middle of 2008, over 3000 combined PET/CT systems had been installed worldwide and were being employed in routine clinical operations.

1.2.2　Respiration-Induced Attenuation Artifact

Although CT-based attenuation correction offers a number of benefits, it also creates some problems. In addition to the higher radiation dose, another problem is the attenuation artifact that arises when there is spatial mismatch between the PET emission images and the CT attenuation images despite the mechanical registration of the combined scanner modules.

Attenuation artifacts can arise when the values in the map of attenuation coefficients that are used for correction purposes do not match the actual attenuation that affects the emitted photons during the PET exam. This is most problematic when the misregistration between emission and attenuation images involves a region containing different photon-attenuating media with large difference in attenuation properties, such as the interfaces between lungs and soft tissues, between air and soft tissues, and between soft tissues and bones.

Attenuation artifacts are a common problem in PET imaging of the thorax due to the presence of respiratory motion. In PET/CT imaging, the PET scan and the CT scan are performed sequentially, not simultaneously. On the one hand, the PET emission scan is generally slow and can take 2-5 minutes for each bed acquisition to complete, and so clinical PET scans are always done while the patient breathes freely. As a result, the reconstructed PET emission images reflect the spatial distribution of PET tracers averaged over multiple respiratory cycles. On the other hand, CT attenuation scans are usually performed during a breath-hold. This is done to avoid the inconsistent

measurements that can be induced by respiration and lead to artifacts in the reconstructed helical CT images. This means that the breathing states captured by the two modalities are different, which can cause severe spatial misregistration between the emission and the attenuation images that gives rise to attenuation artifacts.

1.2.3 Four-dimensional Computed Tomography (4DCT) and Respiration-Averaged CT (ACT)

The use of a slowly rotating gantry in the CT scan has been suggested as a method to produce a motion blurring or averaging effect that is similar to that seen in the PET images [16]. However, CT data acquired with a slowly rotating gantry can cause inconsistency in the measured data as the patient anatomy moves from view to view during respiration. This produces new artifacts in the CT scan.

Four-dimensional CT was developed as a solution to address the problem of respiratory motion in the thorax [17]. In 4DCT scans, the CT gantry rotates around the target with a fast rotation speed in axial mode while the patient table remains stationary. The table is then moved and the process repeated if a longer axial field of view is required. The acquisition at each table position lasts longer than one respiratory cycle. The CT data are sorted into respiratory phases; volumetric CT data corresponding to the patient's anatomy at various respiratory phases can be then obtained and accumulated into a time-resolved CT or 4DCT dataset. The phase-sorted CT data can also be averaged over the respiratory cycle to mimic the signal averaging intrinsic in the PET images.

4DCT can effectively reduce the motion artifact in the CT images that is caused by respiratory motion as well as provide information about the motion itself. However, since the SNR of the 3DCT data at each phase of the respiratory cycle needs to be maintained, the acquisition of 4DCT delivers a greater radiation dose to the patient.

Respiration-averaged CT (ACT) can be directly created from cine axial CT data even without recording the respiratory signal [18]. In this approach, a low-dose, cine CT protocol continuously acquires CT images for the duration of a respiratory cycle at each table location while the patient breathes freely. All images acquired at the same location are averaged to create the respiration-averaged CT images. Several studies have shown that ACT is effective in reducing the spatial mismatch between PET and CT data [19, 20].

1.2.4 Hybrid PET/MR Imaging

While combined PET/CT systems were under development, there was also interest in combined PET/MR systems. A hybrid PET/MR system is desirable because it offers several distinct advantages over PET/CT, including superior soft tissue contrast, reduced radiation dose to the patient, the potential for simultaneous, multi-parametric functional imaging, and real-time motion tracking and correction [21]. However, combining PET and MR scanners poses a much more formidable engineering challenge than combining PET and CT. This is primarily because of the employment of photomultiplier tubes (PMT) in the traditional PET detector module: the PMT is extremely adversely affected

by the strong magnetic field that is required for MR imaging. In the first ever combined PET/MR prototype, which was developed by Shao *et al.* in 1997 [22], 4-meter long optical fibers were used to transmit the light from the scintillation crystals (placed inside the MR bore) to the PMTs located outside the main magnetic field.

The subsequent development of PET/MR systems mainly involved using MR-compatible PET detectors such as avalanche photodiodes (APD). A prototype PET/MR system featured a PET head insert based on lutetium oxyorthosilicate (LSO)-APD detector rings in a 3T MR system. It was introduced into clinical research in 2006 and used for the first human PET/MR study, which was of the brain [23]. The first whole-body PET/MR system (Philips Ingenuity TF PET/MR Hybrid Imaging System, Best, The Netherlands) became commercially available in 2010. It used two separate MR and PET scanners that were placed in the same room and shared a common table to shuttle the patient between the scanners [24]. This design can minimize any potential interference between the PET and MR hardware. However, MR and PET exams have to be performed sequentially. A variation of this design, triple-modality PET/CT-MRI, was also reported [25]. Also in 2010, the first fully integrated whole-body PET/MR system [26] with the potential of simultaneous PET/MR imaging (Siemens Biograph mMR, Erlangen, Germany) was introduced. By 2014, about 50 whole-body PET/MR systems were operational worldwide [27]. The adoption of PET/MR systems has been relatively slow in contrast to the adoption of PET/CT, for which about 500 systems had been operational worldwide three years after its introduction [27]. This is possibly due to higher cost, more complicated operations, lack of reimbursement and some uncertainty in the targeted key

clinical applications. Although at a slower pace, interest in hybrid PET/MR systems continues to grow steadily.

1.2.5 PET Attenuation Correction with MR images

Despite the progress in the development of hybrid PET/MR systems, many technical challenges remain for PET/MR imaging, among which attenuation correction is critical. Ideally, for PET/MR systems the map of attenuation coefficients should be derived from the MR images, since a CT-based attenuation map is not available, and the addition of PET transmission scans to PET/MR imaging is less than desirable because the limited diameter of MR scanner bores leaves little space, if any, for the rotation of a transmission source. Unfortunately, attenuation correction based on MR images is not a simple task.

First, a number of scanner structures that attenuate the 511 keV photons, such as the patient table, the positioning aids and the MR RF coils, are not visible in typical MR images. It is possible to compute 3D templates of the attenuation coefficients of fixed structures that are invisible in MR and insert them digitally back into an MR-derived attenuation map [28, 29]. However, such methods are difficult to implement correctly when the structure's size or location is not predictable, as in the case of non-rigid MR surface coils. Secondly, direct conversion from MR images to a PET attenuation map is not possible because MR signals represent the proton density weighted by the tissue relaxation properties: the spin-lattice relaxation time T_1 and the spin-spin relaxation time T_2. They are not correlated with the photon attenuation coefficients. Other challenges

include the truncation artifact when the patient is larger than the limited MR field of view (FOV) [30], and the artifacts to which MR is susceptible when the patient contains metal implants [31].

In order to create PET attenuation maps from MR images, a number of approaches have been proposed. They fall into two broad categories: atlas-based approaches and tissue-classification-based approaches.

Atlas-based methods derive attenuation maps from MR images with the aid of a pre-established atlas, which contains either CT images only [32] or co-registered pairs of MR and CT images [33, 34]. Patient-specific MR images are converted to pseudo-CT images with either deformable registration or machine learning-based methods. Pseudo-CT images derived from these approaches have continuously-distributed attenuation values and are visually similar to real CT images, most notably including bone. Unfortunately, this approach is prone to artifacts when the patient has anatomical abnormalities that are not well represented by the data in the atlas.

Tissue-classification-based approaches, also known as segmentation-based approaches, assign each voxel to one of several different types or "classes" of tissue using the MR images, which are usually acquired with T_1-weighted gradient echo sequences. Standard, discrete attenuation values are then assigned to the classified voxels to create MR-based attenuation maps. Differences among patients in the attenuation values of the same tissue class are usually ignored. This approach is relatively straightforward and can, in theory, adapt to any atypical anatomy. So far, all

commercially available systems have adopted the tissue-classification approach for attenuation correction in PET/MR systems. The Philips Ingenuity TF system uses a three-class segmentation method [35], which classifies the voxels of the MR images as air, lung or soft tissues, while the Siemens Biograph mMR uses a four-class segmentation method [36], which classifies the voxels as air, lung, fat or non-fat tissues. Fat and non-fat tissues are distinguished using Dixon water-fat imaging sequences.

In current MR-based attenuation correction methods, bone is not identified as a separate tissue class. Instead, the bones are assimilated into soft tissue with the aid of morphological operations and assigned with the soft tissue attenuation coefficient. However, this can be problematic. In the human body, bone is much more attenuating to photons than are the soft tissues. For 511 keV photons, the attenuation coefficients of bone and soft tissues are approximately 0.172 cm^{-1} [14] and 0.100 cm^{-1} [37], respectively. Given such a marked difference, bone should ideally be identified as a separate tissue class in a tissue-classification-based MR AC approach. Unfortunately, bone imaging using MR is a longstanding challenge, and identification of bone in MR images is very difficult. The MR signal represents tissue proton density weighted by its relaxation times. The proton density of bone is only 20-25% of that of typical soft tissues. More importantly, the transverse relaxation time, T_2 (and its counterpart in gradient echo sequences, T_2^*), of bone (0.3-0.5 ms) is substantially shorter than those of typical soft tissues (10-300 ms). Because of the extremely short T_2, the MR signal of bone decays almost instantaneously after each RF excitation. Thus, bones are essentially invisible in

13

typical clinical MR images. Voxels containing only bone have values that are indistinguishable from those of air.

Ultrashort-echo-time (ultrashort-TE or UTE) sequences have been proposed for the segmentation of bone for PET/MR attenuation correction [37, 38]. Using specially designed RF pulses, UTE sequences are capable of realizing an extremely short echo time (TE), which can capture the MR signal of bone before it has decayed completely. Quantitative MR parameters, such as R_2^* ($=1/T_2^*$) or proton density [39], can then be used to separate bone from the air and soft tissues.

Although UTE sequences have shown some promise in making bone visible in MR, another impediment to effective MR bone imaging has rarely been discussed: the averaging of bone and soft tissues within a voxel as a result of the limited spatial resolution and voxel size used in typical clinical MR imaging. Some parts of the human skeleton can be very thin and often are smaller than the size of the voxels that are used in clinical MR imaging protocols. As a result, in a typical 3D MR dataset, a considerable number of voxels contain both bone and soft tissue. Identifying bone in voxels with a lower fraction of bone is more difficult than in voxels with a higher fraction of bone, and as of now it is unclear how the heterogeneity of voxel contents in regarding to bone and soft tissue influence the quantification of PET. The consequences of intra-voxel heterogeneity are investigated as part of this work.

1.2.6 Statement of Problem and Scope of Dissertation

Quantitative, functional imaging has been increasingly incorporated into routine clinical care and is expected to play an even greater role in the future as modern healthcare heads in the direction of personalized and precision medicine. As one of the primary functional imaging modalities, the integration of PET with CT has been proven to be tremendously successful, and the integration of PET with MR, another powerful modality that can be used for both morphological and functional imaging, also has exhibited great potential. However, it is important to ensure that the capability of achieving accurate quantification in PET is not compromised in the hybrid modalities.

Despite the development and progress in hybrid PET systems, there are a number of problems that can compromise attenuation correction and quantification of the PET data that remain to be solved. The goal of this dissertation is to address some of the problems that can adversely affect the quantification of PET and to improve attenuation correction of PET in the hybrid systems. More specifically, this work addressed three currently existing problems that plague the attenuation correction of hybrid PET systems.

1. The spatial misregistration that can occur between PET and CT images of the heart.

An automatic registration algorithm was developed for cardiac PET/CT in order to achieve accurate registration and reduction of the attenuation artifacts caused by the misregistration between PET and CT images.

2. The temporal mismatch that exists between PET and MR images of the heart.

A fast 2D MR protocol and an associated post-processing algorithm were developed to produce MR-based attenuation maps that have a temporal resolution that is consistent with PET.

3. The difficulty of identifying bone in MR and the resultant PET quantification bias in bone lesions.

The scenarios in which bones are identified in MR images with various levels of sensitivities and then assigned with proper attenuation coefficients were simulated with CT images, and the impact of bone identification sensitivity on PET quantification of bone lesions was studied.

1.3   Summary of the Chapters

1.3.1   Chapter 2: Reduction of Spatial Misregistration between PET and CT

The hypothesis of this study is that an automatic registration algorithm based on FCM-assisted gradient correlation for cardiac PET/CT data can reduce misregistration between PET and CT to less than 5mm (which is the physical spatial resolution for typical clinical PET scanners) on average compared to manual registration regardless of the CT breathing protocol.

In order to reduce the spatial misregistration between cardiac PET and CT images, an automatic registration algorithm was developed for both helical CT and average CT images based on the principle of gradient correlation with the assistance of a

modified fuzzy c-means clustering algorithm. The algorithm was developed on a training group containing 55 cardiac PET/CT datasets and tested on a testing group containing another 65 different datasets. The results of automatic registration were evaluated against manual registration. A quantitative measure that characterizes the fraction of myocardial volume mis-projected into lung tissues was developed as a secondary measure to evaluate the registration results.

1.3.2   Chapter 3: Reduction of Temporal Mismatch between PET and MR

The hypothesis of this study is that using respiration-averaged MR images for PET attenuation correction is feasible, and can reduce the PET attenuation artifact compared to using MR images obtained under breath-hold.

A method that aims to reduce the temporal mismatch between PET emission data and MR-derived attenuation data was developed based on the same principle that is utilized in average CT for PET/CT. A 2D fast SPGR sequence was used to obtain cine MR images over one respiratory cycle while the patient breathed freely. A three-class tissue-classification approach was adapted to convert the individual cine MR images into pseudo-CT images. Two different sets of attenuation coefficients were assigned to create the segmented attenuation images. These were then averaged over the different phases to obtain pseudo-ACT images, which were subsequently used for the attenuation correction of the PET data. The difference between the AMR-corrected and the ACT-corrected PET

data was evaluated quantitatively as well as with a clinically relevant, semi-quantitative measure.

1.3.3 Chapter 4: Effect of Bone Identification Sensitivity on PET Quantification Accuracy

The hypothesis of this study is that using a binary-tissue-classification-based MR attenuation correction approach with a bone identification sensitivity of 50% bone volume fraction can reduce the PET bone lesion quantification errors caused by the presence of bone to be less than 5%.

Data from eight NaF PET/CT studies were analyzed. Sodium fluoride is used to image the skeleton. Homogeneous bone voxels were first identified on the CT attenuation images with combined thresholding and morphological operations and then used to reduce the inaccuracy in the measured CT attenuation coefficients. A metric called the Bone Volume Fraction (BVF) was estimated for each voxel in the CT attenuation images. Attenuation images were constructed for different thresholds of the bone volume fraction. Attenuation correction was performed with the simulated attenuation maps. The effect of bone identification sensitivity on quantification was evaluated in 139 NaF-avid bone sites using the PET data corrected with the original CT as a reference.

1.3.4 Chapter 5: Conclusions

The main goals of this dissertation were achieved. The automatic registration algorithm was found to be effective in reducing spatial misregistration between the PET and CT images regardless of the breathing protocol. It was also found to be as effective as manual registration in reducing the mis-projection of myocardial activity. The MR protocol was able to obtain artifact-free respiration-averaged MR images of the thorax while the patient was breathing freely, and the feasibility of converting respiration-averaged MR images to PET attenuation maps were demonstrated. The non-monotonic relationship between PET bone lesion quantification accuracy and bone identification sensitivity was revealed, and the requirements on reducing quantification errors in bone lesions uptakes were established.

Chapter 2:   Reduction of Spatial Mismatch between PET and CT

2.1 Abstract

In cardiac perfusion PET/CT studies, respiratory motion can cause a mismatch between the PET and CT data, which can cause erroneous projection of myocardial uptake into lung tissues and therefore lead to attenuation artifacts in the reconstructed PET images. Fast helical CT (HCT) acquired at or near the end-expiration phase of the respiratory cycle under breath-hold, and cine respiration-averaged CT (ACT) acquired over a respiratory cycle under free-breathing have been proposed to reduce the mismatch between CT and PET images and to mitigate inaccurate quantitation in PET images caused by the mismatch. However, neither ACT nor HCT can eliminate the mismatch from voluntary patient motion such as self-repositioning for a more comfortable position during the exam, for which image registration is required. The purpose of this study was to develop and evaluate an automatic registration algorithm to minimize the spatial mismatch between CT and PET data and to improve the quantification of cardiac perfusion data. We used 3D rigid-body translation for registration of the CT to PET data in this study. A modified fuzzy c-means clustering algorithm was introduced to facilitate and regulate the algorithm. A similarity metric was constructed as the vector correlation of the gradient maps derived from the PET and CT images. The algorithm was developed on a training group containing 55 consecutive clinical datasets and tested on a separate group of 65 datasets. The registration results were compared to the results from two observers and evaluated with an objective metric that characterizes the fraction of mis-projected myocardial volume (FMMV) inside lung tissues. Misalignment between the PET and CT data was observed in both the medial-lateral and superior-inferior directions

for HCT but only in the medial-lateral direction in ACT. The frequency and extent of large misalignment (>=10mm) was less severe in ACT than in HCT. The automatic registration algorithm reduced the overall misalignment between the PET and CT data from 6.8±2.7mm to 3.9±1.7mm for ACT and from 9.5±8.6mm to 3.7±1.6mm for HCT. The misalignment after automatic registration was no greater than the inter-observer variability. Evaluation of the objective metric showed that myocardial uptake is projected into lung tissues in the PET/CT data before registration ($FMMV_{ACT}$ = 11.3±9.0%, $FMMV_{HCT}$ = 20.1±22.7%), and the mis-projection is substantially reduced after registration by the observers ($FMMV_{ACT}$ = 1.5±1.5%, $FMMV_{HCT}$ = 2.4±2.5%) and by the algorithm ($FMMV_{ACT}$ = 1.4±1.5%, $FMMV_{HCT}$ = 2.5±2.4%). Auto-registration reduced the attenuation artifacts in cases with severe misalignment. This algorithm is effective for cardiac PET/CT registration for both the fast helical CT at or near end-expiration and the averaged CT regardless of the CT breathing protocol, and is potentially useful in a clinical setting. ACT is better than HCT in reducing the mismatch between CT and PET data in cardiac PET/CT, but it still requires registration to achieve accurate quantification.

2.2   Introduction

Positron emission tomography (PET) has the capability to quantify myocardial perfusion *in vivo*. The diagnostic accuracy of PET has been shown to surpass that of the more routinely used single photon emission computed tomography (SPECT) [40]. Previous research has suggested that PET, as a noninvasive method, can provide a definitive

assessment of early or advanced coronary atherosclerosis [41]. The accuracy of quantification of PET imaging in PET/CT can be affected by various factors, the most important of which is the attenuation correction of PET data with CT images, which depends largely on the registration of the CT and PET data [42-46].

Because the acquisition duration of CT is generally much shorter than that of PET (less than three seconds for a 16-slice helical CT (HCT) compared to several minutes for PET), anatomic mismatch can occur between PET and CT images due to respiratory motion [47]. This problem is especially prominent in cardiac PET imaging because the heart is directly above the diaphragm and is thus subjected to respiratory motion. Such mismatch can cause the myocardial uptake to be erroneously projected into lung tissues and, if left uncorrected, can lead to severe artifacts in the reconstructed PET images (Figure 1) that can be misinterpreted as myocardial ischemia or infarction. Special breathing maneuvers, such as asking patients to hold their breath at or near end-expiration for a fast HCT scan to obtain better matches between CT and PET data, can reduce the mismatch to some extent [48-50], but these maneuvers may be too difficult for sicker patients to perform.
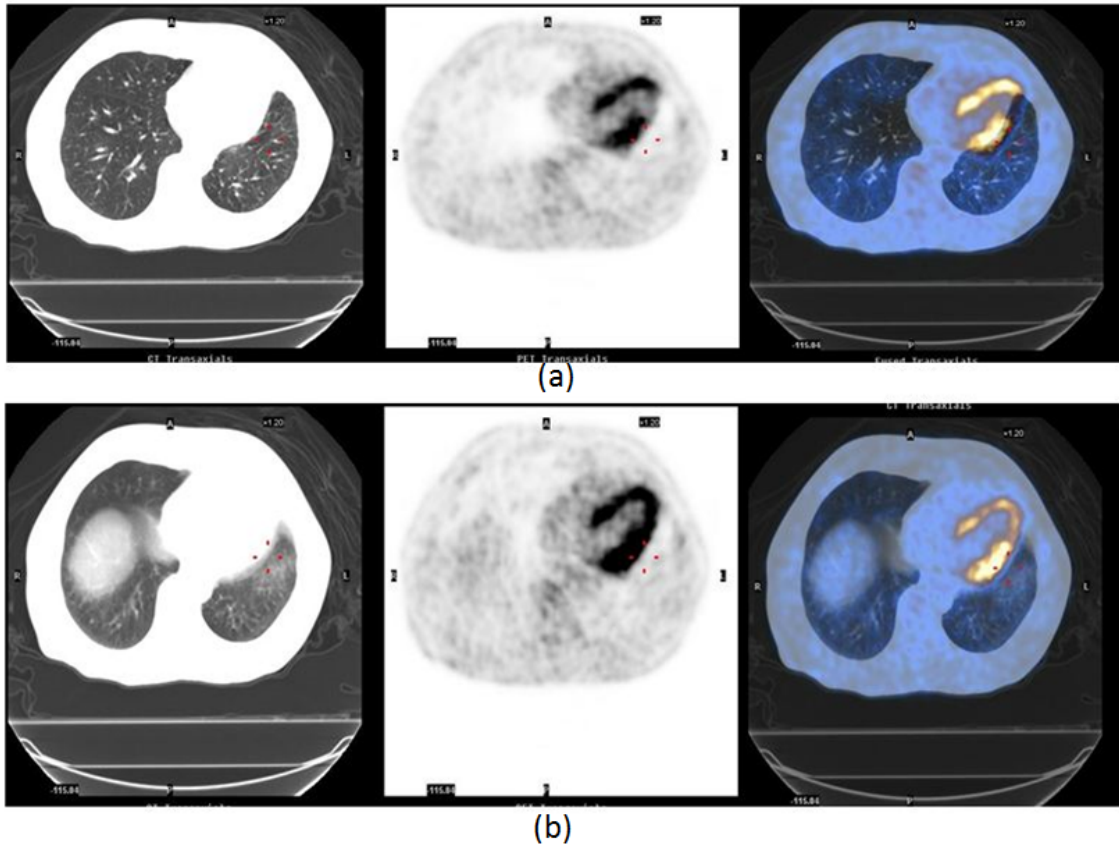
Figure 1. An example of the misregistration between PET and CT. The images from left to right are CT, PET, and fused CT and PET. An attenuation artifact is shown in (a) with HCT. ACT in (b) was able to fix the artifact.

We have also investigated cine respiration averaged CT (ACT) to scan patients under free-breathing in order to match the temporal resolution of CT and PET images and reduce misregistration. In ACT, the CT slices acquired under the cine mode over various phases of the respiratory cycle are averaged to match the PET data taken over several minutes spanning many respiratory cycles [18, 51, 52]. The efficacy of ACT has also been verified independently by other groups [19, 20]. However, ACT alone cannot compensate for gross physical motion of the patient; a mismatch between CT and PET

data can still occur, for which image registration is necessary. The mismatch under ACT is easier to manage than under HCT because it is mostly caused by patient re-positioning for a more comfortable position during the scan instead of mismatch in the breathing state between the CT and PET data. For the latter, a more sophisticated deformation type of registration may be needed [53]. In the clinic, image registration is generally performed manually with a 3D rigid-body translation, which is subjective and thus susceptible to operator variability. Rigid-body translation may not be effective if the mismatch is due to respiratory motion, which is non-rigid in nature and can be more effectively taken care of by ACT. The purpose of this research was to develop an automatic registration algorithm to reduce misregistration between CT and PET data in cardiac PET/CT for both ACT and HCT.

Various registration algorithms – most of them based on 3D rigid-body translation – have been proposed previously to automatically register cardiac PET images with CT attenuation images. Khurshid *et al.* [54] developed a 2D edge-based method which registers PET and CT data by minimizing the distance between the edges detected in PET and in CT. However, the results of their algorithm were not validated against manual registration, leaving the accuracy of the algorithm in question. Also, edge detection is likely to have a greater uncertainty on ACT datasets due to edge blurring from averaging data over the respiratory cycle. Alessio *et al.* [53] developed a registration scheme based on the Radon consistency conditions between attenuation and emission data. Their method includes rotations in the modeling to improve algorithm robustness against PET data corrupted with artifacts. It is also computationally intensive.

Mutual information methods are popular for multi-modality image registration and have also been investigated for cardiac PET/CT with some success [55-57]. However, Martinez-Moller *et al.* [44] found the mutual information method to be incapable of properly assessing the similarity of the cardiac PET and CT data. They circumvented registration and developed an emission-driven method to reduce attenuation artifacts by assigning soft tissue attenuation coefficients to all voxels that are located inside the lung region in the attenuation image and correspond to the myocardium in the emission image. Their method was effective in artifact reduction but requires alteration of the attenuation images, instead of registration, which can have unknown effects on PET quantification.

The challenge in registering cardiac PET images with CT images lies in the fact that PET images represent the distribution of the injected tracer, which is different from the CT images, which represent the anatomy of the body. For the cardiac region, in PET images the myocardium appears hyperintense while in CT the myocardium and the blood have a similar intensity (unless a contrast agent is present in the blood of the patient). Consistent with the findings of Martinez-Moller *et al.* [44], our experiments demonstrated that the dissimilarity between PET and CT images usually limits the robustness of the methods that derive a similarity index such as mutual information from the original images.

We noted that in manual registration of the CT and PET data, human observers often pay the most attention to the high-gradient regions at the myocardial boundaries, regardless of the breathing protocol types of the CT images. In light of this observation,

we developed a novel registration algorithm for cardiac PET/CT to improve registration (hence mitigating the attenuation artifact) using a 3D gradient correlation with a modified fuzzy c-means (FCM) clustering algorithm. To the best of our knowledge, this is the first cardiac PET registration algorithm that has been developed for and evaluated on both clinical ACT and HCT images. The results of automatic registration were compared against those from manual registration and evaluated with an objective metric that characterizes the fraction of mis-projected myocardial volume (FMMV) inside the lung region.

2.3   Materials and Methods

2.3.1   Patient Data

We used Matlab (The Mathworks, Natick, MA) for the development of the algorithm. A group of 55 sets of consecutive cardiac perfusion Rb-82 PET/CT images was used in the development of the algorithm (training group), and a separate group of 65 datasets was used to test the effectiveness of the algorithm (testing group). The data were retrospectively obtained, and the patient information was de-identified. Each patient data set consists of 1) a breath-hold HCT scan at or near end-expiration before the resting perfusion PET data and 2) ACT derived from a free-breathing, low-dose cine CT scan covering the heart after the stress perfusion PET data. The stress PET images without attenuation correction (PET_{noAC}) were used for registration with the ACT and HCT. The PET data were acquired over five minutes and reconstructed with the filtered back

projection (FBP) algorithm with a Butterworth filter using a cutoff frequency of 0.55, and roll-off of 10. Randoms were corrected by the option of singles, and scatter correction was applied. Both CT and PET images were reconstructed for a 50.0-cm field of view over a longitudinal coverage of 15.4 cm with 3.27 mm slice spacing. The matrix size was $512 \times 512 \times 47$ for CT and $128 \times 128 \times 47$ for PET. Because the gradient calculation is sensitive to noise, both ACT and HCT images were filtered with a 2D, 5mm-FWHM Gaussian filter. The smoothing filter also enhances the gradient map in HCT which facilitates the registration algorithm.

2.3.2 Matching image spatial resolution

A summary of the algorithm is presented in Figure 2. Before processing the images, we performed linear interpolation of the datasets so that the image matrix size matched in all three orthogonal directions. Selection of the target spatial resolution depends on the desired precision of image registration. For faster computation, we adopted a dual-resolution approach: the two sets of images were first matched on the lower resolution of the PET image (3.91 mm $\times$ 3.91 mm) to generate a fast and approximate registration result. Then the images were matched on the higher resolution of the CT image (0.98 mm $\times$ 0.98 mm) to improve the precision.
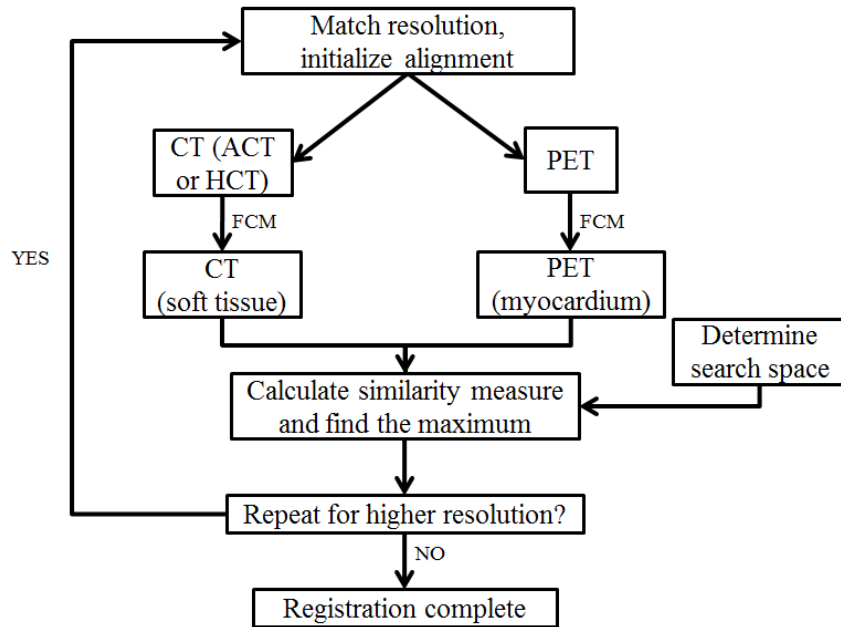
Figure 2. Flow chart illustrating our automatic registration algorithm. After initialization (matching resolution and initializing alignment), both CT and PET images go through fuzzy c-means (FCM) clustering to extract relevant information. The similarity index over a pre-determined search volume is then calculated based on gradient correlation to find the maximum. We adopted a dual-resolution approach, which represents the pixel sizes of PET and CT. The algorithm is first executed at the low-resolution level with a larger search volume; the PET and CT datasets are realigned according to the results. The algorithm is then executed at the high-resolution level to improve the registration precision. This substantially reduces the execution time of the algorithm compared to a single high-resolution approach with the same search volume.

2.3.3   Application of the Modified Fuzzy C-means Clustering Algorithm

We employed a modified FCM algorithm [58] to facilitate the registration of cardiac PET/CT data. Unlike in conventional segmentation techniques in which each pixel

belongs to only a particular cluster, in FCM clustering each pixel can have a partial membership (expressed as numerical values ranging continuously from 0 to 1) in each cluster. The memberships of a particular pixel in all clusters add up to 1. We selected FCM instead of other segmentation techniques because FCM-segmented images (i.e., the maps of memberships) vary smoothly at the edges and therefore preserve the gradient information that is crucial to our method. For CT, the soft tissue cluster is extracted for registration; for PET, the myocardial cluster is extracted.

The introduction of FCM into the algorithm serves two purposes: 1) to extract the information that is most relevant to the registration and 2) to introduce a regulation parameter that can be used to optimize the algorithm. Our implementation of FCM is summarized in the following paragraphs.

In the original FCM clustering algorithm [59], the memberships of each pixel in each cluster are found by solving an optimization problem for the objective function (J):

$$J = \sum_{i=1}^{N} \sum_{j=1}^{c} u_{ji}^{m} \cdot | x_i - v_j |^2$$

Eq. 2-1

where N is the total number of image pixels; c is the pre-selected total number of clusters; i and j are the indices for the pixel and cluster, respectively; u_{ji} is the membership of pixel i in cluster j; m is the parameter that controls the "fuzziness" of the computation, which is set to 2 (FCM algorithms generally use 2 for this value); x_i is the intensity of pixel i; and v_j is the centroid value of cluster j. This problem can be solved by iteratively computing the following equations (in which k is the index of the clusters):

$$v_j = \frac{\sum\limits_{i=1}^{N} x_i u_{ji}^m}{\sum\limits_{i=1}^{N} u_{ji}^m} \qquad \text{Eq. 2-2}$$

$$u_{ji} = \frac{1}{\sum\limits_{k=1}^{c} |\frac{x_i - v_j}{x_i - v_k}|^{2/(m-1)}} \qquad \text{Eq. 2-3}$$

Both the memberships and cluster centroids are updated in each iteration. The iteration ends when the difference between two consecutive iterations in u and/or v is lower than a predetermined threshold.

Instead of iterative computation in the original FCM algorithm, we assign pre-determined values to the cluster centroids and calculate the associated membership values in our implementation. Not only does this step reduce computation, it also improves the robustness of the algorithm because automatic estimation of the FCM centroids can fail in certain CT and PET cases in which an atypical distribution of pixel values is encountered. For example, for a patient with little body fat, in FCM of the CT image the fat can be absorbed into the soft tissue cluster, and another cluster, usually either lung or bone, will be split into two clusters. Assigning pre-determined centroid values can be justified for the CT images because the CT numbers for different tissue types, especially those for soft tissue, do not vary substantially among patients. Five clusters – representing air, lung, fat, non-fat soft tissue, and bone – are used in the processing of CT images. The cluster centroids assigned in our study are the mean values of the cluster centroids, which are automatically estimated from the CT images in the 55 datasets of the

training group: air = -980 HU, lung = -680 HU, fat = -120 HU, soft tissue = 30 HU, bone = 480 HU.

For the processing of PET images, the assigned centroid values are dependent on the maximal activity inside the myocardium, I_{max}, which can be identified automatically. For the background (air), non-myocardial tissue and myocardium, the centroids were assigned as 0, 0.2 I_{max}, and α I_{max}, respectively. The cluster centroid for non-myocardial tissue was determined empirically by observing the histogram of the PET images in the training group, which was found to be typically in the range of 10% to 30% of the maximum myocardial uptake. The parameter α was introduced as a means to regulate the segmentation of the myocardium in PET, which in turn regulates the PET gradient map calculation and thus the registration algorithm. To determine the appropriate value for α, we performed the computation with various α values on the training group and compared the results to those from manual registration. Once the cluster centroids have been set, the memberships can be computed according to Eq. 2-3.

After FCM segmentation, clusters that represent the myocardium in the PET images (PET_{myoc}) and the soft tissues in the CT images (CT_{soft}) are extracted (Figure 3) and used for calculating the similarity index.
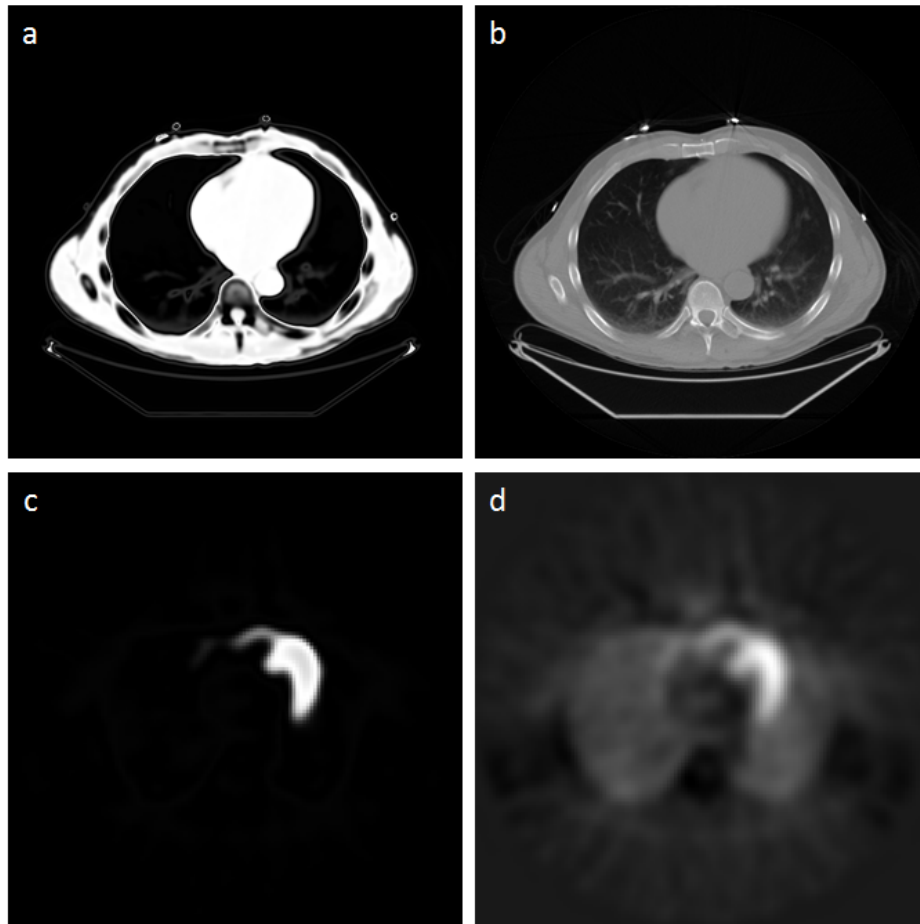
Figure 3. The CTsoft (a) and PETmyoc images (c) compared with the original CT (b) and PET (d) images. Voxels with high membership in the soft tissue cluster in CT and the myocardial cluster in PET appear hyperintense in each image.

2.3.4 Similarity Index

For our algorithm, registration is modeled as a 3D rigid-body translation, which is also what has been used in manual registration. In this model, the alignment of the PET and CT data can be uniquely described by a vector $\vec{\Delta l}$ of three coordinates, representing the

relative displacements between the PET and CT datasets along the three orthogonal axes; the corresponding similarity index $S(\Delta \vec{l})$ is defined as the vector correlation between the two gradient maps:

$$S(\Delta \vec{l}) = \sum_{\vec{r} \in V} \nabla I_{PET_{myoc}}(\vec{r}) \cdot \nabla I_{CT_{soft}}(\vec{r}, \Delta \vec{l}) \qquad \text{Eq. 2-4}$$

where $\vec{r}$ is the spatial location of pixels in the frame of reference of the PET coordinate system (which in our algorithm is kept stationary); V is an automatically determined volume of interest (VOI) that encloses the cardiac anatomy in PET; ∇ is the 3D gradient operator; and $I_{PET_{myoc}}$ and $I_{CT_{soft}}$ are the intensities of PET$_{myoc}$ and CT$_{soft}$, respectively. To determine the VOI, a minimal 3D bounding box was automatically selected to enclose all the myocardial voxels above 50% of the maximal myocardial uptake. The bounding box was then extended by 5% of the FOV along the longitudinal direction (8 mm) and the two axial directions (25 mm) on both ends so that the VOI had a sufficient coverage. The gradient operator produces a 3D vector, each element of which is calculated by averaging the results of the forward and backward finite difference operations. The gradient along the S-I direction is scaled to account for the difference between the resolutions within the plane and perpendicular to the plane.

2.3.5 Search for the Optimal Registration

Like many other commonly used similarity indices in image registration, the gradient correlation can have local maxima (Figure 4). Non-exhaustive search schemes such as the gradient descent algorithm are not guaranteed to arrive at the desired global maximum.

However, owing to the simplicity of this similarity index, an exhaustive search scheme is computationally affordable. Adoption of an exhaustive search scheme also ensures the reproducibility of the algorithm. In our dual-resolution approach, the vector representing the initial alignment of PET and CT is defined as $\Delta \vec{l} = 0$. In the low-resolution registration, the corresponding similarity index $S(\Delta \vec{l})$ was computed for every possible translation $\Delta \vec{l}$ within a 3D search volume of 51 mm $\times$ 51 mm $\times$ 101 mm centered at the initial alignment. The search volume was determined according to the maximal initial misalignment in the training datasets. The registration with the maximal similarity is chosen as the initial alignment for the high-resolution registration. It should be noted that in the low-resolution stage, the gradient map along the anterior-posterior (A-P) direction was excluded from the calculation of the similarity index in order to improve the robustness of the algorithm. The reason is that the A-P gradient in CT images along the anterior cardiac wall sometimes has a very narrow spatial distribution; as a result, during the low-resolution registration stage it can be overpowered by the gradient at the anterior chest wall and cause erratic registration results.

The same process is repeated at the higher resolution with a smaller search volume of 17 mm $\times$ 17 mm $\times$ 3 mm. The search volume has a greater expansion in the in-plane directions to compensate for the exclusion of the A-P gradient at the low-resolution stage. A representative distribution of the similarity index is shown in Figure 4.
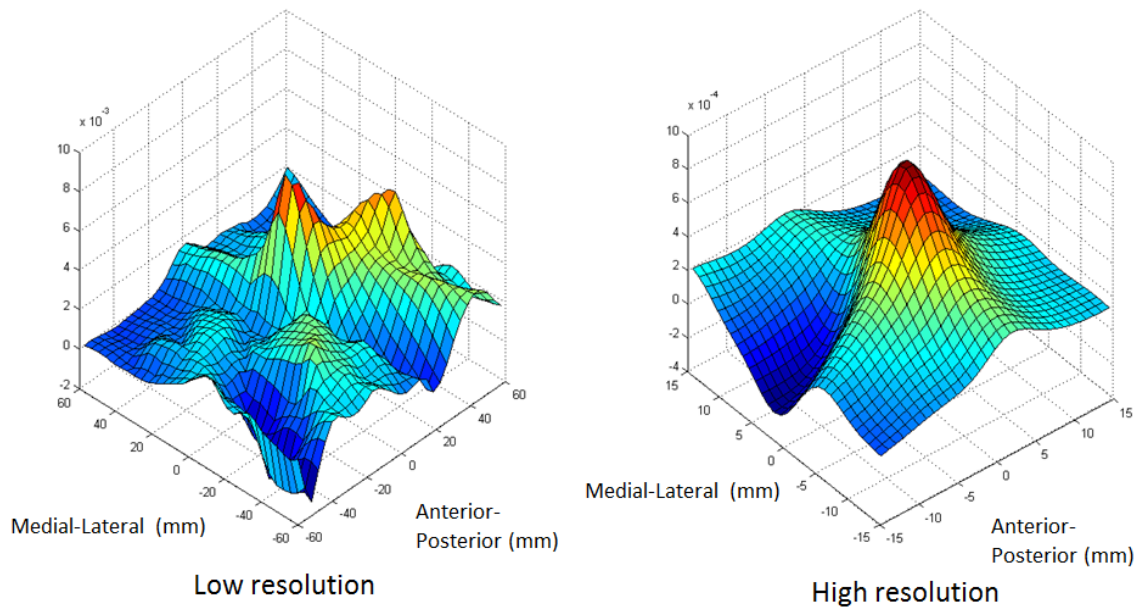
Figure 4. Typical similarity distribution at low resolution (3.91 mm × 3.91 mm with a large search volume) and high resolution (0.98 mm × 0.98 mm with a small search volume). For better visualization, the 3D volumetric data were collapsed onto two dimensions in both plots by taking the maximum value along the superior-inferior direction.

2.3.6 Parameter optimization and evaluation of registration results

The algorithm was first applied to the training group with the value of α, the regulating parameter in the FCM processing of the cardiac PET data, varying between 0.30 and 0.95. The optimal value for α was then determined and the algorithm was applied to the testing group. Manual registration was performed on both groups by two observers using our in-house manual registration software that allows visualization of the fused PET/CT images as well as their interactive alignment using 3D rigid-body translation. In order to

36

improve the accuracy and consistency of the procedure, the manual registration was conducted in the following manner:

1) the two observers were asked to perform manual registration independently on the PET/CT datasets while blinded to the results of the algorithm and of each other's manual registration; 2) the registration results from the two observers were compared, and for cases with large disagreements (>=5 mm), the two observers were asked to repeat the registration until the disagreement was less than 5 mm; 3) the average registration position was then used as the reference to which the automatic registration results were compared.

In addition to assessing the difference between the automatic and manual registrations, we designed an objective metric with which to evaluate the registration results. Because attenuation artifacts in cardiac PET originate from the erroneous projection of myocardial uptake into lung tissues, the fraction of mis-projected myocardial volume (FMMV) inside the lung tissue of the CT images can serve as an indicator of the severity of the attenuation artifact in the reconstructed PET images. FMMV is computed as:

$$FMMV = \frac{V_{myoc} \bigcap V_{lung}}{V_{myoc}} \qquad \text{Eq. 2-5}$$

For a pair of registered PET/CT data, values of FMMV that are close to 0 denote minimal mis-projection of the myocardial uptake, and hence minimal attenuation artifact is expected. On the other hand, if FMMV is considerably greater than 0, a more severe attenuation artifact can be expected in the reconstructed PET image (Figure 5). In our

approach, we measured FMMV by first segmenting the myocardium from PET_{noAC} and the lungs from CT and then calculating the percentage of the myocardial voxels in the PET data that fell inside the lungs in the CT images. Both segmentations were performed with a threshold-based region-growing algorithm instead of FCM in order to avoid any potential bias. The segmentation of the myocardium was performed with a lower threshold of $0.5I_{max}$ and was manually validated for each case. The segmentation of the lung was performed with the threshold of -330 HU, which is the average of the mean lung HU and the mean soft tissue HU from one of our previous studies [60]. The results of the lung segmentation were also manually verified.

FMMV=0.3%   FMMV=4.3%   FMMV=12.6%
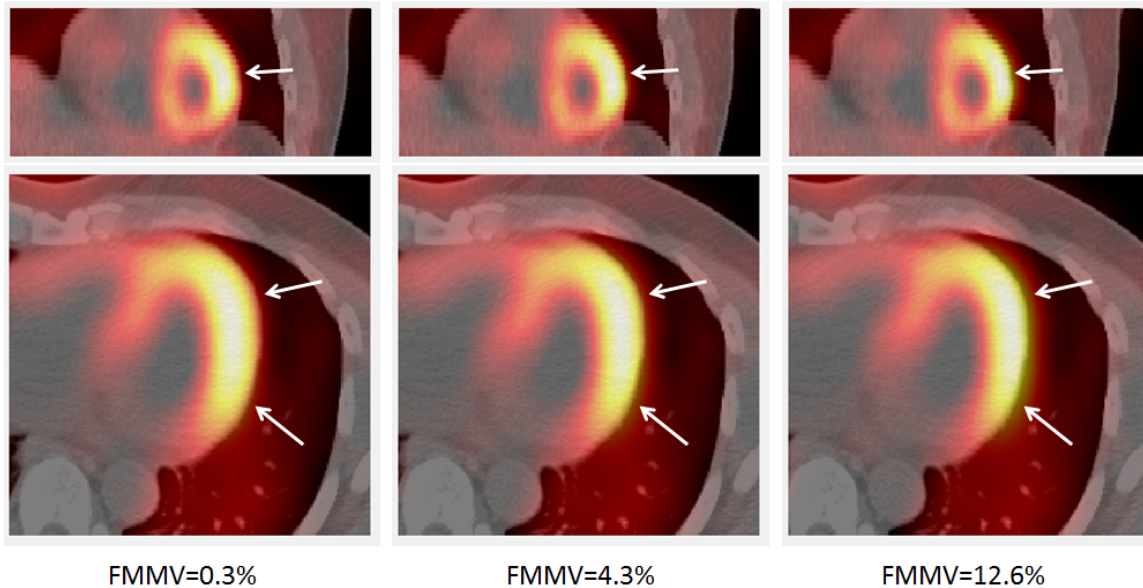
Figure 5. Examples of calculated FMMV at different registrations. The mis-projection in these examples is highlighted by white arrows. A higher FMMV value indicates more cardiac uptake being erroneously projected into the lung tissues, which generally leads to attenuation artifacts.

FMMV quantifies the amount of the myocardium in the PET images that encroaches into the lung region of the CT images; therefore it can be a good indicator of attenuation artifact. It should be noted that FMMV by itself cannot directly quantify the accuracy of registration because a large misalignment between PET and CT <u>could</u> still have a low or nil FMMV value when the myocardium in PET is "pulled" deep into the heart region on CT. FMMV can, however, evaluate the relative quality of two registrations if the possibility of the aforementioned scenario has been precluded, e.g. when the PET and CT data have been registered using either manual or automatic registration.

The two-sided Wilcoxon signed rank test was the primary statistical test employed to evaluate the significance of the difference because the numerical results in this study did not follow a normal distribution. In the case of different sample sizes, a two-sided Wilcoxon rank sum test was used. The two-sided Z-test was also used when testing results involving proportions. For the cases with a prominent initial misregistration, the PET images were attenuation-corrected with the CT images before and after the automatic registration to demonstrate the reduction of attenuation artifacts.

2.4   Results

2.4.1   Manual registration

Inter-observer variability of the manual registration was evaluated in data from both the training group and the testing group (i.e., $N_{total}=55+65=120$) since it does not depend on

the algorithm. For the first round of manual registration, the disagreements between the two observers were 4.6±2.0 mm (max 11.1 mm) and 4.2±2.0 mm (max 9.0 mm) for ACT and HCT datasets (p = 0.094), respectively, with 43/120, or 36%, and 36/120, or 30%, cases (p = 0.336) having inter-observer disagreement greater than 5 mm. After repeated registration of these cases where the disagreement exceeded 5 mm, the disagreements reduced to 3.0±1.3 mm and 2.8±1.4 mm for ACT and HCT, respectively.

2.4.2 FCM parameter selection

Using the average manual registration provided by the two observers as the reference, the effect of the PET FCM parameter α on the registration error is plotted in Figure 6 for both the HCT and the ACT data from the training group. When α is too small (<=0.60), the FCM segmentation of the myocardium in PET starts to fail, which in turn leads to erratic registration results. A "stable" region is observed for values above 0.60; however, increasing α imposes a small yet consistent error in the alignment compared to the manual registration and thus should be also avoided. Weighing both the registration errors and the risk of algorithmic failure, α = 0.65 was selected for the registration with both ACT and HCT for the testing group.
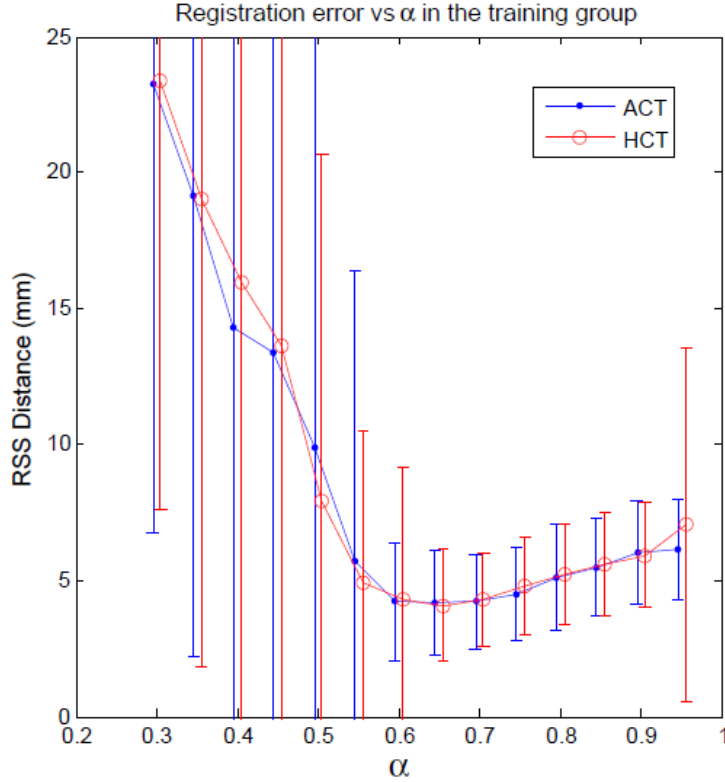
Figure 6. Registration difference between algorithm and manual registration as α varies in the training datasets. A low α can cause the registration algorithm to fail due to inappropriate FCM segmentation of PET images. A "stable" region is observed for α ≥ 0.65.

2.4.3 Misalignments in ACT and HCT before and after Automatic Registration

Execution of our dual-resolution Matlab-based algorithm takes approximately 15 seconds on a Dell Precision T5600 workstation (Intel Xeon E5-2667, 2.9 GHz). The misalignments between PET and CT in the testing group before and after automatic registration (using the average manual registration as the reference) are listed in Table 1 and plotted in Figure 7. The initial misalignment of ACT is less than that of HCT

(6.8±2.7 mm vs 9.5±8.6 mm), although the difference was not found to be statistically significant using the Wilcoxon signed rank test (p = 0.165). For cases with greater initial misalignments (either ACT <u>or</u> HCT >=10 mm), however, the mismatch in ACT datasets is significantly smaller than that in HCT (8.4±3.3 mm vs 16.4±10.8 mm, N = 24, p = 0.005, not tabulated). In addition, for cases with large misalignments (>=10 mm) both the frequency (9/65 vs 20/65, p = 0.021) and extent (11.9±2.0 mm vs 18.8±10.2 mm, p = 0.030) are less severe in ACT than in HCT. The findings agree with those of previous investigations [19, 20, 47].
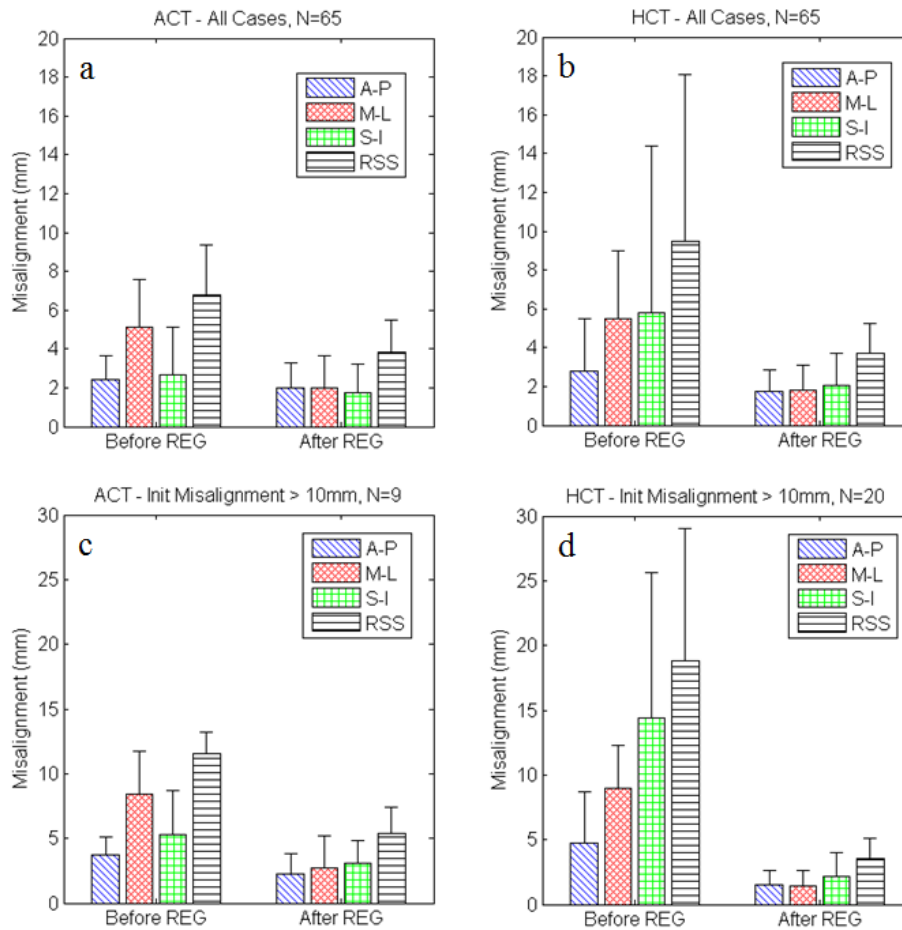
Figure 7. Misalignment between PET and ACT/HCT data before and after automatic registration (REG) using manual registration results as reference for all cases (a, b) and cases with initial misalignment greater than 10mm (c, d) in the testing group. Initial misalignment is prominent only in M-L for ACT, while both M-L and S-I shows a relatively large misalignment for HCT. After automatic registration, registration is improved in all directions for both ACT and HCT. The improvement in registration is more evident in cases with greater initial misalignments.

The initial misalignment in the M-L direction is relatively prominent for both ACT (5.2±2.6 mm) and HCT (5.5±3.5 mm). This is the direction along which patient

motion is most likely to occur. On the other hand, the initial misalignment along the A-P direction is minor for both ACT (2.4±1.2 mm) and HCT (2.8±2.7 mm) datasets. This is most likely due to motion restriction by the scanner table. Along the S-I direction, however, HCT has a substantially greater misalignment than ACT (5.8±8.6 mm vs 2.7±2.4 mm, p = 0.012). This is most readily attributable to the end-expiration breath-hold of the HCT protocol, which moves the heart away from its average location along the S-I direction, and the longer temporal separation between the HCT scan and the PET stress scan.

This algorithm significantly reduced the overall misalignment (root-of-sum-of-squares, or RSS, distance) and misalignments along each orthogonal direction for both HCT and ACT datasets (Table 1). After registration, the RSS misalignment decreased to 3.9±1.7 mm for ACT and 3.7±1.6 mm for HCT, respectively. The residue RSS misalignment in ACT was found to be less than that of the inter-observer variability (p = 0.017), and in HCT they were found to be comparable (p = 0.135). The reduction of misalignment was particularly conspicuous in datasets with greater initial misalignments (Table 1, Figure 7). Examples of registration are shown in Figure 8.

Table 1. Misalignment between PET and CT before and after registration. Numbers in parentheses are the maximal distances within that group.

All cases (N=65)

Distance from reference (mm)		ACT	HCT	p-value
Anterior-Posterior (A-P)	**Before**	2.4±1.2 (5.9)	2.8±2.7 (13.7)	0.927
	After	2.0±1.3 (4.9)	1.7±1.1 (4.9)	0.186
	p-value	0.035	0.031	
Medial-Lateral (M-L)	**Before**	5.2±2.6 (14.6)	5.5±3.5 (15.1)	0.511
	After	2.0±1.7 (6.8)	1.8±1.3 (4.9)	0.395
	p-value	<0.001	<0.001	
Superior-Inferior (S-I)	**Before**	2.7±2.4 (9.8)	5.8±8.6 (42.5)	0.012
	After	1.8±1.5 (6.5)	2.0±1.7 (6.5)	0.303
	p-value	0.005	<0.001	
Root-of-Sum-of-Square (RSS)	**Before**	6.8±2.7 (15.5)	9.5±8.6 (45.4)	0.165
	After	3.9±1.7 (9.0)	3.7±1.6 (8.6)	0.636
	p-value	<0.001	<0.001	

Cases with initial misalignment >=10mm in ACT (N=9)

Distance from reference (mm)	ACT			
	A-P	**M-L**	**S-I**	**RSS**
Before	3.7±1.3 (5.9)	8.8±3.7 (14.6)	5.5±3.3 (9.8)	11.9±2.0 (15.5)
After	2.2±1.6 (4.9)	3.0±2.4 (6.8)	3.3±1.6 (6.5)	5.5±2.1 (9.0)
p-value	0.094	0.004	0.188	0.004

Cases with initial misalignment >=10mm in HCT (N=20)

Distance from reference (mm)	HCT			
	A-P	**M-L**	**S-I**	**RSS**
Before	4.8±3.9 (13.7)	8.9±3.3 (15.1)	14.4 ±11.2 (42.5)	18.8±10.2 (45.4)
After	1.5±1.1 (4.9)	1.5±1.1 (4.9)	2.1±1.9 (6.5)	3.5±1.6 (6.6)
p-value	0.005	<0.001	<0.001	<0.001
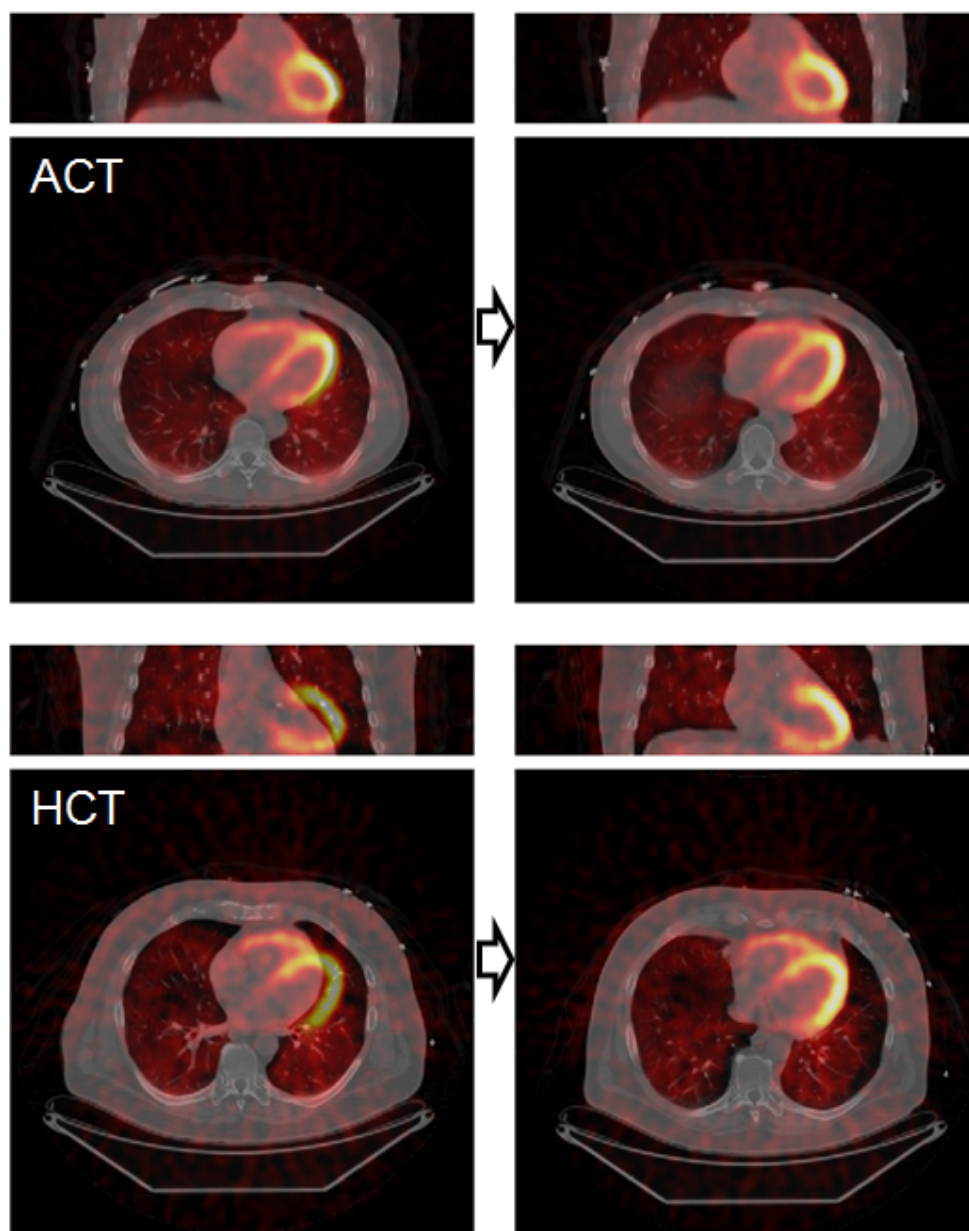
Figure 8. Examples of misalignment before and after registration by the algorithm. Both ACT and HCT cases were initially mis-aligned and become well-aligned after the automatic registration. Misalignment in HCT can be particularly severe due to respiration mismatch and is generally minor in ACT, though registration is still necessary for accurate quantification.

2.4.4 Reduction of Erroneously Projected Myocardial Uptake

FMMV values for the 65 datasets in the testing group before and after the registrations are plotted in Figure 9. Before any registration, FMMV was 11.3±9.0% for ACT and 20.1±22.7% for HCT. After manual registration, FMMV decreased to 1.5±1.5% ($p <$ 0.001) for ACT and 2.4±2.5% ($p < 0.001$) for HCT, while after automatic registration it decreased to 1.4±1.5% ($p < 0.001$) for ACT and 2.5±2.4% ($p < 0.001$) for HCT. The difference between the manual registration and the algorithm was statistically insignificant ($p = 0.397$ for ACT, $p = 0.636$ for HCT). The measured FMMV showed that a considerable mis-projection of myocardial uptake exists for the PET/CT data before registration, indicating the presence of quantification errors if no registration is performed.
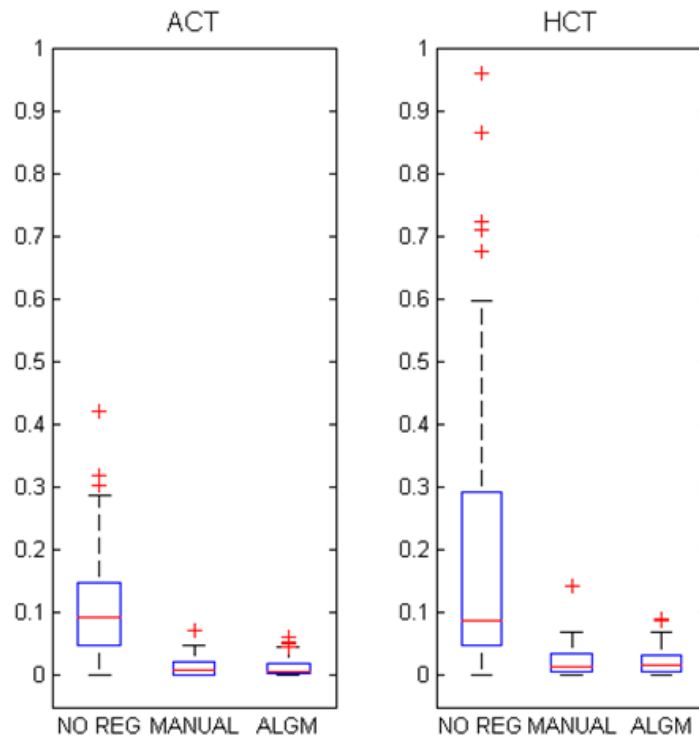
Figure 9. Measured FMMV for initial alignment (NO REG), after manual (MANUAL) and automatic (ALGM) registration. The results suggest that the HCT started out with more severe misregistration than did the ACT. Both manual and automatic registrations reduced FMMV to a similar level.

2.4.5 Example of Attenuation Artifact Reduction

In cases where severe misregistration was found in the PET/CT images, the automatic registration algorithm substantially reduced the registration error and the resultant attenuation artifact in the attenuation-corrected cardiac PET images. One example is shown in Figure 10.
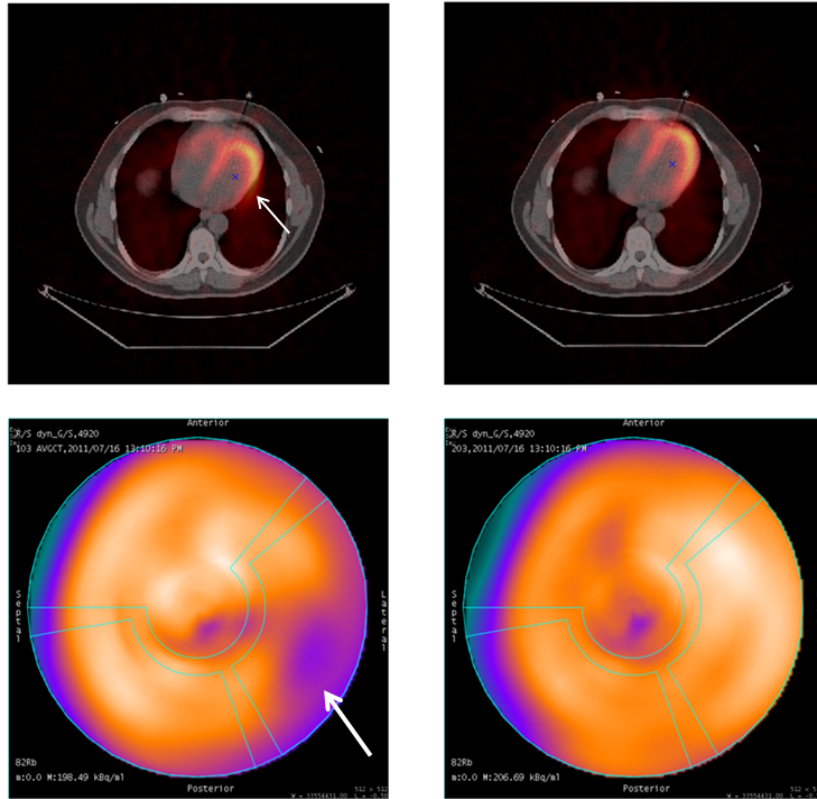
Figure 10. An example of dataset before and after registration. The original images were severely misregistered, which resulted in artifactual hypoperfusion in the lateral walls (white arrows). After automatic registration with our algorithm, the images were well registered and the artifact was removed. The misalignment was usually most severe along the M-L direction, but in this particular case it occurred along the A-P direction.

2.5 Discussion

We have developed a novel algorithm for the automatic registration of cardiac PET and CT images that is based on a 3D gradient correlation algorithm with a modified FCM method. The results from the algorithm were in good agreement with those from the manual registration, with the mean differences being less than 4 mm (and the maximum

differences being 9.0 mm for ACT and 8.6 mm for HCT). After optimization, the registration results compare favorably to previously reported approaches: in the studies conducted by Alessio *et al.* [53] with 5 patients and Bond *et al.* [55] with 26 patients, the mean translation differences were reported to be 6.6 mm (and the maximum 10.8 mm) and 8 mm (and the maximum 27 mm), respectively.

After the FCM clustering algorithm removes the information that does not contribute to – or may even confound – the image registration process, the gradient correlation can reach the maximal value only when the myocardium in the PET and CT images aligns well in all three orthogonal directions. As long as the segmentation is performed properly (i.e., with the appropriate α value selected), the maximal similarity index is expected to translate into minimal registration error between the PET and CT images. The simplicity of our similarity index enabled an efficient calculation of the algorithm and the adoption of an exhaustive search scheme.

The inter-observer variability of manual registration was demonstrated in this study. Surprisingly, the disagreement between the two observers was greater than 5mm in over 30% cases for both ACT and HCT datasets before reconciliation. This underscores the limitation of using manual registration as the reference when evaluating a registration algorithm. In this study, the difference between our algorithm and the manually performed reference registration is less than or comparable to the inter-observer variation within the manual registration. Assuming that a manual registration produces tolerable results, this suggests that cardiac PET/CT registered using our algorithm might be acceptable in the clinic.

The difference between ACT and HCT in our results demonstrated the advantage of the average CT protocol over helical CT in reducing misalignment in cardiac PET/CT. First, the initial misalignments along the S-I direction of ACT in the testing group are significantly lower than those of HCT (p = 0.012). The large initial misalignment along the S-I direction in HCT was likely due to the patients' holding their breath during acquisition and the longer separation in time between the acquisitions of the HCT and the stress PET scan. Secondly, when greater misalignment (>=10 mm) occurs, ACT tends to be less severe than HCT in terms both of frequency (9/65 vs 20/65, p = 0.021) and of extent (11.9±2.0 mm vs 18.8±10.2 mm, p = 0.030). Additionally, in HCT, two cases (3%) were found to have greater than 10 mm misalignment along the A-P direction, while in ACT the maximum misalignment along this direction was only 5.9 mm. These results suggest that ACT can largely compensate for the respiration-induced misalignment along the S-I and A-P directions. The remaining misalignment in the M-L direction most likely stems from the patient motion, which ACT alone cannot correct for.

The difference in FMMV between pre-registration ACT and HCT data is another indication of the advantage of ACT in reducing attenuation artifacts. Although the overall misalignment of ACT prior to registration was smaller, the average FMMV remained at 11%, suggesting that registration is still necessary in order to achieve accurate quantification. We did not include rotations in our registration modeling because ACT was able to reduce the misregistration to a simpler translational type of registration in the clinic [52]. The consequence of this can be perceived in the FMMV values: after manual registration, ACT has less activity remaining inside the lung than HCT

(FMMV$_{ACT}$=1.5±1.5%, FMMV$_{HCT}$=2.4±2.5%, p<0.001). This suggests that even after careful manual registration, ACT can still provide a potentially better attenuation map for cardiac PET than does HCT. The algorithm was able to reduce FMMV to a level similar to that achieved by manual registration for both ACT and HCT, indicating its effectiveness in reducing attenuation artifacts in cardiac PET.

The primary purpose of this study was to develop an automatic registration method and to evaluate its accuracy in registration with ACT and HCT. We did not evaluate the reduction of the attenuation artifact in the reconstructed PET image. This is a limitation of our study. However, by measuring and comparing FMMV values, we demonstrated that considerable mis-projection of the myocardial uptake exists in the PET/CT datasets without registration, and our algorithm achieved an FMMV reduction similar to that of the manual registration. Given that the attenuation artifact in the cardiac PET image is produced by such mis-projection, we believe our algorithm can achieve a similar artifact reduction to a level comparable to the manual registration. This observation needs to be verified by future work.

2.6   Conclusion

We have designed a novel automatic algorithm for the registration of cardiac PET and CT images and evaluated it in clinical datasets containing both ACT and HCT images. The registration results from our algorithm were compared to those from manual registrations performed by two human experts, and an objective metric, FMMV, was developed to characterize the fraction of mis-projection of the myocardial uptake inside the lung

tissues, which causes attenuation artifacts. Our evaluation of the results shows that our algorithm can mitigate the misalignment between the cardiac PET and CT data and reduce the activity mis-projection to a level similar to that of manual registration, suggesting the effectiveness of the algorithm in reducing attenuation artifacts. The algorithm is computationally efficient and potentially useful in a clinical setting. ACT is found to be advantageous over HCT in reducing the mismatch in cardiac PET/CT, but it still requires registration for accurate quantification.

Chapter 3: Reduction of Temporal Mismatch between PET and MR[1]

3.1   Abstract

Cardiac imaging is a promising application for combined PET/MR imaging. However, the current MR imaging protocols for whole-body attenuation correction can produce spatial mismatch between PET and MR-derived attenuation data owing to a disparity between the two modalities' imaging speeds. We assessed the feasibility of using a respiration-averaged MR (AMR) method for attenuation correction of cardiac PET data in PET/MR images. First, to demonstrate the feasibility of motion imaging with MR, we used a 3T MR system and a two-dimensional fast spoiled-gradient-recalled echo (SPGR) sequence to obtain AMR images of a moving phantom. Then, we used the same sequence to obtain AMR images of a patient's thorax under free-breathing conditions. MR images were converted into PET attenuation maps using a three-class tissue segmentation method with two sets of pre-determined CT numbers, one calculated from the patient-specific (PS) CT images and the other from a reference group (RG) containing 54 patient CT datasets. The MR-derived attenuation images were then used for attenuation correction of the cardiac PET data, which were compared to the PET data corrected with average CT (ACT) images. In the myocardium, the voxel-by-voxel differences and the differences in mean slice-activity between the AMR-corrected PET data and the ACT-corrected PET data were found to be small (less than 7%). The use of AMR-derived attenuation images in place of ACT images for attenuation correction did not affect the summed stress score. These results demonstrate the feasibility of using this SPGR-based MR imaging protocol to obtain patient AMR images and using those images for cardiac PET attenuation correction.

3.2   Introduction

The advent of hybrid positron emission tomography (PET)/magnetic resonance (MR) imaging systems offers the potential of superior diagnostic performance over PET/CT (computed tomography) in certain applications [61-65], including cardiac imaging [66-70]. However, respiratory motion can compromise the quantification of cardiac PET data using MR data. This issue was discussed in the previous chapter for the case of PET/CT: the respiratory motion–induced spatial mismatch between the emission data from PET and the attenuation data estimated from CT can cause moderate to severe artifacts in up to 40% of clinical cardiac PET/CT studies [42, 44]. This mismatch, which reflects the different breathing states captured by the respective imaging modalities, is largely due to the disparity in the modalities' imaging speeds [71]. Unlike PET data, which are averaged over several minutes, each CT slice is captured in less than one second. Similarly, in whole-body PET/MR imaging, MR images for attenuation correction, unlike PET data, are usually acquired using a breath-hold Dixon sequence, which takes about 18 seconds for each 21-cm bed position [36]. Examples of respiration-associated attenuation artifacts in clinical whole-body PET/MR have been reported by Keller *et al* [72]. The difference in image acquisition time suggests that artifacts caused by spatial mismatch can also occur in cardiac PET/MR imaging.

For cardiac PET/CT attenuation correction, the use of respiration-averaged CT (ACT) images has been reported to reduce respiratory motion-induced misalignment of PET and CT images [19, 20, 71]. Similarly, we posit that using respiration-averaged MR (AMR) images for attenuation correction could reduce misalignment between cardiac

PET and MR data and thus reduce myocardial perfusion artifacts in PET/MR images. As a proof of concept, in the present study, we 1) assessed a spoiled gradient recalled echo (SPGR)-based MR imaging protocol for obtaining cardiac AMR images under free breathing conditions, 2) demonstrated the feasibility of deriving attenuation maps from AMR data, and 3) evaluated this technique in a patient study.

3.3   Methods

3.3.1   Phantom Validation

To assess the effect of respiratory motion on the MR imaging protocol, we scanned a spherical phantom (diameter = 16.5 cm) containing 0.1% sodium azide using a 3T clinical MR imaging system (GE Discovery MR750) integrated with a motion-enabled table (ROCKER system, GE). The spherical phantom was fixed to the top of the table. Because the table is able to generate one-dimensional periodic motion along the axial direction of the scanner, it can be used to simulate respiratory motion, which is usually modeled as one-dimensional motion along the superior-inferior direction of the patient (i.e., the axial direction of the scanner). The table moves with a prescribed velocity and range; it pauses briefly at either end of the motion, leading to a trapezoidal motion track (Figure 11). In our experiment, we used a range of ±1.5 cm and a velocity of 1.5 cm/s, which resulted in a motion period of 4.88 seconds.
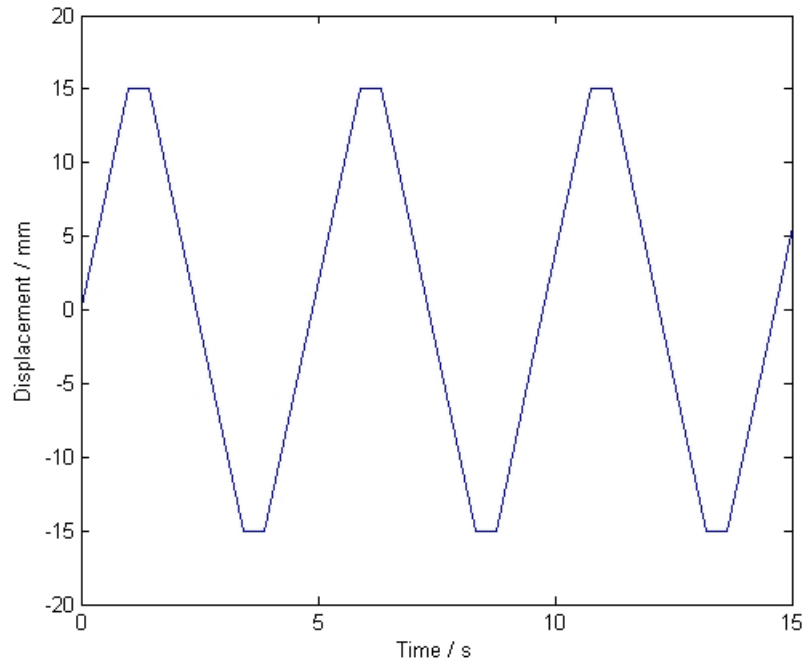
Figure 11. Motion trajectory of the phantom. Owing to a limitation of the motion system, a trapezoidal track was used instead of a sinusoidal one. The range (30 mm) and period (4.88 seconds) of the motion are reasonable approximations of human respiratory motion.

To obtain axial slices of the phantom under simulated respiratory motion, we performed an MR scan with a two-dimensional (2D) multi-slice, multi-phase, fast spoiled gradient recalled echo (SPGR) sequence (field of view = 260 mm × 260 mm, slice thickness = 5 mm, frequency/phase encoding = 128×128, repetition time [TR]/echo time [TE] = 3.0 ms/1.4 ms, flip angle = 20°, bandwidth = ±125 kHz) with a single-channel head coil. Fourteen temporal frames were acquired for each slice. Each frame's duration was 0.4 seconds, resulting in a temporal coverage of 5.6 seconds for each slice. A total of 30 slices were acquired, covering 150 mm along the axial direction. The scan duration was 169 seconds.

3.3.2 Patient PET/CT study

A patient who received a cardiac rubidium-82 (^{82}Rb) chloride PET/CT was recruited for the MR imaging, which was performed under free breathing conditions. The PET and MR images were acquired separately, not concurrently or simultaneously. Cardiac PET/CT was performed using a GE Discovery ST 16-slice PET/CT system with the patient in a supine, arms-up position. Dipyridamole stress testing with PET was performed over six minutes beginning 70 seconds after the start of ^{82}Rb infusion (1,295–1,850 MBq [35-50 mCi]). Dipyridamole stress testing was followed by a cine CT for ACT (8 × 2.5 mm X-ray collimation, 120 kVp, 0.5-second gantry rotation, 5.9-second cine duration) [18]. PET perfusion images were reconstructed with filtered back projection using a Butterworth filter with a cutoff frequency of 0.55, a "roll-off" value of 10, and a pixel size of 3.27×3.27 mm^2. Randoms were corrected by the option of singles, and scatter correction was applied.

3.3.3 Patient MR Study

For MR imaging, the patient was placed in an 8-channel torso coil and scanned using the GE 3T MR imaging system in a supine, arms-up position. Images of the patient's thorax and upper abdomen were obtained using the 2D multi-slice, multi-phase SPGR sequence used for the phantom, with slightly modified parameters (TR/TE = 3.7 ms/2.2 ms, flip angle = 20°, frequency/phase encoding = 128×128, field of view = 400 mm × 400 mm, slice thickness = 5 mm, bandwidth = ±125 kHz). In particular, TE was automatically determined by the console as the result of choosing the "in phase" setting, which ensures

that the phase difference between water and fat signals in the MR image is minimized. TR was automatically adjusted to account for the change in TE. Axial slices were acquired for attenuation correction of the PET images. A total of 30 slices were acquired, covering 150 mm along the superior-inferior direction. The acquisition time for each 2D frame was 0.48 seconds, and 12 temporal frames (5.76 seconds) were obtained consecutively to ensure continuous and sufficient coverage of at least one respiratory cycle for each slice location. The temporal coverage was close to 5.9 seconds, which was the duration chosen in a previous ACT study based on recorded breathing cycles for 600 patients [71]. The total scan duration was slightly less than three minutes, which is a typical PET acquisition time per bed position in oncology.

3.3.4   Data Processing

Previously developed segmentation-based methods produce attenuation maps that assign discrete attenuation coefficients for each tissue class. As a result, these methods cannot directly convert AMR images into synthetic ACT images, ACT_{AMR}, whose attenuation properties should reflect the motion blurring. Direct conversion from AMR to ACT_{AMR} can be potentially achieved with a pattern recognition or machine learning algorithm combined with a dedicated ACT/AMR atlas [73], or a fuzzy segmentation of the MR images. In the present study, we circumvented this problem by processing each MR image frame acquired at different temporal phases instead of processing AMR images. After each frame of the MR image was converted into a synthetic CT image, ACT_{AMR}

was derived as the average of all the frames for each slice. In other words, the averaging was performed on attenuation data rather than on MR data.

A simple three-class (air, lung, and soft tissue) segmentation approach [74-76] was adopted to convert MR images into synthetic CT images. To overcome the low signal-to-noise ratio and spatial inhomogeneity in each frame of the MR images, we implemented the following steps to achieve better segmentation. First, anisotropic diffusion filtering [77] was applied to reduce noise while preserving edge information. Then, sequential morphological erosion and dilation algorithms, which aim to remove small, isolated noise clusters that had been treated as "soft tissue" during the initial thresholding, were used to threshold-segment and refine the soft tissue. Bone voxels could not be separately identified in these MR images; instead, they were subsumed by the soft tissue class during segmentation. After the soft tissues were identified, the rest of the pixels in each 2D image were grouped into connected regions using a modified Moore-Neighbor tracing algorithm [78]. The region that contained pixels outside the body contour was identified as air, while all the non-tissue regions inside the body were identified as lung. After segmentation, predetermined CT numbers were assigned to each segmentation class in order to generate a corresponding synthetic CT image. Finally, the averaged attenuation images were derived as the pixel-by-pixel arithmetic mean of the individual synthetic CT images of all phases.

The assigned CT numbers for lung and tissue were determined by segmenting the CT images that were obtained in cardiac PET/CT. Non-anatomical components (the scanner table, blanket, etc.) were removed from the CT images, and then the lung was

segmented using a region-growing algorithm with a fixed upper threshold (-350 HU). Tissue was segmented by applying a lower threshold (-500 HU) and then excluding the segmented lung. Both fat and bone were thus included in the soft tissue class. Class-specific mean CT numbers were then calculated from the segmented tissue classes and used to create attenuation images.

We used two sets of CT numbers to generate attenuation images from MR data. In one set, patient-specific (PS) CT numbers were derived from the patient who underwent MR imaging. This set was created to ensure that the attenuation property of the created image matched that of the patient. In the other set, reference group (RG) CT numbers were computed by taking the mean of class-specific mean CT numbers from a 54-patient reference group. This set was created to ensure that average attenuation could also be used for attenuation correction. The average attenuation images derived using these two sets of CT numbers—ACT_{AMR-PS} and ACT_{AMR-RG}—were used along with the original ACT data for attenuation correction of the PET data.

Before performing attenuation correction, we digitally removed the scanner table from the ACT data so that the ACT data matched the AMR data. Both the ACT- and AMR-derived attenuation images were manually shifted to ensure good alignment with the emission images in the myocardial region. To reduce subjectivity, two independent observers verified the results of the manual registration. Attenuation correction of the PET data was then performed with the ACT- and AMR-derived attenuation images, the results of which are referred to as PET_{ACT}, PET_{AMR-PS}, and PET_{AMR-RG}, respectively.

3.3.5   Assessing Differences in Attenuation-Corrected PET Images

The quantitative difference in the myocardial region was evaluated. The myocardium was segmented in PET_{ACT} using a region-growing algorithm with the lower threshold set at 50% of the maximal myocardial activity. We evaluated the myocardial quantification difference between MR-based and CT-based PET data by comparing voxel-by-voxel difference and mean slice activity (MSA). To assess the potential clinical impact resulting from the quantification difference, we used a semi-quantitative five-point scoring system [79] to evaluate the perfusion map for each attenuation-corrected PET dataset, which was created by reformatting the myocardial PET data using a 17-segment model recommended by the American Heart Association [80]. The definitions of these quantities are described below.

For each voxel, the relative difference d_1 and absolute relative difference d_2 were computed as

$$d_1 = \frac{I - I_{REF}}{I_{REF}} \times 100\%$$

$$d_2 = \left| \frac{I - I_{REF}}{I_{REF}} \right| \times 100\%$$

Eq. 3-1

where I and I_{REF} represent the measured tracer concentration (Bq/cc) in each voxel. For a slice z, the MSA was first computed as

$$MSA_z = \frac{\sum\limits_{j \in M_z} I_{PET}(j)}{N_z}$$

Eq. 3-2

where *j* is the index for a voxel, M_z is the set of voxels in slice *z* that were identified as myocardium, and N_z is the size of M_z. For comparison, normalized mean slice activity (nMSA) was calculated as

$$nMSA_z = \frac{MSA_z}{MSA_{max}} \times 100\%$$

Eq. 3-3

where MSA_{max} is the maximal MSA of all slices in the attenuation-corrected PET datasets. The difference in MSA in slice z was calculated as

$$dMSA_z = \left| nMSA_{z,AMR} - nMSA_{z,ACT} \right|$$

Eq. 3-4

The polar perfusion maps were created with the Emory Cardiac Toolbox (ECToolbox, Atlanta, GA). Based on the amount of perfusion present in each segment, a score ranging from 0 to 4 was assigned automatically by the software as an indicator of cardiac perfusion function (0 = normal, 1 = equivocal, 2 = moderately reduced, 3 = severely reduced, 4 = absent).

3.4   Results

3.4.1   AMR Images of the Phantom and Patient

For both the phantom that included simulated respiratory motion and the patient under free breathing conditions, visual inspection of the acquired MR images revealed that the MR protocol could generate AMR images without visible motion artifacts and with

average motion blurring effect, which is crucial to the success of this technique (Figure 12). For the patient study, motion artifacts were not visible in the individual frames even when the images were displayed at the signal intensity level of the noise, indicating the effectiveness of the proposed MR protocol for free-breathing MR acquisition (Figure 13).
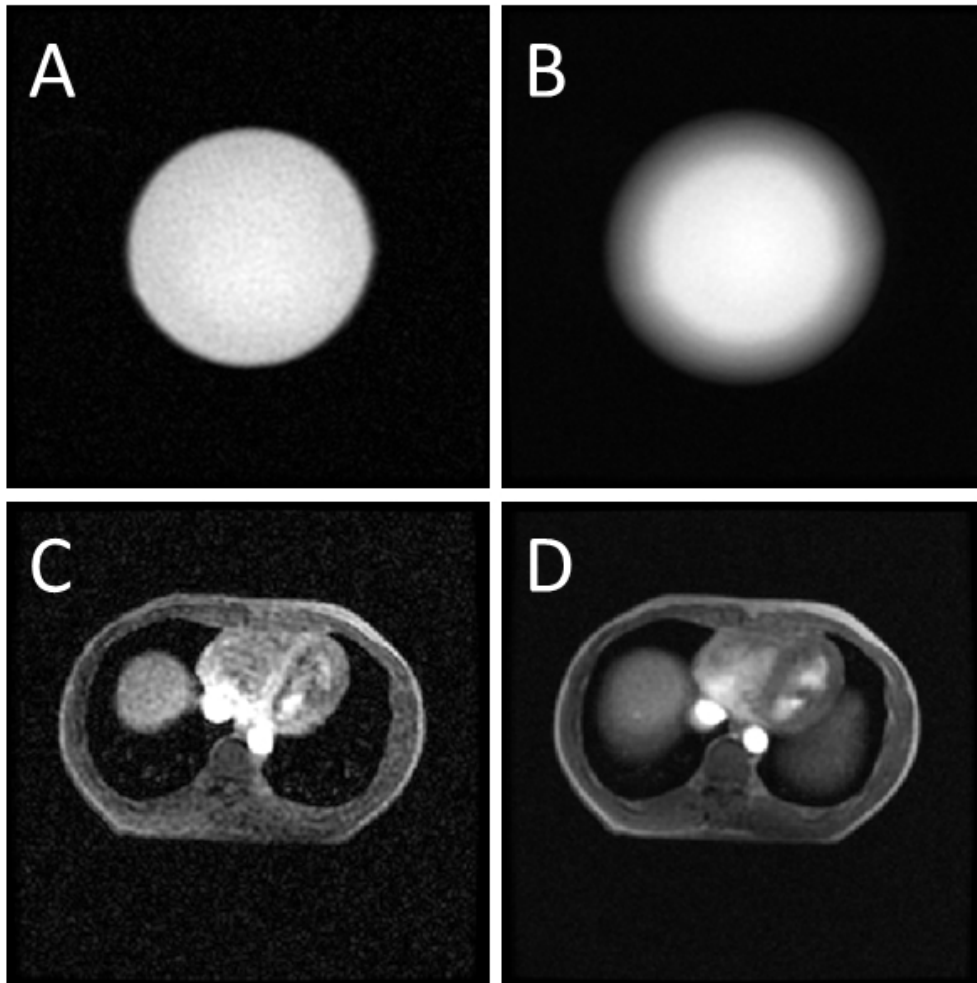
Figure 12. (A) A single-frame phantom image and (B) a corresponding motion-averaged phantom image; (C) a single-frame patient image and (D) a respiration-averaged patient image. Motion blurring is clearly visible in the averaged images.
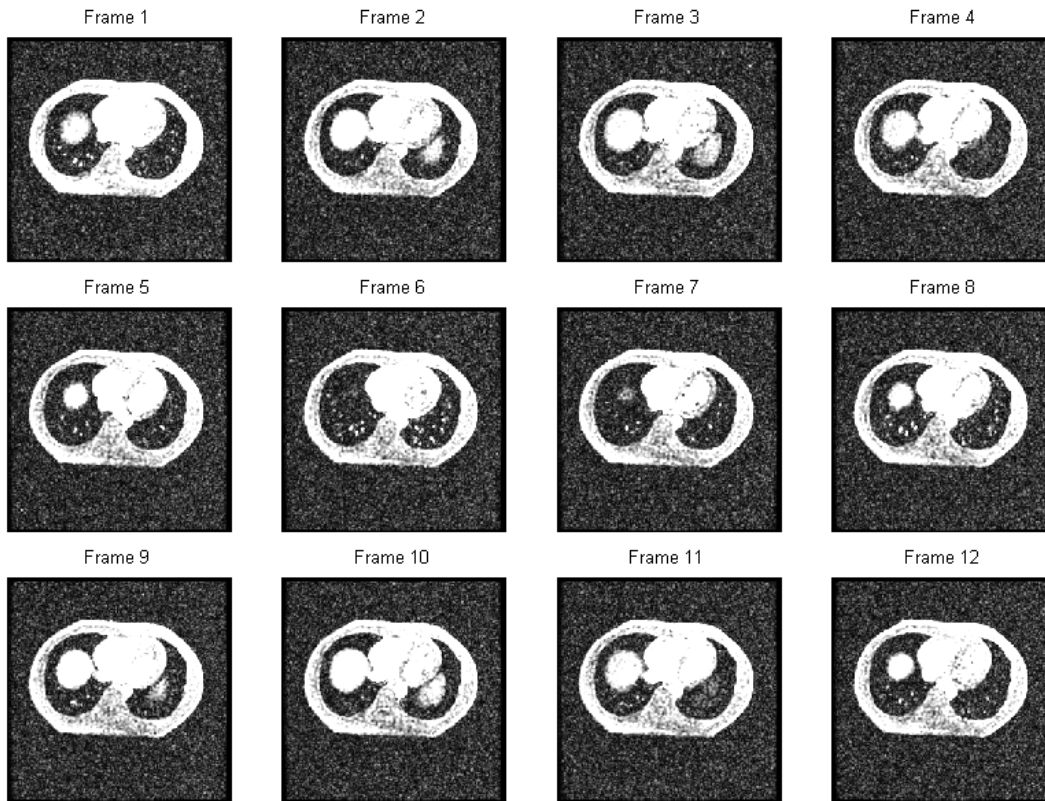
Figure 13. All twelve frames of one slice from the patient MR study acquired with the 2D FSPGR sequence. These frames are displayed at the signal intensity level of noise; motion ghosting artifacts that usually affect clinical MR images are not visible in these images, which were acquired under free-breathing, which indicates the effectiveness of the proposed MR protocol.

3.4.2 Class-specific Mean CT Numbers

The mean CT numbers calculated for lung and tissue were -726 HU and 47 HU, respectively, for the patient, and -727±51 HU and 4±18 HU, respectively, for the 54-patient reference group. The same segmentation parameters were used for all datasets.

3.4.3 Quantification of PET_{AMR}

Representative slices of the sagittal, coronal, and axial views created from AMR, ACT_{AMR-PS}, and ACT data are shown in Figure 14. With PET_{ACT} as the reference, the differences d_1 and d_2 of PET_{AMR-PS} were $-2.0\pm5.1\%$ and $4.3\pm3.3\%$, respectively; for $PET_{AMR-RG,}$ the differences were $-6.2\pm5.0\%$ and $6.3\pm4.8\%$, respectively.
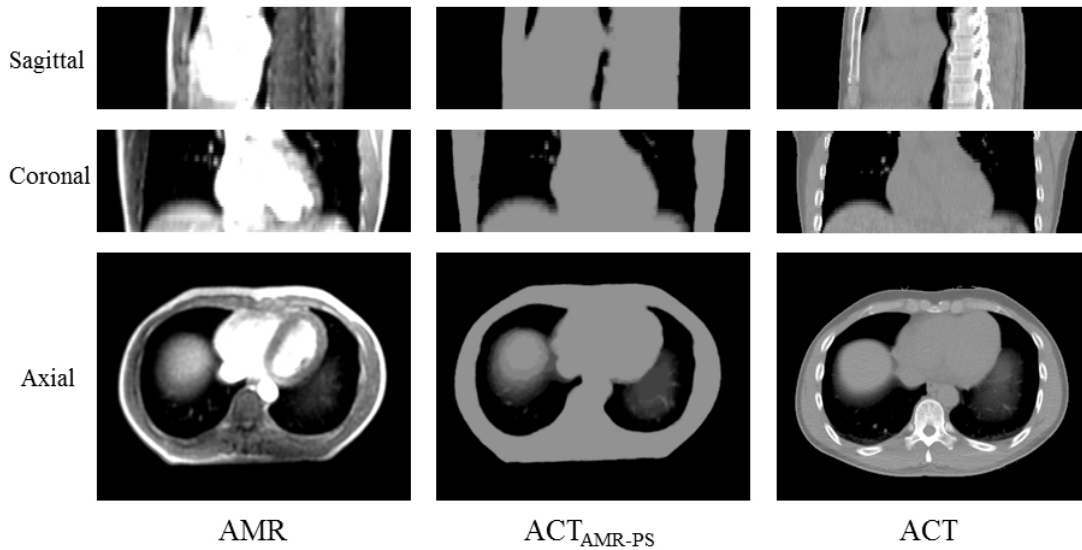
Figure 14. Representative slices of the sagittal, coronal, and axial views created from AMR, ACT_{AMR-PS}, and ACT data. Views created from the ACT_{AMR-RG} data, which are not visually different from those created from ACT_{AMR-PS} data, are not shown. ACT_{AMR-PS} and ACT images are shown with the same brightness and contrast. Respiration-averaging effects in the AMR images were preserved in the MR-derived attenuation images. Bones were included in the soft tissue class. Spatial mismatch between AMR and ACT images, which was the result of different table shapes, is clearly present in the dorsal area.

The nMSA values for different PET_{AMR-PS}, PET_{AMR-RG}, and PET_{ACT} slices are plotted in Figure 15. The highest MSA value was that of slice 7 of PET_{AMR-PS}, and this

value was used to normalize all three datasets. The absolute quantification difference in mean myocardial activity between PET_{AMR-PS} and PET_{ACT} at different slices was 2.0±1.6%; the maximum difference was 5.0%. The absolute quantification difference between PET_{AMR-RG} and PET_{ACT} was 4.7±2.5%, with a maximum difference of 8.8%.
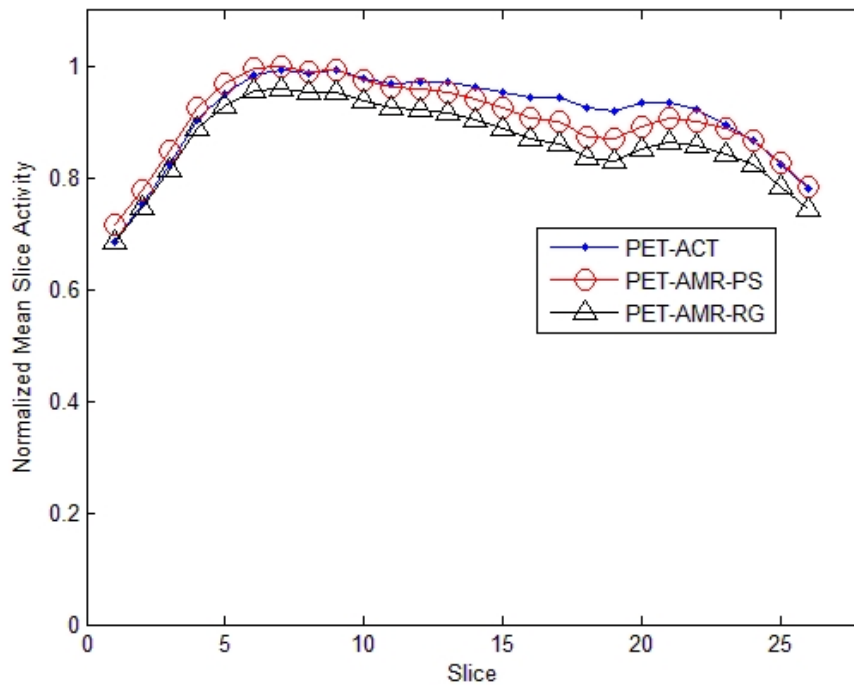
Figure 15. Mean myocardial uptake in different slices normalized to maximal mean uptake. The slices are labeled from the most superior slice to the most inferior slice. The three curves are from PET corrections with ACT, AMR-PS (patient specific) and AMR-RG (reference group).

Reformatted PET images (PET_{ACT}, PET_{AMR-PS}, and PET_{AMR-RG} images) of the myocardium along the short axis, horizontal long axis, and vertical long axis are shown in Figure 16. The PET images of the left ventricle in the attenuation-corrected PET images were reformatted into the polar maps using the 17-segment model. In the original ACT-

corrected PET image, the summed stress score was 0, indicating normal cardiac function. The scores in all segments were the same in both AMR-corrected PET datasets (Figure 17).
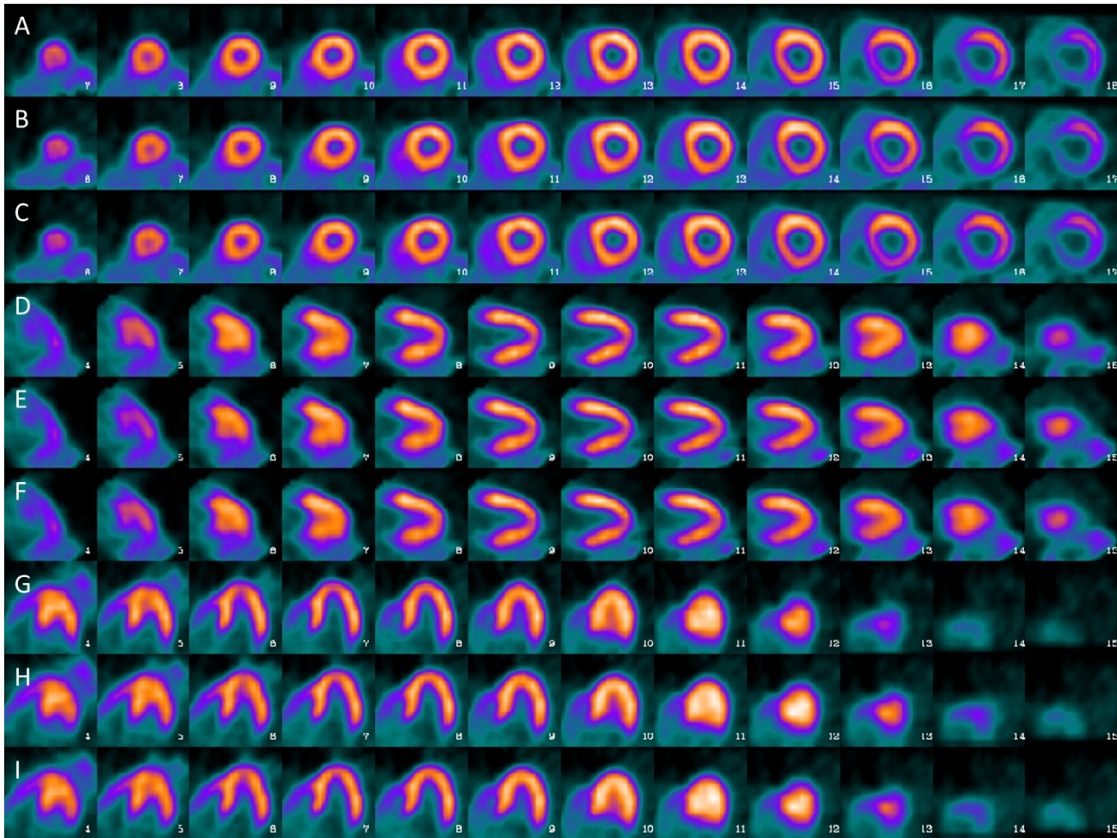
Figure 16. Reformatted myocardial PET images showing different cardiac axes, in which rows A–C are short-axis views, rows D–F are horizontal long-axis views, and rows G –I are vertical long-axis views. In each three-row section, the PET$_{ACT}$, PET$_{AMR-PS}$, and PET$_{AMR-RG}$ images appear in sequence from top to bottom.
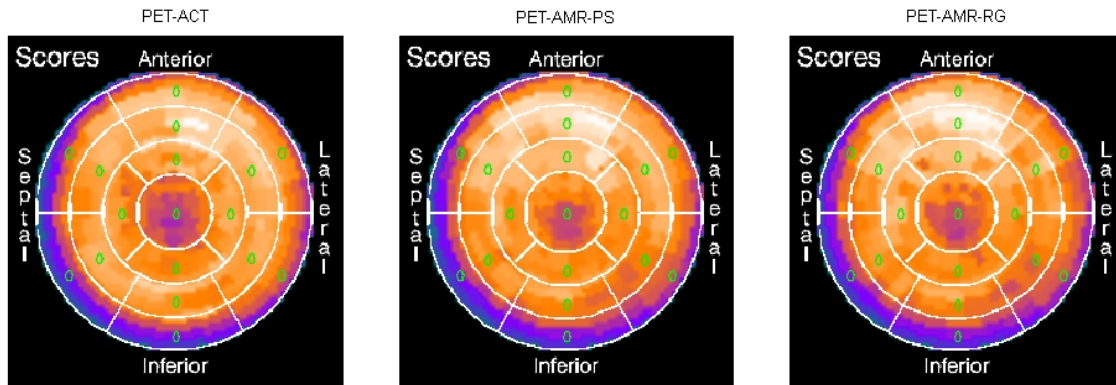
Figure 17. PET$_{ACT}$, PET$_{AMR-PS}$, and PET$_{AMR-RG}$ myocardial perfusion images. Stress scores were assigned to each segment. The patient had normal cardiac function, with a summed stress score of 0 in the PET$_{ACT}$ image. Using MR-derived attenuation images for attenuation images for attenuation correction did not affect the stress scores.

3.5   Discussion

The different patient tables of the MR system and the PET/CT system caused a visible spatial mismatch between AMR and ACT images in the dorsal area of the patient (Figure 14) because the MR system's table has a flat surface, whereas the PET/CT system's table has a curved surface. This mismatch, which would not be an issue in a combined PET/MR system, most likely contributed to the underestimation of the cardiac activity in PET$_{AMR-PS}$ and PET$_{AMR-RG}$. In the present study, we reduced the effect of this spatial mismatch on the PET quantification by ensuring good alignment of the attenuation images and emission images in the myocardial region. This was achieved by manual

registration, which is the typical approach to correcting misregistration between cardiac PET and CT images [44].

In a previous phantom-based study, Bin *et al.* [28] found that reconstructed PET activity can be underestimated by 10%-20% if one does not correct for the attenuation that is introduced by the MR system's table. Our phantom experiment using the PET/CT system, with its curved table, produced similar results. Therefore, the imaging system table must be considered in order to accurately quantify PET data. In the present study, we attempted to incorporate the PET/CT system's table into the AMR-derived attenuation images. Unfortunately, this proved to be difficult owing to the mismatch of the patient's body contour resulting from the different shapes of the two tables. For the purpose of a fair comparison, therefore, we digitally removed the table from the ACT images before performing the attenuation correction.

As a proof of concept, we used a three-class segmentation scheme to derive MR-based attenuation images. Despite its simplicity, this method achieved relatively accurate quantification in the reconstructed PET images. While creating the attenuation map from AMR images, we did not perform bone segmentation. Bone segmentation is difficult without the aid of a dedicated ultrashort-echo-time imaging sequence. To date it has been mainly applied in PET/MR imaging of the brain [37, 38]. In brain PET, quantification bias have been attributed to having ignored bone [81]. In whole-body PET/MR imaging, however, neglecting bone in segmented attenuation images has been thought to cause large errors only in regions that are inside or near bones [82-84]. In one example demonstrated by Samarin *et al.* [84], classifying bone as soft tissue resulted in a

difference of less than 6% for PET voxels in the heart region. Ouyang *et al.* [85] also concluded that the three-class segmentation can be sufficient for PET quantification in the heart, as it yields less than 5% quantification difference after compensation. These studies indicate that bone segmentation may not be necessary for cardiac PET/MR.

Martinez-Moller *et al.* [36] proposed using a four-class segmentation scheme with the Dixon technique, in which fat is separated from non-fat soft tissue and assigned a different attenuation coefficient. Although evaluating different segmentation-based attenuation correction methods was beyond the scope of our study, it should be noted that the Dixon technique can be integrated into our proposed AMR protocol with a modification of the MR sequence to separate fat and non-fat soft tissue while maintaining similar temporal resolution. Such an approach may improve PET quantification in patients with higher body-fat composition.

To investigate the effect of the assigned CT numbers on quantification, we created two sets of attenuation images from MR data: ACT_{AMR-PS} and ACT_{AMR-RG}. As expected, ACT_{AMR-PS} resulted in a smaller quantification difference because of the more accurately estimated attenuation coefficients for the patient. In clinical PET/MR applications, however, patient-specific CT images are usually unavailable, and general coefficients must be used for attenuation correction. In the present study, the mean lung CT number of the patient (-726 HU) was close to that of the reference group (-727±51 HU); however, a Student's t-test revealed that the patient's mean tissue CT number was significantly higher than that of the reference group (47 HU vs 4±18 HU, p<0.001). As a result, the quantification difference in the ACT_{AMR-RG}-corrected PET data (6.3%) was

higher than that in the ACT_{AMR-PS}-corrected PET data (4.3%). However, the error was small. For patients whose mean attenuation coefficients or CT numbers deviate less from the population mean, a smaller quantification difference is expected. AMR-based attenuation correction did not affect the summed stress score, indicating that the quantification difference is not clinically significant in this one case. Further investigation is required to evaluate the clinical effect of this method of MR-based attenuation correction.

Several authors have proposed MR-based respiratory motion correction for thoracic PET/MR [86-89], and at least one phantom-based study tested a tagged MR imaging–based technique for cardiac motion correction [90]. Although such approaches aim to eliminate the effect of motion on the reconstructed PET image, they usually require non-standard MR sequences that are not clinically available. In contrast, the approach we propose uses a scheme that has proven effective in PET/CT to reduce the spatial mismatch between emission and attenuation data and the consequent artifact in the cardiac perfusion PET image. The present study's findings suggest that a similar improvement can be achieved in cardiac PET/MR imaging without resorting to motion correction.

In the present study, we tested the feasibility of using AMR images of the thorax to create attenuation maps for cardiac PET data. As a proof of concept, we designed a simple strategy to include the motion blurring effect by processing the images of individual phases. This strategy does not fully capture the motion blurring effect and is a

potential limitation of this study. However, the quantification errors were small, suggesting that this simple strategy is feasible.

3.6   Conclusion

The findings of the present study demonstrate the feasibility of using AMR images for attenuation correction of cardiac PET data. Despite the fact that the different tables of the MR and PET/CT systems caused a geometrical mismatch of the AMR-based and ACT-based attenuation images, the PET data corrected with the MR images achieved accurate quantification and maintained the same summed stress score. Further study with more patients is warranted to determine the effectiveness of AMR-based attenuation correction in cardiac PET/MR imaging.

Chapter 4:   Effect of Bone Identification

Sensitivity on PET Quantification Accuracy

4.1 Abstract

A tissue-classification-based attenuation-correction strategy has been proposed as a solution for correcting bone attenuation in PET/MR imaging. The feasibility of this approach has been investigated by previous CT-simulated studies. However, the unique problem of voxel averaging associated with bone but not soft tissue has been largely overlooked in the past, and this study aims to investigate the issue related to voxel averaging of bone and the effect of bone identification sensitivity in attenuation images on the quantification of PET in bones. Data from eight NaF PET/CT studies of the skeleton were retrospectively obtained for this study. The CT attenuation images were used to simulate MR-derived attenuation images with various bone identification sensitivities, which was achieved by estimating the volumetric fraction of bone inside a voxel from its CT HU value using a linear signal model. The simulated attenuation images were then used for PET attenuation correction. The PET quantification difference was evaluated in 139 NaF-avid bone sites identified in the skull, pelvis, ribs, vertebral processes and vertebral bodies. The omission of bone identification caused a difference of -10.3%±5.6% in the evaluated bone sites (-20.3%±4.1% for lesions in the skull and -8.5%±3.6% for non-skull lesions). No significant difference was found between lesions in the pelvis and vertebrae. A non-monotonic relationship between bone identification sensitivity and PET quantification accuracy was observed, with the minimal quantification difference achieved at a bone volume fraction (BVF) around 40% for skull lesions (2.0%±1.6%) and 30% for non-skull lesions (1.3%±1.0%). This study further

76

demonstrated the feasibility of a tissue-classification-based approach for attenuation correction of bone in PET/MR.

4.2   Introduction

Since its commercial introduction in 2010 [24, 26], the application of combined positron emission and magnetic resonance imaging has been growing steadily. By February 2014, more than 50 whole-body PET/MR systems had been installed worldwide for clinical use [27]. Promising applications of PET/MR include neurology, cardiology and oncology (especially pediatric oncology), as well as clinical research. Compared to PET/CT systems, PET/MR delivers significantly less radiation dose to the patients during imaging, can provide images with superior soft tissue contrast, and has the potential to realize contemporaneous multi-parametric functional imaging [91, 92], real-time motion tracking and correction [21].

However, PET/MR systems face a number of challenges that need to be addressed before the combined modality can reach its full potential. Among these factors, inaccuracy in generating correct attenuation coefficients using MR-based approaches, which can compromise PET quantification accuracy for the combined PET/MR systems, has been recognized as one of the weakest points in current PET/MR technology [27]. First, scanner accessories such as the patient table, positioning aids and the MR RF coils create additional photon attenuation even though they cannot, in general, be visualized in the MR images, and thus require special means of correction. Second, for materials that

can be visualized in MR images, the MR signal reflects the proton density of the material weighted by its magnetic relaxation properties (T_1 and T_2) and not the material's photon attenuation properties. Therefore, MR is not directly translatable into the 511 keV photon attenuation coefficients that are required for PET attenuation correction. In order to obtain a patient-specific attenuation map from MR images, two different approaches have been proposed.

One of the approaches derives a patient-specific attenuation map from the information in an established MR-attenuation map atlas. This approach can produce attenuation maps from MR images that have a high visual similarity to CT images and that produce accurate PET quantification. However, the atlas approach cannot reflect the range of possible anatomical anomalies, such as patients whose anatomy had been distorted by surgery. The second approach of deriving MR-based PET attenuation maps involves classifying or segmenting the MR images into different tissue categories followed by assigning standard tissue-specific attenuation coefficients to each voxel based upon its assigned class. Due to its simplicity and flexibility, all of the commercially available PET/MR models have used the tissue-classification approach. Usually either three-class (air, lung and soft tissue) [74] or four-class (air, lung, fat and non-fat soft tissue) [36] methods are employed.

Despite the substantial difference in attenuation properties, bones are not recognized as a separate tissue class but instead are included in the soft tissues in the attenuation maps provided in current clinical PET/MR systems. A number of studies have

demonstrated the necessity of distinguishing bone as a separate tissue-class for improved PET quantification, especially in brain imaging and for voxels adjacent to or inside bones [84, 93-95]. The omission of bones from the MR tissue-classification-based attenuation correction approach is largely due to the difficulty in identifying bone in MR images: first, the number of protons in bones that are visible to the MR scanner is only about 20%-25% of that in soft tissues [96]; second, the transverse relaxation time, T_2, of bones is substantially shorter than those of soft tissues (<=1ms vs 10~100ms), leading to a rapidly decaying signal that cannot be captured by conventional MR sequences. These two challenges are well-recognized and have been discussed extensively in the MRI and PET/MR literatures. In order to address these difficulties, ultra-short-echo-time MR sequences, which can capture the signal of bone before its disappearance by utilizing an extremely short TE, have been proposed to overcome these challenges [37, 38]. These techniques have been applied to head imaging and, although still facing challenges [97, 98], can potentially provide bone information for attenuation correction in whole-body PET/MRI systems. A few previous CT-simulated studies have shown that identifying these partially bone voxels is indeed a valid approach to correct for bone-induced quantification inaccuracy [93, 99].

However, another important challenge of clinical bone imaging has heretofore been largely ignored in the literature of MR tissue-classification-based attenuation correction: the relatively small size of bone and the consequent intra-voxel averaging of bone and non-bone tissues. In the anatomical sense, bones are visible organs with sizable volumes that can be easily identified in gross anatomy. However, the material

composition of bone is highly heterogeneous, and the "hard-tissue" part of bones (the part with a high attenuation coefficient which is difficult to image using MRI) is usually very thin (with a few exceptions such as the skull and the long bones found in the extremities). The thickness of the cortical layer of bones in the torso, such as the vertebrae and ribs, can be around 1mm or less [100, 101]. One millimeter is substantially smaller than the dimensions of most soft tissues structures (~10 mm or more). Because the voxel sizes used in clinical tomographic imaging are generally on the order of 1-3 mm, the mixing of bone with other tissue types within a single voxel cannot be neglected, as it can be in the case of soft tissues whose dimensions are appreciably larger than the voxel size. In clinical tomographic imaging, the fraction of bone within a voxel can take any value between 0 and 1, because of the uncertainty of the location and orientation of the bone structures in relation to those of a voxel.

	Air Lung Tissue	0.3% 13.1% 4.2%	Air Lung Fat Tissue	0.3% 13.1% 36.3% 15.8%	Air Lung Fat Tissue Bone	0.3% 13.1% 36.3% 21.9% 50.4%
Percentage of voxels located on the interface:						
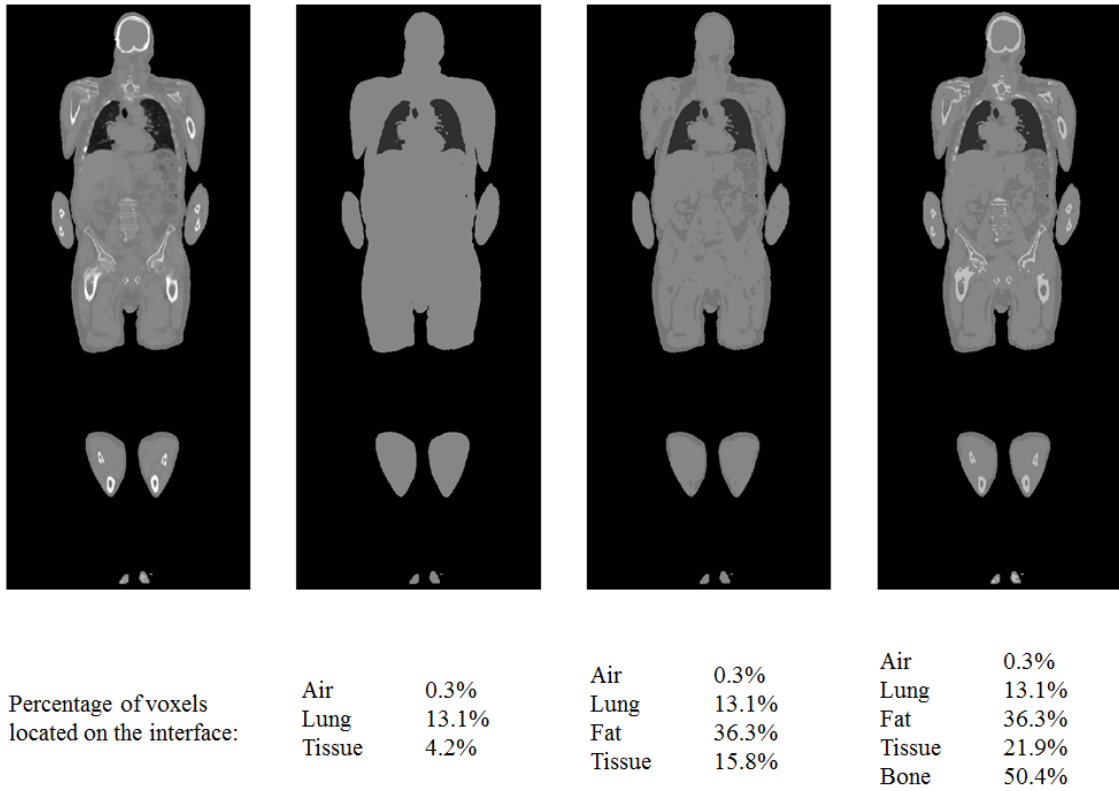
Figure 18. To intuitively illustrate the extent of intra-voxel averaging for different tissue types, a 3D whole-body CT dataset was classified into different tissue categories. The percentage of voxels located on the interfaces of different tissues, which are potentially subject to intra-voxel averaging, is recorded for tissue-classification methods. The images displayed here are, from left to right, the original CT, the three-class segmentation, the four-class segmentation and the five-class segmentation. The CT dataset used here has a typical voxel size for attenuation images (1.5 mm × 1.5 mm ×3.0 mm). In this case, the percentage of bone voxels on the tissue interface is greater than 50%, indicating that there is a substantial intra-voxel averaging for bone.

The measured value of a voxel under intra-voxel averaging deviates from those of homogeneous voxels, which can be estimated as the average of the values of the composing tissue types weighted by their respective volumetric fractions within this

voxel. It should be noted that the relationship between the composition of a voxel and the value representing its characteristic can be nonlinear when such value is not directly measured but rather derived (Figure 19). For the imaging of bone, the continuous distribution of volumetric bone fractions inside voxels is the primary reason why bone voxels have a much wider HU range than soft tissues on a typical CT histogram (Figure 20).
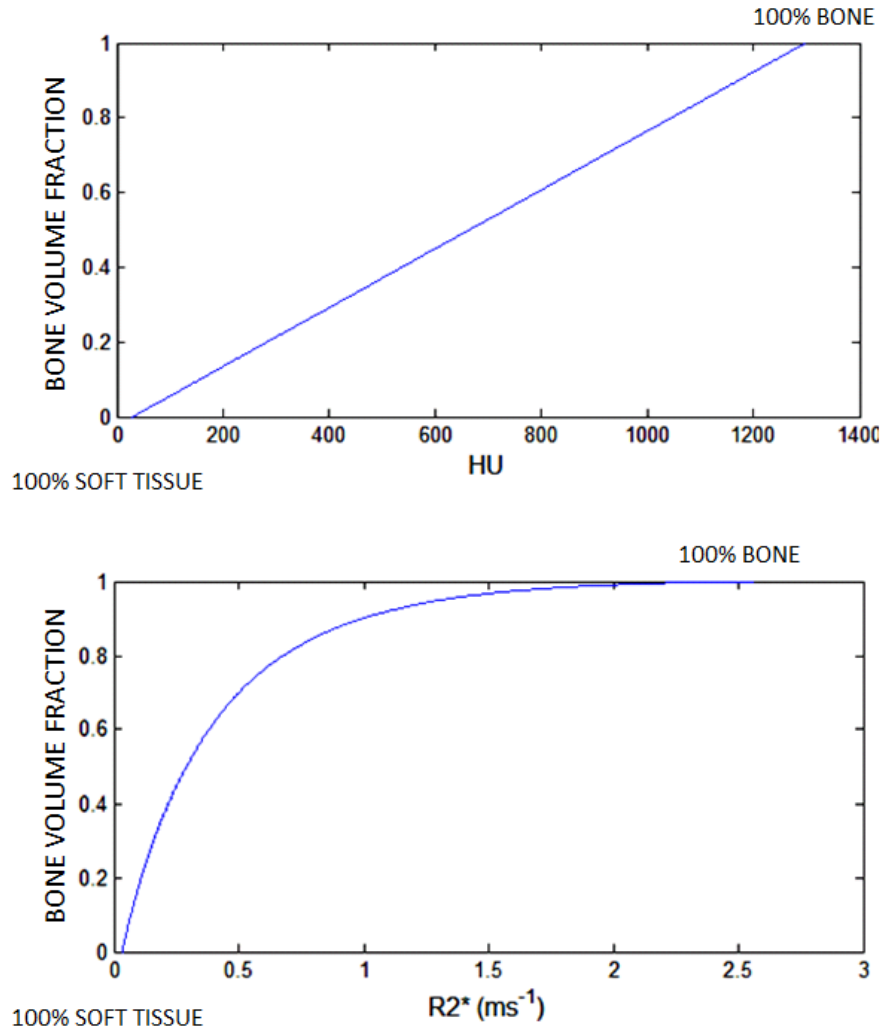
Figure 19. Simulated relationship between BVF and HU in CT (tissue - 30 HU, bone - 1300 HU) and between BVF and R_2^* (tissue - 0.03 ms^{-1}, bone - 2.56 ms^{-1}) in MR under a noiseless scenario. The simulation of R_2^* also assumed $T_1 = 1400$ ms for soft tissue and $T_1 = 223$ ms for bone, and that proton density in bone is 25% of that in soft tissue. TE and TR in the simulation of MR signals are from Keereman et al. (J Nucl Med, 2010. 51(5): p. 812-8). HU is directly measured from CT, while R_2^* has to be derived from multiple MR images, which, because of the exponential T_1 and T_2^* relaxation, led to a nonlinear relationship between BVF and nominal R_2^* of voxels.
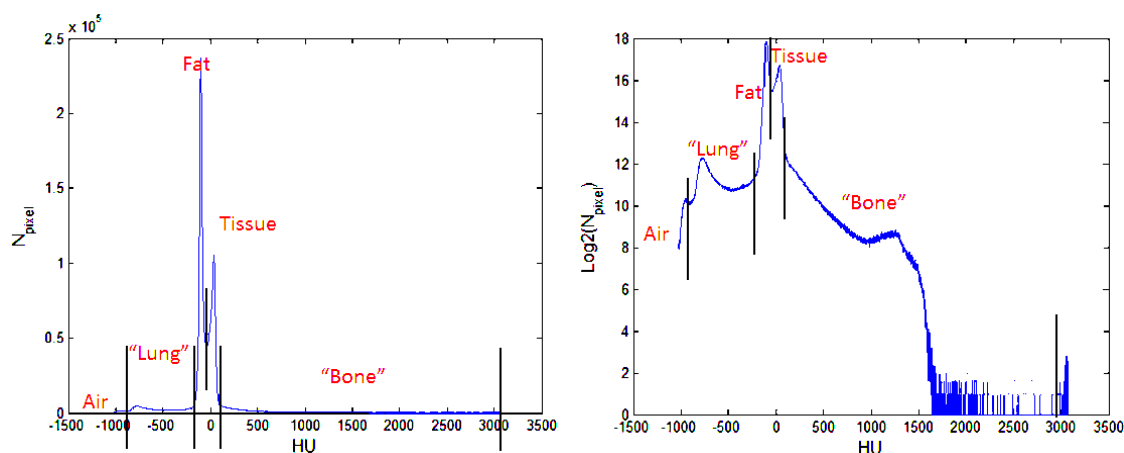
Figure 20. Histogram of a typical whole-body CT dataset (all voxels outside the patient body were excluded), plotted in linear scale (left) and in logarithmic scale (right). Both soft tissue and fat have a narrow distribution on the HU spectrum, while lung and bone have substantially wider distribution from intra-voxel averaging. For "bone voxels", it can be clearly seen on the logarithmic plot that the number of voxels on the lower HU end (representing voxels of lower BVF) is much greater than the voxels one the higher HU end (representing voxels of higher BVF).

A few previous CT-simulated studies have shown that, despite the presence of substantial voxel averaging, identifying voxels that are partially bone and then assigning a single attenuation coefficient is an effective approach to correct for bone-induced quantification inaccuracy [85, 93, 99]. However, these studies generally used rather low HU thresholds (representing voxels of low BVF) when simulating the segmentation of bone in MR. In other words, these studies simulated the scenario that MR has a high sensitivity in bone identification, similar to that of CT. Given that MR is inherently ill-suited for bone imaging and may never be able to achieve the high sensitivity level in previous CT-simulated studies, it is unclear whether binary-classification method remains

a viable approach to correct for the bone-induced photon attenuation in PET/MR when the sensitivity of bone identification is limited in MR-based attenuation images.

This study examined the relationship between the PET quantification accuracy and the sensitivity of bone identification in the attenuation image in an attempt to establish the requirement for accurate quantification of bone uptake in PET/MR. We simulated the scenarios of various bone identification sensitivity in MR-based attenuation images with the CT images acquired during PET/CT scans. This is possible because there is the excellent contrast between bone and soft tissues in CT. We determined the proper attenuation coefficients to be assigned to bone for each level of sensitivity and then evaluated the associated quantification difference inside bone.

4.3   Methods

4.3.1 ^{18}F-Sodium Fluoride PET/CT Data

^{18}F-sodium fluoride (NaF) is a radiotracer developed for skeletal imaging. It has been clinically used to evaluate metastatic bone diseases in oncology [102]. Image data of eight patients (five male, three female, age 57.5±16.5 yr, weight 92.1±19.8 kg) who had undergone whole-body ^{18}F-NaF PET/CT exams at The University of Texas MD Anderson Cancer Center were retrospectively obtained for this study. The studying of these patient data was approved by the Institutional Review Board of The University of Texas M. D. Anderson Cancer Center. All of the PET/CT exams had been performed on a Siemens Biograph mCT flow PET/CT scanner. The injected NaF doses were 9.0±0.5

mCi. After an uptake time of 47.4±8.9 minutes, whole-body CT attenuation data and PET emission data were acquired from the vertex of the skull to the toes. The CT data were acquired with 140 kVp (except for one exam that used 120 kVp), pitch factor = 1.4, and collimation = 16×1.2 mm and were reconstructed into images with 512×512 matrices with a 1.5 mm transverse voxel size. The PET data were acquired in 3D mode and reconstructed into 200×200 matrices with a 4.1 mm transverse voxel size. Both datasets have 3 mm slice thickness and 2 mm slice spacing. PET reconstructions were performed using the "UltraHD-PET" option, which includes correction for the point spread function of the PET system and for time-of-flight correction, using two iterations, 21 subsets and a 5-mm FWHM Gaussian filter. The same parameters were used for all PET reconstructions in this study.

4.3.2　Estimation of intra-voxel averaging between bone and soft tissues

The HU value in CT reflects the overall attenuation property of a voxel. For a voxel that contains multiple tissue types, the attenuation of the voxel is the mean of the attenuation of each tissue type that it contains, weighted by the volumetric fraction of each type and ignoring noise:

$$HU(x, y, z) = \sum_{n} c_n(x, y, z) HU_n \text{ , where } \sum_{n} c_n(x, y, z) = 1 \qquad \text{Eq. 4-1}$$

In this equation c_n denotes the volume fraction of tissue type n. In this study, the primary concern was the voxel averaging between soft tissue (without differentiating

between fat and non-fat tissues) and bone. The scenarios of voxels containing more than two different tissue types were not considered. Using the Bone Volume Fraction (BVF) to replace c_n in the dual-tissue-type scenario, equation 4-1 becomes:

$$HU(x, y, z) = BVF(x, y, z) \cdot HU_{bone} + [1 - BVF(x, y, z)] \cdot HU_{tissue} \qquad \text{Eq. 4-2}$$

And BVF can be solved for as

$$BVF(x, y, z) = \frac{HU(x, y, z) - HU_{tissue}}{HU_{bone} - HU_{tissue}} \times 100\% \qquad \text{Eq. 4-3}$$

The linear relationship between the volumetric fraction of bone and HU values measured with clinical CT scanner has been demonstrated for *ex vivo* situations [103]. This linear relationship is also assumed in the CT-based attenuation correction in the step that converts the CT images into the 511 keV photon attenuation maps of PET.

In order to estimate the bone volume fraction for voxels, an assumption was made that the HU variation of homogenous soft tissue voxels (BVF=0) and homogenous bone voxels (BVF=1) are small enough to be essentially considered as constant given the large HU difference between these two types of tissues. This is a reasonable assumption for both fat and non-fat soft tissues, which have little intra- and inter-patient variation in images from a properly calibrated CT scanner. In this study, HU_{tissue} was set as 0, the HU value of water.

However, assuming constant HU values for "homogeneous" bone voxels in clinical patient datasets is less acceptable, and will lead to greater inaccuracy when

estimating BVF from HU values unless additional correction is performed. This is primarily caused by the polychromatic nature of the X-ray beams that are generated by the X-ray tube of CT scanners. Instead of ideal, monoenergetic X-ray photons, the photons produced by CT scanners have a continuous distribution on the energy spectrum. Photons of lower energy are attenuated by the patient more strongly per unit distance than are the ones with higher energy. Thus, the effective energy of the beam increases as the beam penetrates deeper into the tissues, resulting in a variation of the measured HU values along the path of the beam. This is known as beam hardening. Although theoretically this would cause HU inaccuracy in all HU values, in reality it is minimized around 0 HU because of the calibration procedures and built-in correction algorithms of CT scanners. However, this does not hold true for HU values in the higher range, as can be seen in the results of our phantom experiment.

4.3.2.1 The effect of beam hardening on HU values

In order to demonstrate the impact of beam hardening on the HU values, an anthropomorphic knee phantom was scanned with the CT component of a GE Discovery 690 PET/CT scanner using four different setups that created different degrees of beam hardening effects (Figure 21). Those different levels were obtained by employing different amounts of additional attenuating material in various scans. All of the CT data were acquired with the same scanning parameters: 120 kVp, 300 mAs, pitch factor =

0.984, and 40×0.625 mm collimation and were reconstructed into images with a 0.98 mm transverse voxel size, a 0.625 mm slice thickness and a 0.625 mm slice spacing.

Voxels of homogenous "soft tissue" and "bone" were segmented with HU thresholding (soft tissue: [0 HU, 100 HU], bone: [1000 HU, ∞]) followed by morphological operations to erode the segmented masks isotropically by one voxel. The segmented voxels came only from the knee phantom proper, and the voxels within the added attenuation materials were excluded from the analysis. As can be seen in Figure 22, the HU values for soft tissue voxels remained essentially the same, while a considerable difference in the HU values in the bones was induced by the increased amount of attenuation and beam hardening within the reconstructed CT images.
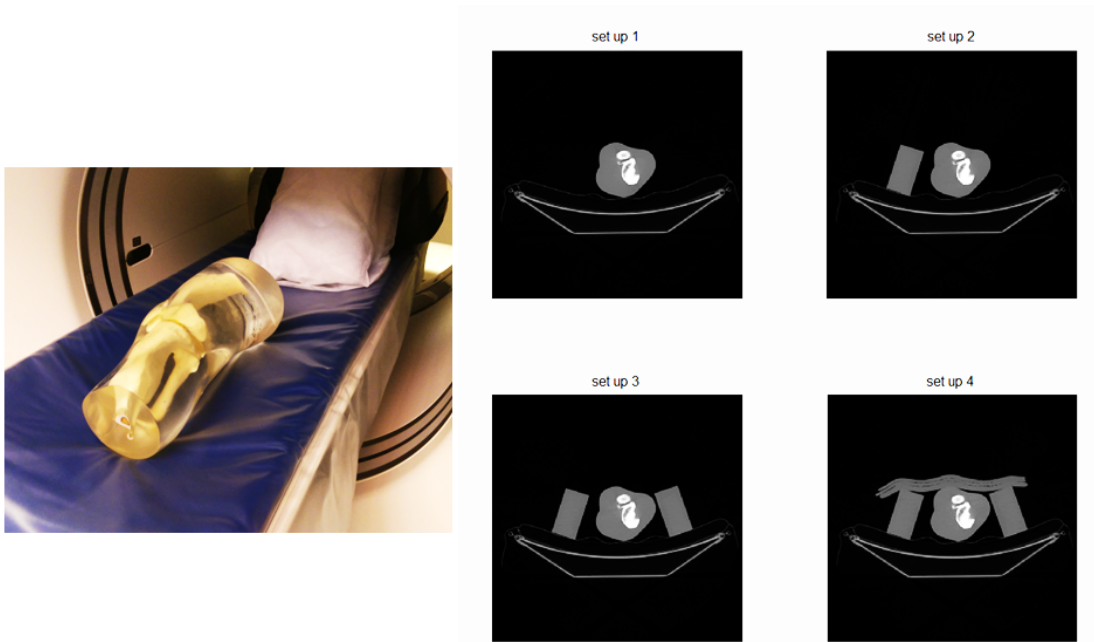
Figure 21. The anthropomorphic knee phantom and the scan setups used to verify the impact of beam hardening on HU values. The amount of total attenuation increases monotonically from setup 1 to setup 4.
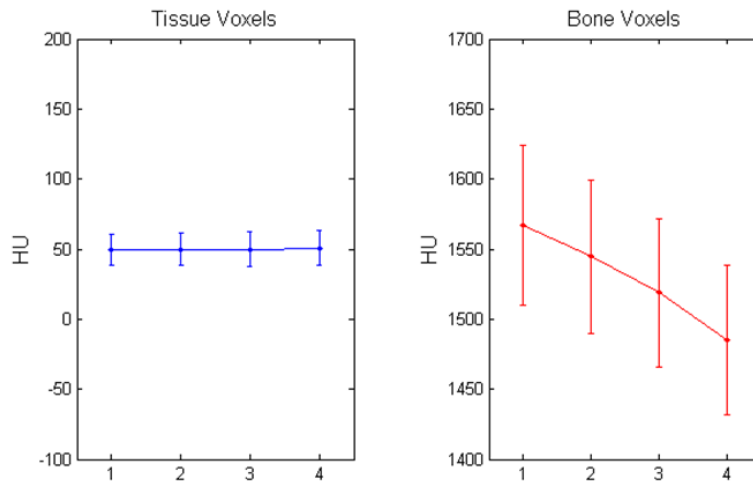
Figure 22. Measured HU values in the segmented "soft tissue" voxels and "bone" voxels of the knee phantom. Increasing attenuation did not affect the HU values measured in tissue voxels, but decreased the measured HU values in bone voxels.

4.3.2.2 Calibration of HU values of homogeneous bone voxels

Ideally, the value of HU_{bone} should be calibrated for each individual voxel. However, accurate correction for the beam hardening effect in a clinical CT dataset is extremely difficult. As an attempt to reduce the HU uncertainty from beam hardening, we developed a heuristic method as a "first-order" correction strategy. This is based on the observed linear relationship between the HU values of the homogenous bone voxels and the total in-slice attenuation (TISA, defined as the sum of the CT numbers from all voxels within a slice). In this strategy, HU_{bone} is adjusted for each individual slice when

91

estimating the BVF instead of being represented by a constant value. In other words, equation 4-3 becomes:

$$BVF(x,y,z) = \frac{HU(x,y,z) - 0HU}{HU_{bone}(z) - 0HU} \times 100\% = \frac{HU(x,y,z)}{HU_{bone}(z)} \times 100\% \qquad \text{Eq. 4-4}$$

Voxels within objects other than the patients (e.g., the scanner table and the positioning aids) were first excluded from the images. Then we computed HU_{bone} for each slice in each CT dataset of this study using the following steps:

a) Classification of slices

The CT slices were divided into skull slices and torso slices. The slice that contains the most inferior point of the chin was first identified as the landmark, and all slices above it were designated as skull slices (including the landmark slice), while slices below the landmark were recognized as torso slices.

b) Segmentation of homogeneous bone voxels

The potential candidates of homogeneous bone voxels were those that exceeded a threshold of 1000 HU. In order to exclude the voxels that are potentially mixed with soft tissue, a morphological erosion algorithm was used to erode the mask of potential candidates isotropically by one voxel. This step ensured that the identified bone voxels were at least one voxel away from any soft tissue voxels.

c) Mean HU value for bone voxels

The mean HU value for the segmented homogenous bone voxels in each slice was computed.

d) Calibration of $HU_{bone}(z)$ for torso slices

The total in-slice attenuation TISA was calculated for each torso slice. A linear regressional analysis was performed between TISA and the measured mean HU for bone voxels. $HU_{bone}(z)$ was then computed using the linear correlation coefficients and TISA for each torso slice.

e) Calibration of $HU_{bone}(z)$ for skull slices

The HU values for homogenous bone voxels in the skull slices were observed not to be linearly correlated with TISA. Therefore, a single $HU_{bone}(z)$ was used for all of the skull slices. It was simply calculated as the mean of all the bone voxels in the skull of each dataset.

After $HU_{bone}(z)$ had been determined, BVF was computed for each voxel using equation 4-4. The computed BVFs could have values less than 0 or greater than 1, which are not realistically possible values for BVF. In those cases, BVFs were reset to 0 or 1, respectively.
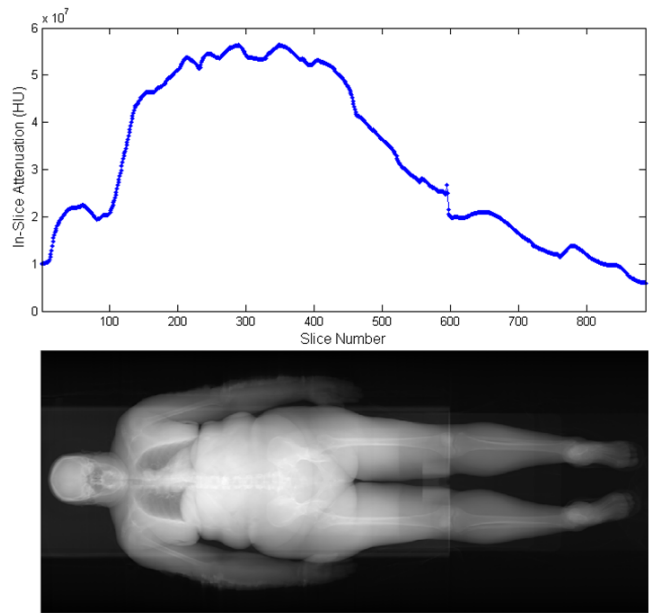
Figure 23. Variation of TISA among the CT slices of a female adult. TISA is calculated as the sum of the CT numbers (shifted by 1024) of all the voxels within the slice.
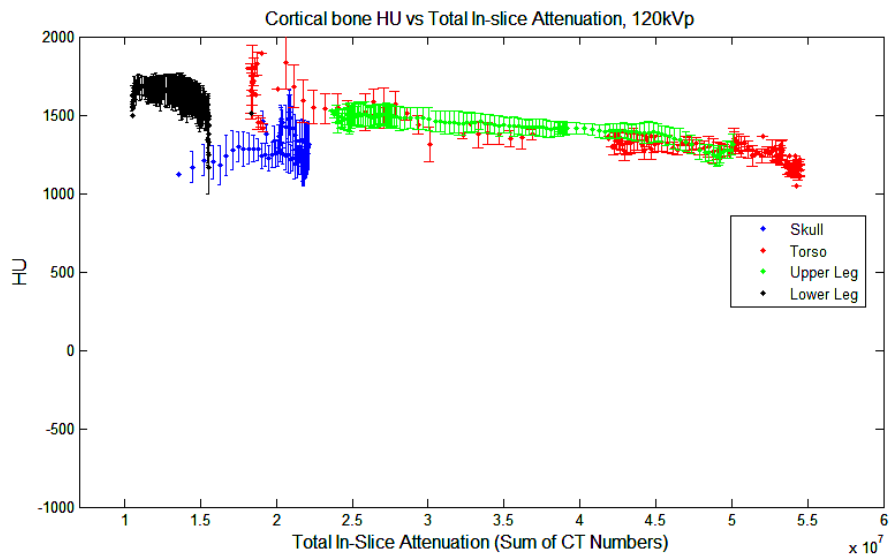
Figure 24. The HU of homogeneous bone voxels in one CT dataset vs. TISA. Each data point and error bar represents the voxels in one CT slice. It can be seen that the relationship between the mean HU of the homogenous bone voxels and TISA is approximately linear (except for the skull slices).

4.3.3   Simulation of MRAC Images with Various Bone Identification Sensitivities

For MR-based attenuation correction using tissue-classification-based approaches, identification of bone in voxels with higher BVF is easier because there are greater differences in the MR-derived parameters, such as R_2^*, between such voxels and voxels representing soft tissue. By the same token, identifying bone in voxels with lower BVF is more difficult. Therefore, the sensitivity of a bone identification method can be characterized with the lowest BVF that a voxel must have in order for the presence of bone to be detectable using this technique. A low BVF threshold indicates that the technique is sensitive to the presence of bone, while a high BVF threshold indicates relative insensitivity.

A BVF threshold of 100% corresponds to the situation with the lowest sensitivity, namely that in which the presence of bone can be identified only in voxels with BVFs strictly greater than 100%. Such threshold simulates the MRAC approaches that are available on the current commercial PET/MR systems in which bone is treated the same as soft tissue. With a decreasing BVF threshold, the simulated sensitivity increases. In theory, the highest sensitivity corresponds to the BVF threshold of 0%, meaning that the presence of bone can be identified even in voxels in which the volumetric fraction of bone approaches 0%. This could not be simulated in our study, because we found that a 10% BVF threshold roughly corresponds to 100~120 HU in the CT attenuation images. Further decreasing the threshold would start to include soft tissue voxels, leading to

unacceptable segmentation errors. This also indicates that, as the most sensitive tomographic bone imaging modality, the bone identification sensitivity of CT is slightly lower than 10% BVF. Expecting MR-based methods to achieve this level of sensitivity would be unrealistic with present technology.

In order to simulate the scenarios of different bone identification sensitivities in MR, ten sets of different attenuation images were created, representing a range of sensitivity with BVF thresholds of 100%, 90%, 80%, 70%, 60%, 50%, 40%, 30%, 20% and 10%. Voxels with a BVF higher than the thresholds were identified in each CT dataset, while voxels with a BVF between 10% and the threshold values were identified as soft tissue, simulating the consequence of limited sensitivity. For each BVF threshold, the mean HU values for the identifiable voxels were calculated for each dataset. These mean HU values were then assigned to the segmented bone voxels, replacing the original HU value. The mean HU values for soft tissue voxels were also calculated for each patient, and assigned to the voxels with a BVF between 10% and the corresponding threshold. The HU values for voxels with BVF<10%, representing the soft tissue voxels, were not modified. By doing this, the attenuation contribution of bone is isolated from that of the rest of the body. The components that were first excluded prior to the BVF estimation (e.g., the patient table and the positioning aids) were then reintroduced into the attenuation images so that they were consistent with the reference CT. The ten sets of attenuation images, along with the original CT attenuation images, were then used in the reconstruction of the PET data.

4.3.4 Identification and Classification of NaF-Avid Bone Lesions

In order to quantitatively assess the effect of bone identification sensitivity on PET bone lesion quantification, we evaluated the difference in tracer uptake of NaF-avid bone lesions (for convenience, all regions of bones with tracer uptake that was visibly higher than the surrounding background are referred to as lesions in this study, without necessarily implying any clinical indication). The lesions were visually identified on the PET images reconstructed with original CTAC images.

The definition of lesions was performed with our in-house Matlab software. A seed location was first chosen for each lesion, and then a region-growing algorithm was used to segment the PET voxels with an appropriate uptake threshold that was manually determined for each lesion. If necessary, this step was followed by morphological dilation or erosion to ensure an adequate segmentation of the entire tracer-avid region.
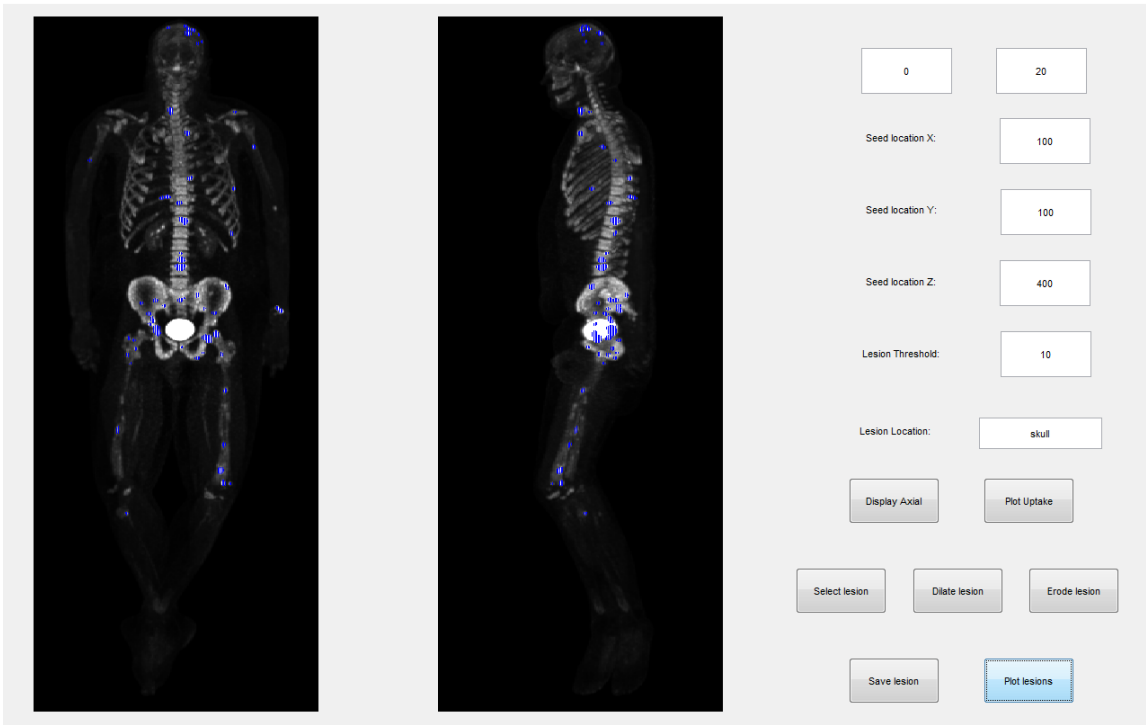
Figure 25. User interface of the in-house Matlab software developed to define lesions in this study.

Figure 26. An example of the misregistration between CT attenuation and the PET emission images in the lower extremities from voluntary patient motion during the exam. To avoid this problem, lesions in the extremities were not included in the quantitative analysis in this study.

In these NaF PET/CT studies, NaF-avid lesions could be identified in bones all over the body. However, sometimes patients move their limbs during the lengthy PET scan, causing spatial misregistration of limbs between the CT image and the PET image, which can lead to inaccuracy in quantification of the affected lesions. An example of misregistration is shown in Figure 26. For this reason, lesions that are located in the bones of the upper and lower extremities were not included in the analysis. A total of 139 suitable lesions were identified in five different locations: skull (N=21), pelvis (N=28), ribs (N=18), vertebral processes (N=18) and vertebral bodies (N=54). Maximum uptakes were quantified in the ROIs of these lesions.

4.4 Results

4.4.1 MRAC Image with Various Bone Identification Sensitivities

A CTAC image and the simulated attenuation images with no identified bone are shown in Figure 27. An example of attenuation images with various bone identification sensitivities are shown in Figure 28. The HU values assigned to the segmented AC images are given in Table 2.

Table 2. HU values assigned to the segmented bone voxels corresponding to each sensitivity level of bone identification, as determined by the mean HU of the voxels above the BVF threshold in each dataset. The CT images were acquired with 140 kVp except for one dataset, which was obtained with 120 kVp. That value is listed separately.

BVF threshold	HU Assigned to Segmented Bone Voxels
10%	461±30 HU, 501 HU
20%	620±34 HU, 642 HU
30%	764±42 HU, 787 HU
40%	885±45 HU, 914 HU
50%	984±44 HU, 1019 HU
60%	1067±44 HU, 1109 HU
70%	1147±52 HU, 1202 HU
80%	1219±54 HU, 1303 HU
90%	1287±51 HU, 1397 HU
Tissue	31±7 HU
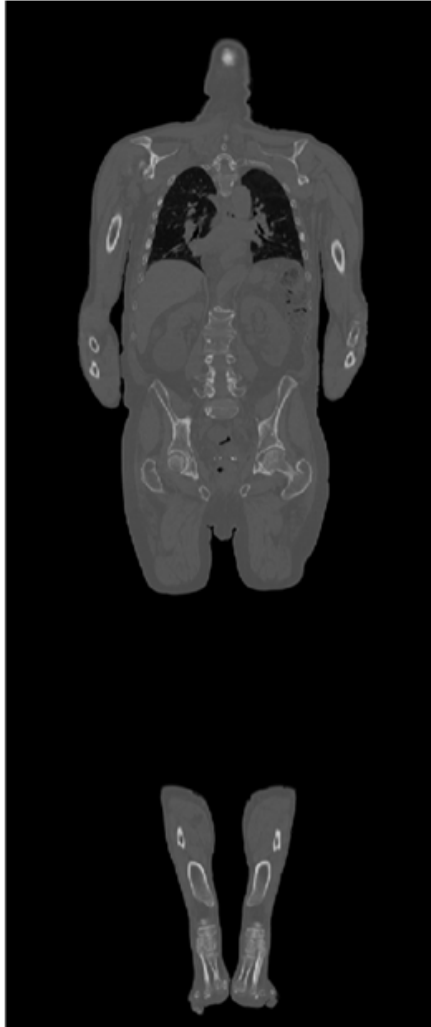
Original CT   AC map with no bone

Figure 27. Attenuation image with all voxels above 10% BVF assigned with the soft tissue attenuation coefficient.
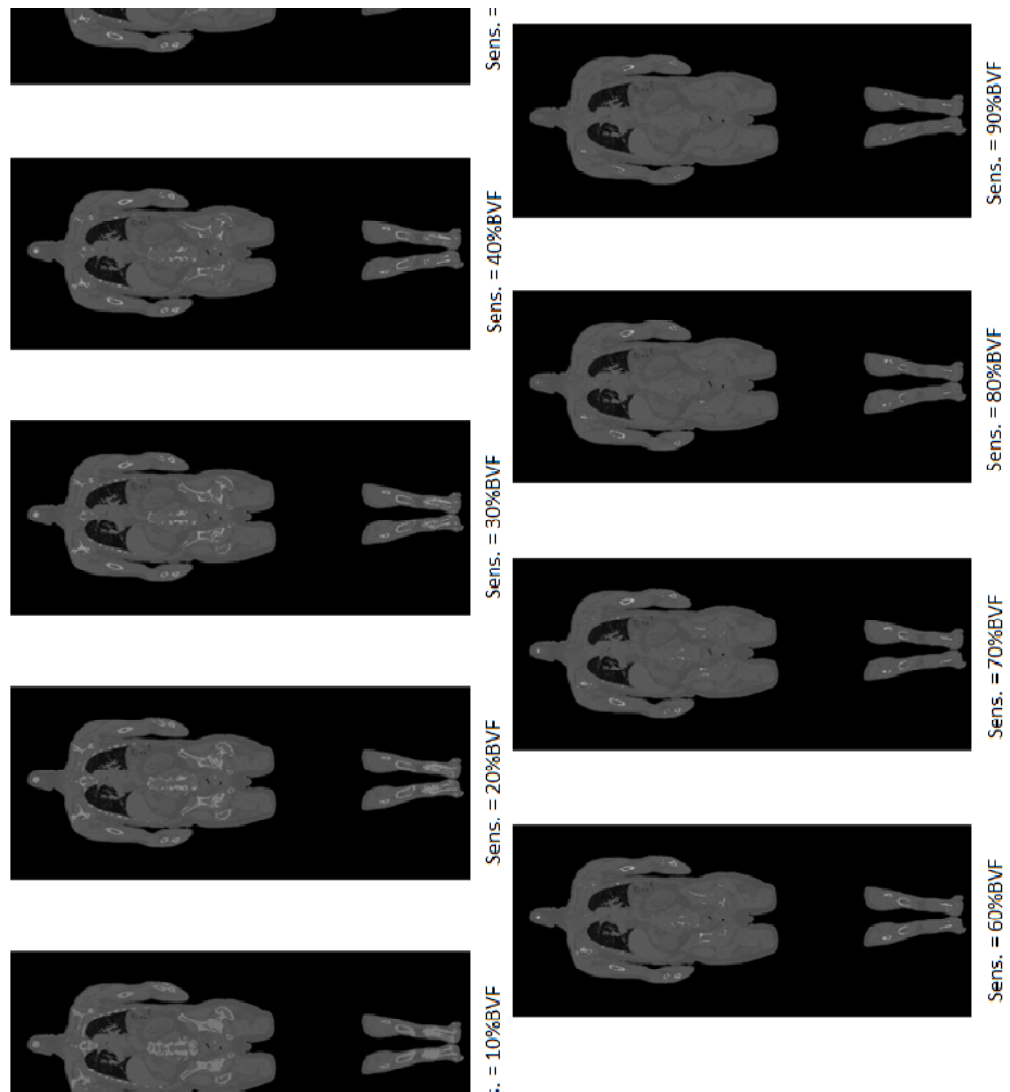
Figure 28. An example of simulated attenuation image with bone identification sensitivities varying from BVF = 10% to BVF = 90%

4.4.2 Quantification Difference in NaF-Avid Bone Lesions without and with a Highly Sensitive Bone Identification in Attenuation Images

Compared to the reference PET data, the quantification difference of the 139 tracer-avid bone lesions when no bone was identified in the attenuation images was -10.3%±5.6% (-2.0% to -27.6%) for the maximal uptake. The degree of underestimation differs between

lesions located inside the skull (-20.3%±4.1%) and lesions located in the body (-8.5%±3.6%, p<0.001[2]). Within the body, the underestimation of lesions in ribs (-4.5%±1.6%) is significantly lower compared to lesions in the pelvis, the vertebral bodies and the vertebral processes (-9.2%±3.3%, p<0.001). However, the difference between lesions in the pelvis, the vertebral bodies and the vertebral processes was not found to be statistically significant (p=0.424 for the pelvis and the vertebral processes, p=0.864 for the pelvis and the vertebral bodies, and p=0.137 for the vertebral processes and the vertebral bodies).

For the simulation of the case of a highly sensitive method for bone identification method in MR (corresponding to a BVF threshold of 10%), the quantification difference of the 139 bone lesions decreased from -10.3%±5.6% to 0.9%±4.8%. However, although the mean difference is small, there is compensation between the overestimated and the underestimated lesions. Analyzing the absolute values of the differences in order to remove the compensation effect, the absolute quantification difference of the 139 lesions decreased from 10.3%±5.6% to 3.9%±2.9%, which is a reduction of 62% of the original bias.

Table 3. Quantification difference in 139 bone lesions when bone is classified as soft tissue in the attenuation image.

Lesion location	Difference in max uptake
All (N=139)	-10.3%±5.6% (-27.6% ~ -2.0%)

---

[2] The statistical significances in this chapter were all evaluated using Wilcoxon rank sum test, unless stated otherwise.

Skull (N=21)	-20.3%±4.1% (-27.6% ~ -10.8%)
Non-Skull (N=118)	-8.5%±3.6% (-19.1% ~ -2.0%)
Pelvis (N=28)	-9.4%±4.4% (-19.1% ~ -2.6%)
Ribs (N=18)	-4.5%±1.6% (-7.9% ~ -2.0%)
Vertebral Body (54)	-8.9%±2.9% (-17.1% ~ -4.2%)
Vertebral Process (18)	-10.0%±2.7% (-15.9% ~ -5.9%)
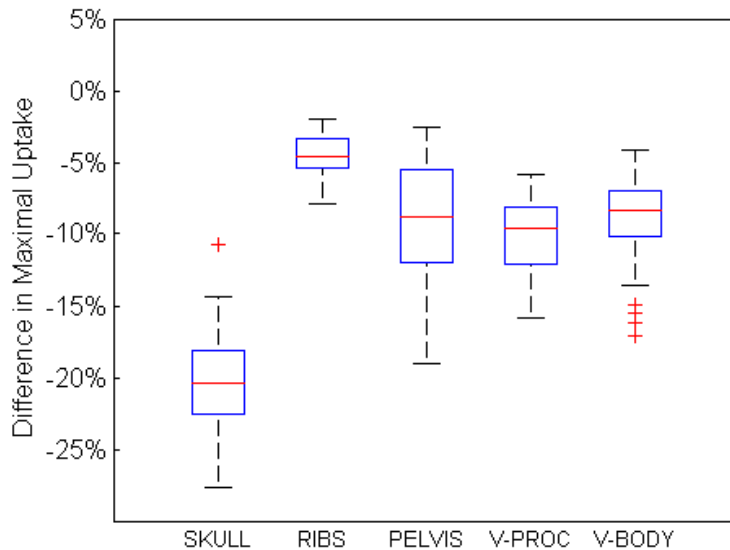
Figure 29. Quantification difference in 139 bone lesions when bone is classified as soft tissue in the attenuation image.

4.4.3   Effect of Bone Identification Sensitivity on Bone Lesion Quantification

The dependence of quantification difference in the 139 bone lesions on the sensitivity of bone identification is plotted in Figure 30. Interestingly, the overall absolute quantification error, which was 10.3%±5.6% with no bone identified, did not decrease

monotonically as the sensitivity of bone identification increased, but instead reached a minimum of 1.5%±1.3% with the simulated attenuation images corresponding to the sensitivity at 30% BVF threshold. This corresponds to a reduction of 85% of the original quantification bias. Beyond this point increasing the bone identification sensitivity slightly increased the quantification error.
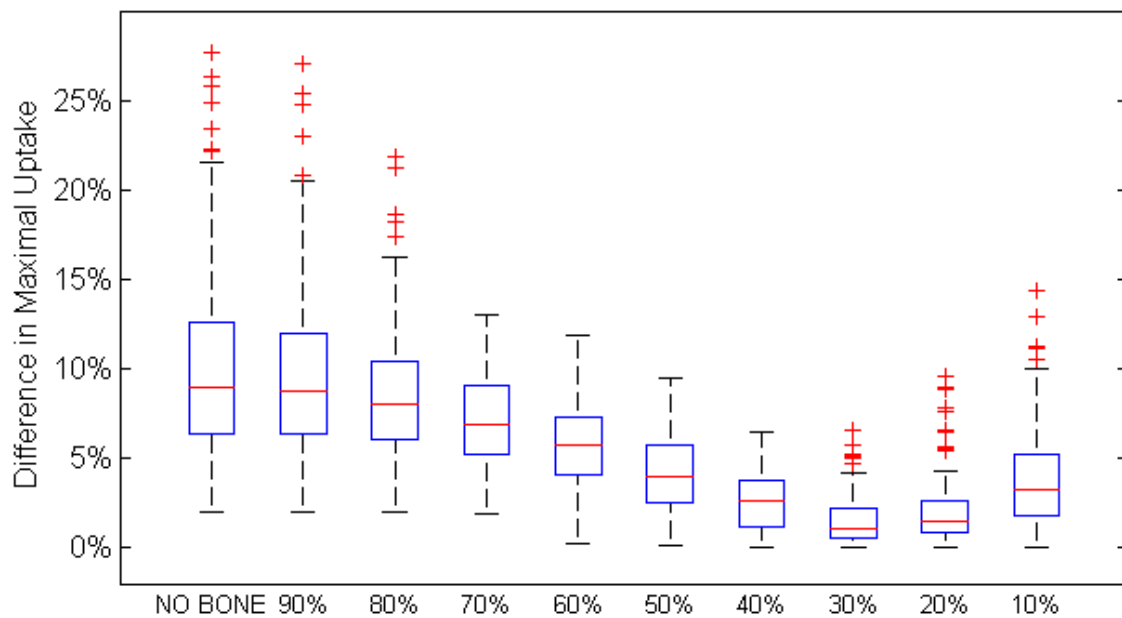
Figure 30. Absolute quantification difference in 139 bone lesions vs. bone identification sensitivity.

A closer examination of the lesions revealed that there is also a notable difference between the lesions in the skull and lesions in the body (i.e. pelvis, ribs, and vertebrae). As the bone identification sensitivity increased from no bone identification to approximately 30% BVF threshold, the degree of underestimation of bone lesions in the body decreased steadily from 8.5%±3.6% to 1.3%±1.1%. Overestimation then started to

occur and the absolute quantification difference reached 3.1%±2.0% at 10% BVF threshold. In contrast, underestimation of skull lesions decreased as bone identification sensitivity increased to 40% BVF threshold, from 20.3%±4.1% to 2.0%±1.6%, and then increased to 8.1%±3.4% without becoming overestimated.

Table 4. **Mean values of absolute quantification difference in evaluated lesions vs. BVF threshold used in binary segmentation of bone**

BVF	All	Skull	Body	Ribs	Pelvis	V-Proc	V-Body
No Bone	10.3%	20.3%	8.5%	4.5%	9.4%	10.0%	8.9%
90%	9.5%	17.2%	8.2%	4.4%	8.7%	9.5%	8.7%
80%	8.5%	13.8%	7.6%	4.4%	7.8%	8.8%	8.2%
70%	7.2%	9.2%	6.8%	4.2%	6.8%	7.8%	7.4%
60%	5.7%	5.2%	5.8%	3.7%	5.6%	6.3%	6.3%
50%	4.2%	2.7%	4.4%	2.8%	4.2%	4.4%	5.1%
40%	2.6%	2.0%	2.7%	1.9%	2.6%	2.4%	3.2%
30%	1.5%	2.8%	1.3%	0.8%	1.3%	0.9%	1.5%
20%	2.0%	5.1%	1.5%	1.2%	1.4%	1.6%	1.6%
10%	3.9%	8.1%	3.1%	2.4%	3.1%	2.6%	3.6%

Table 5. **Standard deviation of the absolute quantification difference in evaluated lesions vs. BVF threshold used in the binary segmentation of bone**

BVF	All	Skull	Body	Ribs	Pelvis	V-Proc	V-Body
No Bone	5.6%	4.1%	3.6%	1.6%	4.3%	2.7%	2.9%
90%	4.8%	5.4%	3.1%	1.5%	3.6%	2.3%	2.5%
80%	3.7%	4.4%	2.7%	1.5%	3.0%	2.4%	2.2%
70%	2.6%	2.9%	2.4%	1.3%	2.5%	2.2%	2.1%
60%	2.2%	2.3%	2.2%	1.1%	2.0%	1.9%	2.3%
50%	2.1%	1.8%	2.1%	1.0%	1.5%	2.1%	2.3%
40%	1.6%	1.6%	1.6%	0.9%	1.2%	1.9%	1.8%

30%	1.3%	2.0%	1.0%	0.6%	0.8%	0.7%	1.3%
20%	1.9%	2.6%	1.0%	0.5%	0.9%	1.0%	1.1%
10%	2.9%	3.4%	2.0%	1.1%	1.8%	1.8%	2.3%
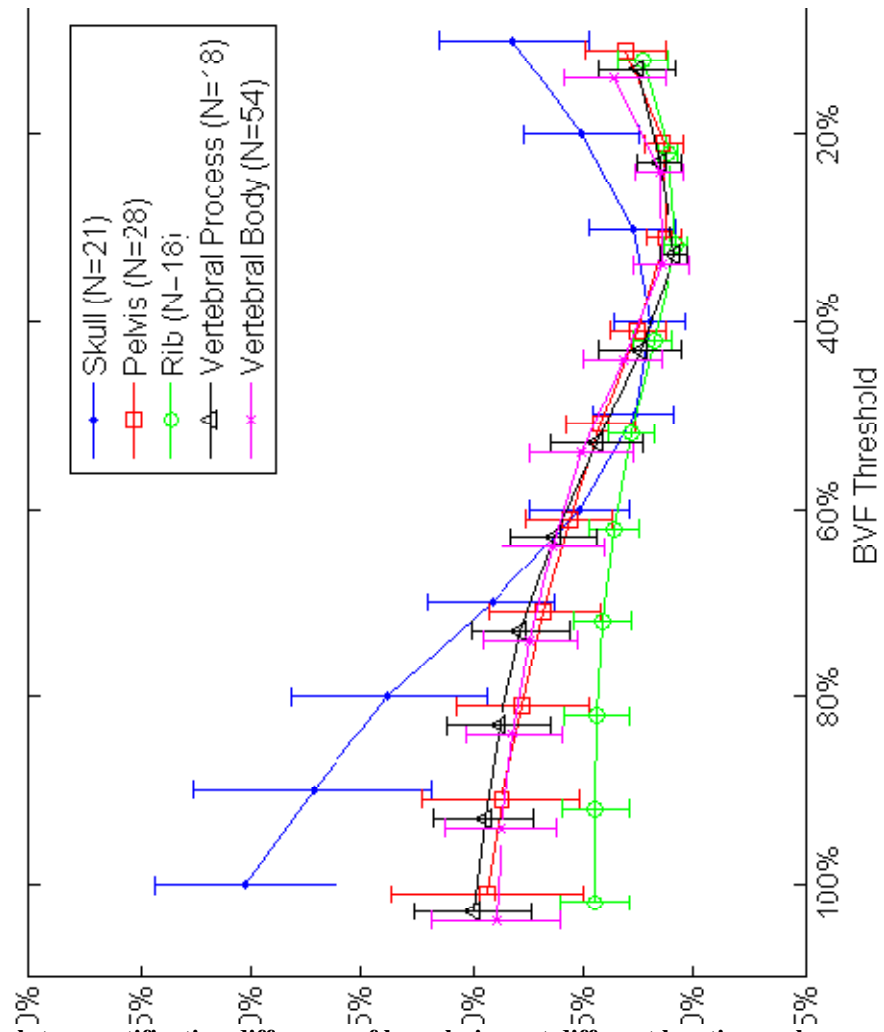
Figure 31. Absolute quantification difference of bone lesions at different location vs. bone identification sensitivity
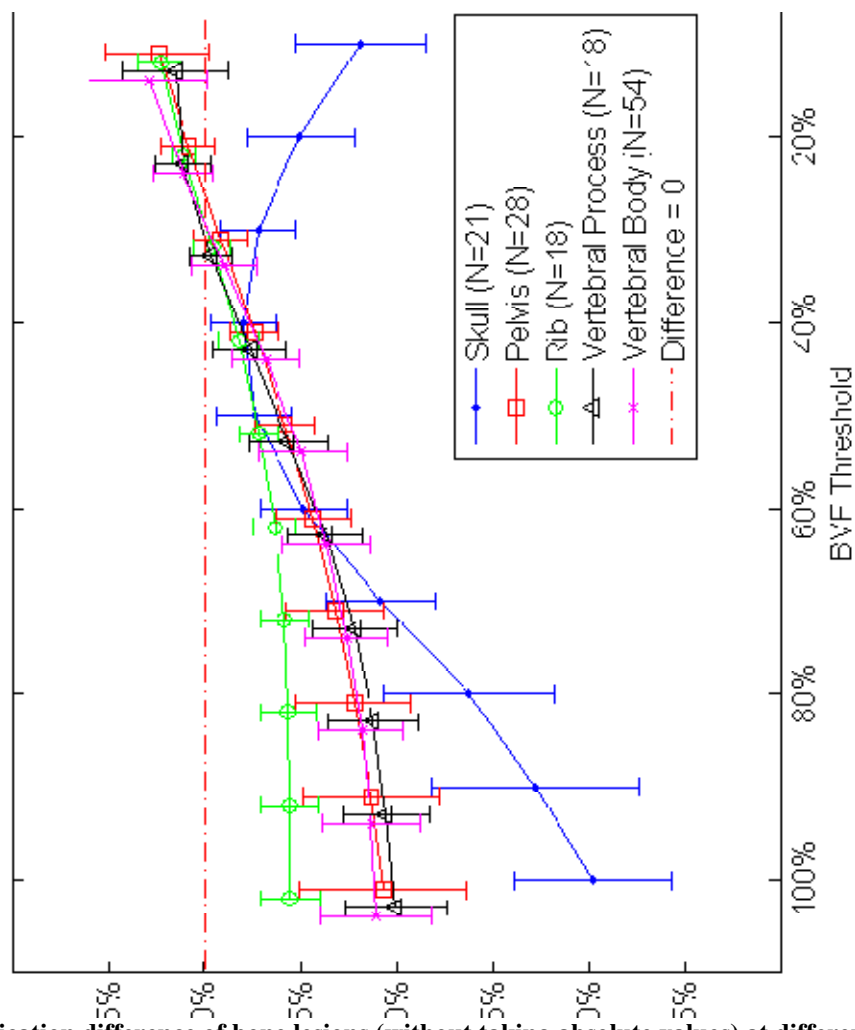
Figure 32. Quantification difference of bone lesions (without taking absolute values) at different location vs. bone identification sensitivity

4.5   Discussion

Since combined whole-body PET/MR systems became commercially available, MR-based attenuation correction techniques using binary tissue-classification have been studied by many previous investigators, most of whom concluded that identifying bone as a separate tissue class is necessary in order to achieve accurate quantification of the PET data, especially for regions inside of or near bones. Some of these studies have shown

that with a sensitive bone identification method, accurate PET quantification can be achieved. However, previous studies have not discussed the issues regarding intra-voxel averaging of bone and soft tissue or the required sensitivity for an MR binary-tissue-classification based attenuation correction approach to correct for the attenuation from human bones. In this study, we examined the contribution to attenuation from bone in greater detail and, for the first time, evaluated how the sensitivity of bone identification can affect the PET quantification in bone lesions. We have thereby established the requirement for the correction of bone-induced attenuation in PET/MR.

When bones are not separately identified in the attenuation images, uptakes in all bone lesions evaluated in this study were underestimated. The underestimation spanned a wide range, from as little as 2.0% to almost 30%. It is significantly higher in the skull than in the other parts of the skeleton that were evaluated in this study. This is expected because in the head, the bone-to-tissue ratio is appreciably higher than in the body. The underestimation of lesion uptakes in the ribs is significantly lower. However, this does not necessarily indicate that the identification of rib bones is less important, but more likely stems from the deleterious effects of involuntary respiratory motion, which caused spatial misregistration between the PET images and the CT images and partially projected uptake in the rib bones into soft tissues in the CT images.

The most interesting result of this study is the non-monotonic relationship between the bone identification sensitivity and the quantification difference in bone lesions. Intuitively, one would expect that the more sensitively bone can be identified, the

less quantification bias there would be in the PET data. Our results showed otherwise: when a binary-tissue-classification method is used for attenuation correction of bone in whole-body imaging, there appears to be an optimal BVF threshold for the segmentation of voxels that are partially bone, beyond which improving the sensitivity is not only unnecessary but in fact counterproductive. This result is not entirely surprising, though, given how binary-tissue-classification approaches are performed in MR-based PET attenuation correction: a single attenuation coefficient is assigned to represent an entire tissue class. This can be justified relatively easily for air, fat, and non-fat soft tissues, whose attenuation coefficients have been shown to have small inter-patient variation (partly because intra-voxel averaging is not a serious problem for these tissue classes). This, however, proved to be more problematic for the bone and lung class [104], both of which are affected by substantial intra-voxel averaging (air and soft tissue for the lung class, and bone and soft tissue for the bone class) within typical clinical voxel sizes. As the result of tissue mixing at various ratios, the nominal attenuation coefficients measured in CT for these two classes have significantly wider distributions compared to "air", "fat" and "soft tissue" even for the same patient. Consequently, using a single attenuation coefficient to represent the entire tissue class can be problematic, as it inevitably leads to overestimation in some regions and underestimation in other regions. In our study, this can be observed both in the split trend between skull and non-skull lesions, and the variation of lesion quantification within the same bone type.

However, this does not invalidate the binary-tissue-classification as a viable solution for PET bone attenuation correction. Our results in this simulated study have

shown that, using a binary bone segmentation method corresponding to approximately 30% BVF threshold and assigning 760 HU (approximately corresponding to 0.135 cm^{-1} for 511 keV photons [105]), the absolute quantification difference of bone lesions was reduced to 1.5%±1.3% compared to CT-corrected PET data. Although this is probably as accurate as a binary-classification method can be, an absolute quantification difference of less than 2.0% is sufficient for most clinical PET applications. More importantly, this study demonstrates that, in order to minimize the quantification effect of bone, MR-based methods do not have to be as sensitive as CT in bone identification. This is fortuitous, given the various limitations in the fundamental imaging mechanism of MR when it comes to bone.

It should be noted that this study has several limitations. One of the primary limitations is the inaccuracy in the estimation of BVF using HU values, which comes from two main sources. The first is the inaccuracy of the values of HU_{bone} and HU_{tissue} in the model. As explained in earlier paragraphs, ideally HU_{bone} needs to be compensated for on a voxel-by-voxel basis. However, this is not practical for clinical CT data. By using the heuristic method we developed that aims to correct the HU_{bone} variation associated with TISA (total in-slice attenuation), the uncertainty is reduced, but can still cause inaccuracy. The other source of BVF inaccuracy is from the CT image noise. Our preliminary analysis estimated that the final root-mean-square-error of voxel BVF estimation from all sources for the eight patients in this study is at minimum 6.0%, and can reach 10.3% with a more realistic estimation. Fortunately, the impact of BVF inaccuracy on the PET quantification was mitigated by the compensation between

overestimation and underestimation of BVF when the voxels that are partially bone were segmented to simulate the attenuation images.

Another limitation of this study is associated with voxel size, which largely determines the extent of intra-voxel averaging. In theory, when the voxel size is small enough compared to the dimension of human bone, voxel averaging can be reduced to a negligible level, and most bone will be located in homogenous bone voxels. Under this scenario, even a method with low bone identification sensitivity would be able to identify enough bone for an adequate attenuation correction. However, reducing voxel averaging by using small voxel sizes in clinical MR scans, especially the ones used for attenuation correction purposes, is impractical as it requires substantially longer acquisition times and also degrades the signal-to-noise ratio in the obtained image. The voxel size of the CT attenuation images used in this study is 1.5 mm ×1.5 mm ×3.0 mm, which is a typical voxel size in clinical MR imaging of the body. The optimal BVF threshold to correct for bone attenuation is expected to depend on the voxel size used for MR imaging, with larger voxel sizes being expected to require higher sensitivity. Since the voxel size for whole-body MR attenuation images is not likely to be significantly smaller, a BVF of 30~40% can be considered to be the bone identification sensitivity that binary-tissue-classification techniques should aim to achieve in order to obtain the best quantification in PET bone lesion uptakes. We estimate the sensitivities of previously published UTE MRAC studies to be around 50%~70% using the sequence parameters published in the articles and typical tissue MR properties. Sensitivities achieved in those studies can

largely compensate the bone attenuation in brain MR, but still need further improvement if optimized applications in whole-body PET/MR are to be achieved.

4.6   Conclusion

In this study we examined the dependence of quantification accuracy of PET lesions inside human bones on the bone identification sensitivity in the attenuation image. We showed that the omission of bone identification can lead to approximately a 10% underestimation inside bones, and that with a binary-tissue-classification approach, an optimal bone identification threshold exists (40% BVF for the skull and 30% BVF for non-skull skeleton) that can minimize the quantification difference compared to reference CT-corrected PET data. This study further proves the feasibility of tissue-classification-based attenuation correction approach for PET/MR imaging.

Chapter 5:   Conclusions

5.1   Summary of Findings

Chapter 2 describes the automatic registration algorithm that we developed to reduce the spatial misregistration between emission and attenuation images for cardiac PET/CT studies and thus to reduce attenuation artifacts and quantification errors. The algorithm uses a modified fuzzy c-means clustering method to extract relevant information in both PET and CT images, and then tracks down the optimal registration location by minimizing a similarity measure calculated as the gradient correlation of the two images. This method was developed in a training group that contains 55 clinical cardiac PET/CT datasets, and was tested on an independent testing group that contains 65 datasets. Both ACT (respiration-averaged CT) and HCT (helical CT) data were employed in this study. Using the results of manual registration as a reference, the registration algorithm significantly reduced the misalignment between PET and CT images for both ACT and HCT datasets to less than 4 mm on average. The objective measure that characterizes the amount of overlapped volume of myocardium in PET and lung in CT, which can be used to indicate the amount of attenuation artifact in the reconstructed PET images, suggested that the registration algorithm could be as effective as manual registration in mitigating attenuation artifacts in cardiac PET images. ACT was found to be more advantageous for providing attenuation images to cardiac PET than HCT. However, registration remains necessary.

Chapter 3 describes a novel MR acquisition protocol and post-processing technique to produce MR-derived attenuation images whose temporal resolution is matched to that of PET for cardiac PET/MR. The goal of this technique is to reduce the

attenuation artifact that could occur in simultaneous PET/MR imaging of the thorax. Based on a principle similar to that used in a previously developed method for PET/CT [18], this technique uses a 2D fast SPGR sequence to acquire cine MR images with a high temporal resolution of approximately 0.5 seconds per frame while the patient breathes freely. Twelve frames were acquired in a continuous manner at each slice in order to obtain the dynamic information of the moving anatomy for at least one respiratory cycle. The protocol was able to obtain MR images without visible artifacts even though the patient was breathing freely. The individual MR images were processed with a three-class tissue-classification method and assigned two sets of CT numbers, one set derived from the patient-specific CT images and the other set from a reference group, to convert MR images into attenuation maps. The attenuation images were averaged over all frames of the same slice to obtain a set of attenuation images that has motion blurring similar to what seen in PET images. These were then used for the reconstruction of the PET data. The difference between MR-corrected PET data and CT-corrected PET data was acceptable, and the summed stress score, a measure routinely used to evaluate myocardial function, had the same value, indicating that the differences might be clinically irrelevant.

Chapter 4 describes a CT-simulated study that assesses the effect of bone identification sensitivity on the quantification of PET in bones using data from eight NaF PET/CT studies. The study simulated the scenario of an MR binary-tissue-classification attenuation correction strategy with a range of sensitivities in identifying bone. This was achieved by first estimating the volumetric fraction of bone within a voxel using a linear

signal model, and then assigning appropriate bone HU values to voxels whose bone volume fraction was above a certain threshold, while assigning tissue HU values to voxels whose bone volume fraction was below the threshold. The simulated attenuation images were then used for the attenuation correction of PET data. The quantification difference was evaluated in 139 NaF-avid bone lesions. The study found that without any bone identification in the attenuation map, uptakes in the lesions were underestimated by approximately 20% on average in the skull and 9% on average in the body (pelvis, ribs, vertebral processes and vertebral bodies). The relationship between the quantification difference and sensitivity of bone identification is not monotonic; the difference first decreases and then increases as sensitivity increases. For the typical clinical voxel size simulated in this study, the quantification difference reaches a minimum at around 30% BVF for lesions in the body and around 40% for lesions in the skull. Because it is implied that MR-based attenuation correction methods do not have to be as sensitive as CT in order to achieve accurate quantification, this study further confirms the feasibility of using binary-tissue-classification approach for correcting photon attenuations by bones in the human body.

5.2   Evaluation of the Hypotheses

This work sought to improve the attenuation correction in the hybrid PET systems through the pursuit of three specific aims.

Specific Aim I was to develop an automatic registration algorithm to reduce the spatial misalignment between emission and attenuation images and evaluate the algorithm with cardiac PET/CT. The hypothesis of this aim was that an automatic registration algorithm based on FCM-assisted gradient correlation for cardiac PET/CT data can reduce misregistration between PET and CT to less than 5 mm (physical spatial resolution for typical clinical PET scanners) on average compared to manual registration regardless of the CT breathing protocol. In this study, the misregistration after automatic registration performed by the proposed algorithm was less than 4 mm for both ACT and HCT images in the independent data group that was not involved in the development of the algorithm. Therefore, the hypothesis was accepted.

Specific Aim II was to design an acquisition protocol and post-processing technique to reduce temporal mismatch in cardiac PET/MR. The hypothesis of this aim was that using respiration-averaged MR images for PET attenuation correction is feasible, and can reduce the amount of PET attenuation artifact compared to using MR images obtained under breath-hold. It was demonstrated in the study that respiration-averaged MR images could indeed be used for PET attenuation correction, validating the first part of the hypothesis. The second part of the hypothesis, unfortunately, could not be verified in this study due to the lack of sufficient clinical data. There are strong reasons to believe this method can reduce the attenuation artifacts in PET/MR imaging, given how a similar approach was shown to be an effective solution to a similar problem in PET/CT. This needs to be verified by future investigations.

Specific Aim III was to investigate the minimal bone identification sensitivity required for MR-based attenuation correction strategy using a binary tissue-classification approach in order to reduce PET quantification bias of bone lesions to be less than 5%. The hypothesis was that <u>using a binary-tissue-classification-based MR attenuation correction approach, a bone identification sensitivity of 50% bone volume fraction can reduce the PET bone lesion quantification difference caused by the presence of bone to be less than 5%.</u> The quantification difference was evaluated both over all bone sites and inside specific bones. It was found that a sensitivity of 50% BVF, which is the "sensible" lower threshold for binary classification, was able to reduce average quantification difference of bone lesions to be less than 5%. However, the quantification differences are also dependent on the location of lesions. The results suggest that for the quantification inside vertebrae, a sensitivity higher than 50% might be necessary.

5.3   Future Directions

This dissertation sought to address some of the problems that can compromise attenuation correction and quantification of PET data in the hybrid systems. It has opened doors for some new investigations, and there are also areas in this work that can be improved upon by future research.

The automatic registration algorithm developed in Chapter 2 has been shown to be effective in registering the emission images with the attenuation images, and the quantitative FMMV values have indicated that it can reduce the attenuation artifact and

improve quantification in the reconstructed myocardial perfusion map. Future work should incorporate a validation of the improvement in quantification of the PET data and compare the results to those of manual registration. An automatic registration algorithm also has the advantage of being more repeatable than manual registration. The inter-operator variability has been demonstrated in this work; however, the intra-operator variability, which is another source of inaccuracy for manual registration, was not evaluated. Demonstration of this can further shed light on the advantage of automatic registration.

The conversion of respiration-averaged MR images to PET attenuation images in this work was achieved via tissue-classification of individual frames of MR images that capture a single phase of the respiratory motion. This is not ideal because the complete information of motion blurring cannot be fully preserved by the segmentation-then-averaging step without loss. A method that directly converts respiration-averaged MR images to respiration-averaged pseudo-CT images is more desirable. One possible solution is to establish a dedicated atlas consisting of registered ACT-AMR image pairs. Another is to combine the fuzzy segmentation strategy with intensity inhomogeneity correction in MR. Work also needs to be done to show the effectiveness of this method to reduce the attenuation artifact in more clinical PET/MR studies.

The study that assesses the effect of bone identification sensitivity on the quantification of PET in bones could be improved in several ways. First, a more accurate signal model could be used to estimate the volumetric fraction of bone in each voxel,

including a better method to compensate the HU value inaccuracy as a result of beam hardening. Secondly, aiming to obtain the minimal quantification difference from tissue-classification methods in order to demonstrate its potential, this study used the attenuation coefficient derived individually from each patient dataset. It would be interesting to see how much difference would result from using a more standardized set of attenuation coefficients for segmented bone voxels. Our discovery of the CT HU inaccuracy in voxels at the higher end of the HU range is very interesting, and could lead to new investigations outside the field of PET, such as quantitative computed tomography and MR-based treatment planning in radiation therapy, both of which could benefit from improved quantification of bone attenuation. The difference in the patterns of beam hardening between the skull and the non-skull skeleton might be another interesting subject of investigation. The next logical step of this study would be to validate the findings that were simulated using CT images with actual MR-derived attenuation images, although this might not be possible in the near future as more technical development is required in order to extend the application of UTE MR from the realm of brain imaging to whole-body application.

References

1. Nutt, R., *The History of Positron Emission Tomography.* Molecular Imaging & Biology. **4**(1):11-26(2002).
2. Herholz, K. and W.D. Heiss, *Positron emission tomography in clinical neurology.* Molecular imaging and biology : MIB : the official publication of the Academy of Molecular Imaging. **6**(4):239-69(2004).
3. Schwaiger, M., S. Ziegler, and S.G. Nekolla, *PET/CT: challenge for nuclear cardiology.* Journal of nuclear medicine : official publication, Society of Nuclear Medicine. **46**(10):1664-78(2005).
4. Bhatnagar, A., R. Hustinx, and A. Alavi, *Nuclear imaging methods for non-invasive drug monitoring.* Advanced drug delivery reviews. **41**(1):41-54(2000).
5. Rigo, P., P. Paulus, B.J. Kaschten, R. Hustinx, T. Bury, G. Jerusalem, T. Benoit, and J. FoidartWillems, *Oncological applications of positron emission tomography with fluorine-18 fluorodeoxyglucose.* Eur. J. Nucl. Med. **23**(12):1641-1674(1996).
6. Kumar, R., M.R. Nadig, and A. Chauhan, *Positron emission tomography: clinical applications in oncology. Part 1.* Expert review of anticancer therapy. **5**(6):1079-94(2005).
7. Kumar, R. and A. Chauhan, *Positron emission tomography: clinical applications in oncology. Part 2.* Expert review of anticancer therapy. **6**(4):625-40(2006).
8. Cherry, S.R., J.A. Sorenson, and M.E. Phelps, *chapter 18 - Positron Emission Tomography*, in *Physics in Nuclear Medicine (Fourth Edition)*, S.R.C.A.S.E. Phelps, Editor. 2012, W.B. Saunders: Philadelphia. p. 307-343.
9. Reinartz, P., F.J. Wieres, W. Schneider, A. Schur, and U. Buell, *Side-by-side reading of PET and CT scans in oncology: which patients might profit from integrated PET/CT?* European journal of nuclear medicine and molecular imaging. **31**(11):1456-61(2004).
10. Kluetz, P.G., C.C. Meltzer, V.L. Villemagne, P.E. Kinahan, S. Chander, M.A. Martinelli, and D.W. Townsend, *Combined PET/CT Imaging in Oncology. Impact on Patient Management.* Clinical positron imaging : official journal of the Institute for Clinical P.E.T. **3**(6):223-230(2000).
11. Hany, T.F., H.C. Steinert, G.W. Goerres, A. Buck, and G.K. von Schulthess, *PET diagnostic accuracy: improvement with in-line PET-CT system: initial results.* Radiology. **225**(2):575-81(2002).
12. Bar-Shalom, R., N. Yefremov, L. Guralnik, D. Gaitini, A. Frenkel, A. Kuten, H. Altman, Z. Keidar, and O. Israel, *Clinical performance of PET/CT in evaluation of cancer: additional value for diagnostic imaging and patient management.* Journal of nuclear medicine : official publication, Society of Nuclear Medicine. **44**(8):1200-9(2003).
13. Kinahan, P.E., D.W. Townsend, T. Beyer, and D. Sashin, *Attenuation correction for a combined 3D PET/CT scanner.* Medical physics. **25**(10):2046-2053(1998).
14. Burger, C., G. Goerres, S. Schoenes, A. Buck, A.H. Lonn, and G.K. Von Schulthess, *PET attenuation coefficients from CT images: experimental evaluation of the transformation of CT into PET 511-keV attenuation coefficients.* European journal of nuclear medicine and molecular imaging. **29**(7):922-7(2002).
15. Huang, B., M.W. Law, and P.L. Khong, *Whole-body PET/CT scanning: estimation of radiation dose and cancer risk.* Radiology. **251**(1):166-74(2009).

16. Lagerwaard, F.J., J.R. Van Sornsen de Koste, M.R. Nijssen-Visser, R.H. Schuchhard-Schipper, S.S. Oei, A. Munne, and S. Senan, *Multiple "slow" CT scans for incorporating lung tumor mobility in radiotherapy planning.* International journal of radiation oncology, biology, physics. **51**(4):932-7(2001).

17. Pan, T., T.Y. Lee, E. Rietzel, and G.T. Chen, *4D-CT imaging of a volume influenced by respiratory motion on multi-slice CT.* Medical physics. **31**(2):333-40(2004).

18. Pan, T., O. Mawlawi, D. Luo, H.H. Liu, P.C. Chi, M.V. Mar, G. Gladish, M. Truong, J. Erasmus, Jr., Z. Liao, and H.A. Macapinlac, *Attenuation correction of PET cardiac data with low-dose average CT in PET/CT.* Medical physics. **33**(10):3931-8(2006).

19. Alessio, A.M., S. Kohlmyer, K. Branch, G. Chen, J. Caldwell, and P. Kinahan, *Cine CT for attenuation correction in cardiac PET/CT.* Journal of nuclear medicine : official publication, Society of Nuclear Medicine. **48**(5):794-801(2007).

20. Cook, R.A., G. Carnes, T.Y. Lee, and R.G. Wells, *Respiration-averaged CT for attenuation correction in canine cardiac PET/CT.* Journal of nuclear medicine : official publication, Society of Nuclear Medicine. **48**(5):811-8(2007).

21. Furst, S., R. Grimm, I. Hong, M. Souvatzoglou, M.E. Casey, M. Schwaiger, S.G. Nekolla, and S.I. Ziegler, *Motion correction strategies for integrated PET/MR.* Journal of nuclear medicine : official publication, Society of Nuclear Medicine. **56**(2):261-9(2015).

22. Shao, Y., S.R. Cherry, K. Farahani, K. Meadors, S. Siegel, R.W. Silverman, and P.K. Marsden, *Simultaneous PET and MR imaging.* Physics in medicine and biology. **42**(10):1965-70(1997).

23. Schlemmer, H.P.W., B.J. Pichler, M. Schmand, Z. Burbar, C. Michel, R. Ladebeck, K. Jattke, D. Townsend, C. Nahmias, P.K. Jacob, W.D. Heiss, and C.D. Claussen, *Simultaneous MR/PET imaging of the human brain: Feasibility study.* Radiology. **248**(3):1028-1035(2008).

24. Zaidi, H., N. Ojha, M. Morich, J. Griesmer, Z. Hu, P. Maniawski, O. Ratib, D. Izquierdo-Garcia, Z.A. Fayad, and L. Shao, *Design and performance evaluation of a whole-body Ingenuity TF PET-MRI system.* Physics in medicine and biology. **56**(10):3091-106(2011).

25. Veit-Haibach, P., F.P. Kuhn, F. Wiesinger, G. Delso, and G. von Schulthess, *PET-MR imaging using a tri-modality PET/CT-MR system with a dedicated shuttle in clinical routine.* Magma (New York, N.Y.). **26**(1):25-35(2013).

26. Delso, G., S. Furst, B. Jakoby, R. Ladebeck, C. Ganter, S.G. Nekolla, M. Schwaiger, and S.I. Ziegler, *Performance measurements of the Siemens mMR integrated whole-body PET/MR scanner.* Journal of nuclear medicine : official publication, Society of Nuclear Medicine. **52**(12):1914-22(2011).

27. Bailey, D.L., G. Antoch, P. Bartenstein, H. Barthel, A.J. Beer, S. Bisdas, D.A. Bluemke, R. Boellaard, C.D. Claussen, C. Franzius, M. Hacker, H. Hricak, C. la Fougere, B. Guckel, S.G. Nekolla, B.J. Pichler, S. Purz, H.H. Quick, O. Sabri, B. Sattler, J. Schafer, H. Schmidt, J. van den Hoff, S. Voss, W. Weber, H.F. Wehrl, and T. Beyer, *Combined PET/MR: The Real Work Has Just Started. Summary Report of the Third International Workshop on PET/MR Imaging; February 17-21, 2014, Tubingen, Germany.* Molecular imaging and biology : MIB : the official publication of the Academy of Molecular Imaging,(2015).

28. Bin, Z., D. Pal, H. Zhiqiang, N. Ojha, T. Guo, G. Muswick, T. Chi-Hua, and J. Kaste. *Attenuation correction for MR table and coils for a sequential PET/MR system.* in *Nuclear Science Symposium Conference Record (NSS/MIC), 2009 IEEE.* 2009.

29. Delso, G., A. Martinez-Moller, R.A. Bundschuh, R. Ladebeck, Y. Candidus, D. Faul, and S.I. Ziegler, *Evaluation of the attenuation properties of MR equipment for its use in a whole-body PET/MR scanner.* Physics in medicine and biology. **55**(15):4361-74(2010).

30. Schramm, G., J. Langner, F. Hofheinz, J. Petr, A. Lougovski, B. Beuthien-Baumann, I. Platzek, and J. van den Hoff, *Influence and compensation of truncation artifacts in MR-based attenuation correction in PET/MR.* IEEE transactions on medical imaging. **32**(11):2056-63(2013).

31. Burger, I.A., M.C. Wurnig, A.S. Becker, D. Kenkel, G. Delso, P. Veit-Haibach, and A. Boss, *Hybrid PET/MR imaging: an algorithm to reduce metal artifacts from dental implants in Dixon-based attenuation map generation using a multiacquisition variable-resonance image combination sequence.* Journal of nuclear medicine : official publication, Society of Nuclear Medicine. **56**(1):93-7(2015).

32. Schreibmann, E., J.A. Nye, D.M. Schuster, D.R. Martin, J. Votaw, and T. Fox, *MR-based attenuation correction for hybrid PET-MR brain imaging systems using deformable image registration.* Medical physics. **37**(5):2101-9(2010).

33. Hofmann, M., F. Steinke, V. Scheel, G. Charpiat, J. Farquhar, P. Aschoff, M. Brady, B. Scholkopf, and B.J. Pichler, *MRI-Based Attenuation Correction for PET/MRI: A Novel Approach Combining Pattern Recognition and Atlas Registration.* J. Nucl. Med. **49**(11):1875-1883(2008).

34. Hofmann, M., I. Bezrukov, F. Mantlik, P. Aschoff, F. Steinke, T. Beyer, B.J. Pichler, and B. Scholkopf, *MRI-based attenuation correction for whole-body PET/MRI: quantitative evaluation of segmentation- and atlas-based methods.* Journal of nuclear medicine : official publication, Society of Nuclear Medicine. **52**(9):1392-9(2011).

35. Hu, Z., N. Ojha, S. Renisch, V. Schulz, I. Torres, A. Buhl, D. Pal, G. Muswick, J. Penatzer, T. Guo, P. Bonert, C. Tung, J. Kaste, M. Morich, T. Havens, P. Maniawski, W. Schafer, R.W. Gunther, G.A. Krombach, and L. Shao. *MR-based attenuation correction for a whole-body sequential PET/MR system.* in *Nuclear Science Symposium Conference Record (NSS/MIC), 2009 IEEE.* 2009.

36. Martinez-Moller, A., M. Souvatzoglou, G. Delso, R.A. Bundschuh, C. Chefd'hotel, S.I. Ziegler, N. Navab, M. Schwaiger, and S.G. Nekolla, *Tissue classification as a potential approach for attenuation correction in whole-body PET/MRI: evaluation with PET/CT data.* Journal of nuclear medicine : official publication, Society of Nuclear Medicine. **50**(4):520-6(2009).

37. Berker, Y., J. Franke, A. Salomon, M. Palmowski, H.C. Donker, Y. Temur, F.M. Mottaghy, C. Kuhl, D. Izquierdo-Garcia, Z.A. Fayad, F. Kiessling, and V. Schulz, *MRI-based attenuation correction for hybrid PET/MRI systems: a 4-class tissue segmentation technique using a combined ultrashort-echo-time/Dixon MRI sequence.* Journal of nuclear medicine : official publication, Society of Nuclear Medicine. **53**(5):796-804(2012).

38. Keereman, V., Y. Fierens, T. Broux, Y. De Deene, M. Lonneux, and S. Vandenberghe, *MRI-based attenuation correction for PET/MRI using ultrashort echo time sequences.* Journal of nuclear medicine : official publication, Society of Nuclear Medicine. **51**(5):812-8(2010).

39. Wiesinger, F., L.I. Sacolick, A. Menini, S.S. Kaushik, S. Ahn, P. Veit-Haibach, G. Delso, and D.D. Shanbhag, *Zero TE MR bone imaging in the head.* Magnetic resonance in medicine : official journal of the Society of Magnetic Resonance in Medicine / Society of Magnetic Resonance in Medicine,(2015).

40. Le Guludec, D., R. Lautamaki, J. Knuuti, J.J. Bax, F.M. Bengel, and C. European Council Nucl, *Present and future of clinical cardiovascular PET imaging in Europe - a position statement by the European Council of Nuclear Cardiology (ECNC).* Eur. J. Nucl. Med. Mol. Imaging. **35**(9):1709-1724(2008).

41. Gould, K.L., *Positron emission tomography in coronary artery disease.* Curr. Opin. Cardiol. **22**(5):422-428(2007).

42. Gould, K.L., T. Pan, C. Loghin, N.P. Johnson, A. Guha, and S. Sdringola, *Frequent diagnostic errors in cardiac PET/CT due to misregistration of CT attenuation and emission PET images: A definitive analysis of causes, consequences, and corrections.* J. Nucl. Med. **48**(7):1112-1121(2007).

43. Loghin, C., S. Sdringola, and K.L. Gould, *Common artifacts in PET myocardial perfusion images due to attenuation-emission misregistration: clinical significance, causes, and solutions.* J Nucl Med. **45**(6):1029-39(2004).

44. Martinez-Moller, A., M. Souvatzoglou, N. Navab, M. Schwaiger, and S.G. Nekolla, *Artifacts from misaligned CT in cardiac perfusion PET/CT studies: frequency, effects, and potential solutions.* Journal of nuclear medicine : official publication, Society of Nuclear Medicine. **48**(2):188-93(2007).

45. Nye, J.A., F. Esteves, and J.R. Votaw, *Minimizing artifacts resulting from respiratory and cardiac motion by optimization of the transmission scan in cardiac PET/CT.* Med Phys. **34**(6):1901-6(2007).

46. Lautamaeki, R., T.L.Y. Brown, J. Merrill, and F.M. Bengel, *CT-based attenuation correction in Rb-82-myocardial perfusion PET-CT: incidence of misalignment and effect on regional tracer distribution.* Eur. J. Nucl. Med. Mol. Imaging. **35**(2):305-310(2008).

47. Pan, T.S., C. Mawlawi, S.A. Nehmeh, Y.E. Erdi, D.S. Luo, H.H. Liu, R. Castillo, R. Mohan, Z.X. Liao, and H.A. Macapinlac, *Attenuation correction of PET images with respiration-averaged CT images in PET/CT.* J. Nucl. Med. **46**(9):1481-1487(2005).

48. Gilman, M.D., A.J. Fischman, V. Krishnasetty, E.F. Halpern, and S.L. Aquino, *Hybrid PET/CT of the thorax: When is computer registration necessary?* Journal of Computer Assisted Tomography. **31**(3):395-401(2007).

49. Nakamoto, Y., M. Osman, C. Cohade, L.T. Marshall, J.M. Links, S. Kohlmyer, and R.L. Wahl, *PET/CT: comparison of quantitative tracer uptake between germanium and CT transmission attenuation-corrected images.* Journal of nuclear medicine : official publication, Society of Nuclear Medicine. **43**(9):1137-43(2002).

50. Goerres, G.W., C. Burger, E. Kamel, B. Seifert, A.H. Kaim, A. Buck, T.C. Buehler, and G.K. Von Schulthess, *Respiration-induced attenuation artifact at PET/CT: technical considerations.* Radiology. **226**(3):906-10(2003).

51. Pan, T., O. Mawlawi, S.A. Nehmeh, Y.E. Erdi, D. Luo, H.H. Liu, R. Castillo, R. Mohan, Z. Liao, and H.A. Macapinlac, *Attenuation correction of PET images with respiration-averaged CT images in PET/CT.* J Nucl Med. **46**(9):1481-7(2005).

52. Gould, K.L., T. Pan, C. Loghin, N.P. Johnson, A. Guha, and S. Sdringola, *Frequent diagnostic errors in cardiac PET/CT due to misregistration of CT attenuation and emission PET images: a definitive analysis of causes, consequences, and corrections.* Journal of nuclear medicine : official publication, Society of Nuclear Medicine. **48**(7):1112-21(2007).

53. Alessio, A.M., P.E. Kinahan, K.M. Champley, and J.H. Caldwell, *Attenuation-emission alignment in cardiac PET/CT based on consistency conditions.* Med Phys. **37**(3):1191-200(2010).

54. Khurshid, K., R.J. McGough, and K. Berger, *Automated cardiac motion compensation in PET/CT for accurate reconstruction of PET myocardial perfusion images.* Phys Med Biol. **53**(20):5705-18(2008).

55. Bond, S., T. Kadir, J. Hamill, M. Casey, G. Platsch, D. Burckhardt, R. Eisner, N. Kaustubh, J. Declerck, and Ieee, *Automatic Registration of Cardiac PET/CT for Attenuation Correction*, in *2008 Ieee Nuclear Science Symposium and Medical Imaging Conference*. 2009, Ieee: New York. p. 4785-4790.

56. Marinelli, M., V. Positano, F. Tucci, D. Neglia, and L. Landini, *Automatic PET-CT Image Registration Method Based on Mutual Information and Genetic Algorithms.* Sci. World J.,(2012).

57. Zaidi, H., R. Nkoulou, S. Bond, A. Baskin, T. Schindler, O. Ratib, and J. Declerck, *Computed tomography calcium score scan for attenuation correction of N-13 ammonia cardiac positron emission tomography: effect of respiratory phase and registration method.* The international journal of cardiovascular imaging,(2013).

58. Szilagyi, L., Z. Benyo, S.M. Szilagyi, H.S. Adam, and Ieee, *MR brain image segmentation using an enhanced fuzzy C-means algorithm*, in *Proceedings of the 25th Annual International Conference of the Ieee Engineering in Medicine and Biology Society, Vols 1-4: A New Beginning for Human Health*. 2003, Ieee: New York. p. 724-726.

59. Bezdek, J.C., R. Ehrlich, and W. Full, *FCM - THE FUZZY C-MEANS CLUSTERING-ALGORITHM.* Computers & Geosciences. **10**(2-3):191-203(1984).

60. Ai, H. and T. Pan, *SU-E-I-86: Evaluation of Segmentation Based Attenuation Correction Methods for PET/MR in the Thorax.* Medical physics. **40**(6):145-145(2013).

61. Torigian, D.A., H. Zaidi, T.C. Kwee, B. Saboury, J.K. Udupa, Z.H. Cho, and A. Alavi, *PET/MR imaging: technical aspects and potential clinical applications.* Radiology. **267**(1):26-44(2013).

62. Herzog, H. and J. Van Den Hoff, *Combined PET/MR systems: an overview and comparison of currently available options.* The quarterly journal of nuclear medicine and molecular imaging : official publication of the Italian Association of Nuclear Medicine (AIMN) [and] the International Association of Radiopharmacology (IAR), [and] Section of the So. **56**(3):247-67(2012).

63. Buchbender, C., T.A. Heusner, T.C. Lauenstein, A. Bockisch, and G. Antoch, *Oncologic PET/MRI, part 1: tumors of the brain, head and neck, chest, abdomen, and pelvis.* Journal of nuclear medicine : official publication, Society of Nuclear Medicine. **53**(6):928-38(2012).

64. Buchbender, C., T.A. Heusner, T.C. Lauenstein, A. Bockisch, and G. Antoch, *Oncologic PET/MRI, part 2: bone tumors, soft-tissue tumors, melanoma, and lymphoma.* Journal of nuclear medicine : official publication, Society of Nuclear Medicine. **53**(8):1244-52(2012).

65. Catana, C., A. Drzezga, W.D. Heiss, and B.R. Rosen, *PET/MRI for neurologic applications.* Journal of nuclear medicine : official publication, Society of Nuclear Medicine. **53**(12):1916-25(2012).

66. Rischpler, C., S.G. Nekolla, I. Dregely, and M. Schwaiger, *Hybrid PET/MR Imaging of the Heart: Potential, Initial Experiences, and Future Prospects.* J Nucl Med. **54**(3):402-15(2013).

67. Nensa, F., T.D. Poeppel, K. Beiderwellen, J. Schelhorn, A.A. Mahabadi, R. Erbel, P. Heusch, K. Nassenstein, A. Bockisch, M. Forsting, and T. Schlosser, *Hybrid PET/MR Imaging of the Heart: Feasibility and Initial Results.* Radiology,(2013).

68. Schlosser, T., F. Nensa, A.A. Mahabadi, and T.D. Poeppel, *Hybrid MRI/PET of the heart: a new complementary imaging technique for simultaneous acquisition of MRI and PET data.* Heart (British Cardiac Society). **99**(5):351-2(2013).

69. Ratib, O. and R. Nkoulou, *Potential Applications of PET/MR Imaging in Cardiology.* Journal of nuclear medicine : official publication, Society of Nuclear Medicine,(2014).

70. Nappi, C. and G. El Fakhri, *State of the Art in Cardiac Hybrid Technology: PET/MR.* Current cardiovascular imaging reports. **6**(4):338-345(2013).

71. Pan, T.S., O. Mawlawi, D. Luo, H.H. Liu, P.C.M. Chi, M.V. Mar, G. Gladish, M. Truong, J. Erasmus, Z.X. Liao, and H.A. Macapinlac, *Attenuation correction of PET cardiac data with low-dose average CT in PET/CT.* Med. Phys. **33**(10):3931-3938(2006).

72. Keller, S.H., S. Holm, A.E. Hansen, B. Sattler, F. Andersen, T.L. Klausen, L. Hojgaard, A. Kjaer, and T. Beyer, *Image artifacts from MR-based attenuation correction in clinical, whole-body PET/MRI.* Magma (New York, N.Y.). **26**(1):173-81(2013).

73. Hofmann, M., F. Steinke, V. Scheel, G. Charpiat, J. Farquhar, P. Aschoff, M. Brady, B. Scholkopf, and B.J. Pichler, *MRI-based attenuation correction for PET/MRI: a novel approach combining pattern recognition and atlas registration.* J Nucl Med. **49**(11):1875-83(2008).

74. Hu, Z., N. Ojha, S. Renisch, V. Schulz, I. Torres, A. Buhl, D. Pal, G. Muswick, J. Penatzer, T. Guo, P. Boenert, C. Tung, J. Kaste, M. Morich, T. Havens, P. Maniawski, W. Schaefer, R.W. Guenther, G.A. Krombach, and L. Shao, *MR-based Attenuation Correction for a Whole-body Sequential PET/MR System*, in *2009 Ieee Nuclear Science Symposium Conference Record, Vols 1-5*, B. Yu, Editor. 2009. p. 3508-3512.

75. Steinberg, J., G. Jia, S. Sammet, J. Zhang, N. Hall, and M.V. Knopp, *Three-region MRI-based whole-body attenuation correction for automated PET reconstruction.* Nuclear medicine and biology. **37**(2):227-35(2010).

76. Schulz, V., I. Torres-Espallardo, S. Renisch, Z. Hu, N. Ojha, P. Bornert, M. Perkuhn, T. Niendorf, W.M. Schafer, H. Brockmann, T. Krohn, A. Buhl, R.W. Gunther, F.M. Mottaghy, and G.A. Krombach, *Automatic, three-segment, MR-based attenuation correction for whole-body PET/MR data.* European journal of nuclear medicine and molecular imaging. **38**(1):138-52(2011).

77. Perona, P. and J. Malik, *Scale-space and edge detection using anisotropic diffusion.* Pattern Analysis and Machine Intelligence, IEEE Transactions on. **12**(7):629-639(1990).

78. Gonzalez, R.C., R.E. Woods, and S.L. Eddins, *Digital Image Processing Using MATLAB*. 2003: Prentice-Hall, Inc.

79. Berman, D.S., R. Hachamovitch, H. Kiat, I. Cohen, J.A. Cabico, F.P. Wang, J.D. Friedman, G. Germano, K. Van Train, and G.A. Diamond, *Incremental value of prognostic testing in patients with known or suspected ischemic heart disease: a basis for optimal utilization of exercise technetium-99m sestamibi myocardial perfusion single-photon emission computed tomography.* Journal of the American College of Cardiology. **26**(3):639-47(1995).

80. Cerqueira, M.D., N.J. Weissman, V. Dilsizian, A.K. Jacobs, S. Kaul, W.K. Laskey, D.J. Pennell, J.A. Rumberger, T. Ryan, M.S. Verani, S. American Heart Association Writing Group on Myocardial, and I. Registration for Cardiac, *Standardized myocardial segmentation and nomenclature for tomographic imaging of the heart. A statement for healthcare professionals from the Cardiac Imaging Committee of the Council on Clinical Cardiology of the American Heart Association.* Circulation. **105**(4):539-42(2002).

81. Andersen, F.L., C.N. Ladefoged, T. Beyer, S.H. Keller, A.E. Hansen, L. Hojgaard, A. Kjaer, I. Law, and S. Holm, *Combined PET/MR imaging in neurology: MR-based*

attenuation correction implies a strong spatial bias when ignoring bone. NeuroImage. **84C**:206-216(2013).

82. Keereman, V., R.V. Holen, P. Mollet, and S. Vandenberghe, *The effect of errors in segmented attenuation maps on PET quantification.* Medical physics. **38**(11):6010-9(2011).

83. Bezrukov, I., H. Schmidt, F. Mantlik, N. Schwenzer, C. Brendle, B. Scholkopf, and B.J. Pichler, *MR-based attenuation correction methods for improved PET quantification in lesions within bone and susceptibility artifact regions.* Journal of nuclear medicine : official publication, Society of Nuclear Medicine. **54**(10):1768-74(2013).

84. Samarin, A., C. Burger, S.D. Wollenweber, D.W. Crook, I.A. Burger, D.T. Schmid, G.K. von Schulthess, and F.P. Kuhn, *PET/MR imaging of bone lesions--implications for PET quantification from imperfect attenuation correction.* European journal of nuclear medicine and molecular imaging. **39**(7):1154-60(2012).

85. Jinsong, O., C. Se Young, Y. Petibon, A.A. Bonab, N. Alpert, and G. El Fakhri, *Bias Atlases for Segmentation-Based PET Attenuation Correction Using PET-CT and MR.* Nuclear Science, IEEE Transactions on. **60**(5):3373-3382(2013).

86. Dikaios, N., D. Izquierdo-Garcia, M.J. Graves, V. Mani, Z.A. Fayad, and T.D. Fryer, *MRI-based motion correction of thoracic PET: initial comparison of acquisition protocols and correction strategies suitable for simultaneous PET/MRI systems.* Eur. Radiol. **22**(2):439-446(2012).

87. Chun, S.Y., T.G. Reese, J.S. Ouyang, B. Guerin, C. Catana, X.P. Zhu, N.M. Alpert, and G. El Fakhri, *MRI-Based Nonrigid Motion Correction in Simultaneous PET/MRI.* J. Nucl. Med. **53**(8):1284-1291(2012).

88. Ouyang, J.S., Q.Z. Li, and G. El Fakhri, *Magnetic Resonance-Based Motion Correction for Positron Emission Tomography Imaging.* Semin. Nucl. Med. **43**(1):60-67(2013).

89. Wurslin, C., H. Schmidt, P. Martirosian, C. Brendle, A. Boss, N.F. Schwenzer, and L. Stegger, *Respiratory Motion Correction in Oncologic PET Using T1-Weighted MR Imaging on a Simultaneous Whole-Body PET/MR System.* Journal of nuclear medicine : official publication, Society of Nuclear Medicine. **54**(3):464-71(2013).

90. Petibon, Y., J. Ouyang, X. Zhu, C. Huang, T.G. Reese, S.Y. Chun, Q. Li, and G. El Fakhri, *Cardiac motion compensation and resolution modeling in simultaneous PET-MR: a cardiac lesion detection study.* Phys Med Biol. **58**(7):2085-102(2013).

91. Aiello, M., E. Salvatore, A. Cachia, S. Pappata, C. Cavaliere, A. Prinster, E. Nicolai, M. Salvatore, J.C. Baron, and M. Quarantelli, *Relationship between simultaneously acquired resting-state regional cerebral glucose metabolism and functional MRI: A PET/MR hybrid scanner study.* NeuroImage,(2015).

92. Schraml, C., M. Schmid, S. Gatidis, H. Schmidt, C. la Fougere, K. Nikolaou, and N.F. Schwenzer, *Multiparametric analysis of bone marrow in cancer patients using simultaneous PET/MR imaging: Correlation of fat fraction, diffusivity, metabolic activity, and anthropometric data.* Journal of magnetic resonance imaging : JMRI,(2015).

93. Aznar, M.C., R. Sersar, J. Saabye, C.N. Ladefoged, F.L. Andersen, J.H. Rasmussen, J. Lofgren, and T. Beyer, *Whole-body PET/MRI: the effect of bone attenuation during MR-based attenuation correction in oncology imaging.* European journal of radiology. **83**(7):1177-83(2014).

94. Andersen, F.L., C.N. Ladefoged, T. Beyer, S.H. Keller, A.E. Hansen, L. Hojgaard, A. Kjaer, I. Law, and S. Holm, *Combined PET/MR imaging in neurology: MR-based attenuation correction implies a strong spatial bias when ignoring bone.* NeuroImage. **84**:206-16(2014).

95.   Akbarzadeh, A., M.R. Ay, A. Ahmadian, N.R. Alam, and H. Zaidi, *MRI-guided attenuation correction in whole-body PET/MR: assessment of the effect of bone attenuation.* Annals of nuclear medicine. **27**(2):152-62(2013).

96.   Du, J., M. Carl, M. Bydder, A. Takahashi, C.B. Chung, and G.M. Bydder, *Qualitative and quantitative ultrashort echo time (UTE) imaging of cortical bone.* Journal of magnetic resonance (San Diego, Calif. : 1997). **207**(2):304-11(2010).

97.   Delso, G., M. Carl, F. Wiesinger, L. Sacolick, M. Porto, M. Hullner, A. Boss, and P. Veit-Haibach, *Anatomic evaluation of 3-dimensional ultrashort-echo-time bone maps for PET/MR attenuation correction.* Journal of nuclear medicine : official publication, Society of Nuclear Medicine. **55**(5):780-5(2014).

98.   Choi, H., G.J. Cheon, H.J. Kim, S.H. Choi, J.S. Lee, Y.I. Kim, K.W. Kang, J.K. Chung, E.E. Kim, and D.S. Lee, *Segmentation-based MR attenuation correction including bones also affects quantitation in brain studies: an initial result of 18F-FP-CIT PET/MR for patients with parkinsonism.* Journal of nuclear medicine : official publication, Society of Nuclear Medicine. **55**(10):1617-22(2014).

99.   Kim, J.H., J.S. Lee, I.C. Song, and D.S. Lee, *Comparison of segmentation-based attenuation correction methods for PET/MRI: evaluation of bone and liver standardized uptake value with oncologic PET/CT data.* Journal of nuclear medicine : official publication, Society of Nuclear Medicine. **53**(12):1878-82(2012).

100.   Fazzalari, N.L., I.H. Parkinson, Q.A. Fogg, and P. Sutton-Smith, *Antero-postero differences in cortical thickness and cortical porosity of T12 to L5 vertebral bodies.* Joint, bone, spine : revue du rhumatisme. **73**(3):293-7(2006).

101.   Li, Z., M.W. Kindig, D. Subit, and R.W. Kent, *Influence of mesh density, cortical thickness and material properties on human rib fracture prediction.* Medical engineering & physics. **32**(9):998-1008(2010).

102.   Bastawrous, S., P. Bhargava, F. Behnia, D.S. Djang, and D.R. Haseley, *Newer PET application with an old tracer: role of 18F-NaF skeletal PET/CT in oncologic practice.* Radiographics : a review publication of the Radiological Society of North America, Inc. **34**(5):1295-316(2014).

103.   Parsa, A., N. Ibrahim, B. Hassan, P. van der Stelt, and D. Wismeijer, *Bone quality evaluation at dental implant site using multislice CT, micro-CT, and cone beam CT.* Clinical oral implants research. **26**(1):e1-7(2015).

104.   Marshall, H.R., F.S. Prato, L. Deans, J. Theberge, R.T. Thompson, and R.Z. Stodilka, *Variable lung density consideration in attenuation correction of whole-body PET/MRI.* Journal of nuclear medicine : official publication, Society of Nuclear Medicine. **53**(6):977-84(2012).

105.   Abella, M., A.M. Alessio, D.A. Mankoff, L.R. MacDonald, J.J. Vaquero, M. Desco, and P.E. Kinahan, *Accuracy of CT-based attenuation correction in PET/CT bone imaging.* Physics in medicine and biology. **57**(9):2477-90(2012).

Vita

Hua "Asher" Ai was born in Chongqing, China (the city of hills, fogs and spicy food) on April 22nd, 1986, the third and youngest son of the family. After graduating from Chongqing Nankai Middle School in July 2004, Asher was admitted to Peking University in September 2004, where he studied Physics and received a Bachelor of Science degree in July 2008. During his undergraduate years Asher became interested in medical physics. He entered The University of Texas Health Science Center at Houston Graduate School of Biomedical Sciences to begin his doctoral study in September 2008.